



Spatial and Temporal Investigation of Localized Electric Fields in Randomly Arranged Dielectric Media.

An der Fakultät für Mathematik und Naturwissenschaften
der Carl von Ossietzky Universität Oldenburg
zur Erlangung des Grades und Titels eines
Doktors der Naturwissenschaften (Dr. rer. nat)
angenommene

Dissertation

von

Dipl.-Phys. Manfred Mascheck

**geboren am 12.06.1983
in Fritzlar**

Erstgutachter: Prof. Dr. Christoph Lienau
Universität Oldenburg

Zweitgutachter: Prof. Dr. Erich Runge
Universität Ilmenau

Tag der Disputation: 10.03.2014

Kurzfassung

Zentraler Bestandteil dieser Arbeit ist die Untersuchung der Lokalisierung von elektromagnetischen Feldern in zufällig angeordneten dielektrischen Strukturen. Der zugrunde liegende physikalische Prozess der Anderson-Lokalisierung ist die kohärente Vielfachstreuung von Wellen und deren Interferenz. Die auf diese Weise hervorgerufene Lokalisierung erfolgt auf Sub-Wellenlängen Längenskalen, im Falle von Licht im Nanometerbereich. Dabei finden die Streuprozesse auf Zeitskalen von wenigen Femtosekunden statt. Die zeitaufgelöste Untersuchung von Nanostrukturen hinsichtlich ihrer Lokalisierungseigenschaften mit ultrakurzen Laserimpulsen in Verbindung mit hochauflösender Mikroskopie stellt die eigentliche Innovation dar. Die experimentelle Verifikation erfolgt unter Verwendung eines 2-Photonen-Mikroskops in Kombination mit einem interferometrischen Autokorrelator. Zufällig angeordnete Zinkoxid-Nanonadeln stellen dabei ein ideales Material zur Untersuchung der raum-zeitlichen Lokalisierungsdynamik von Licht dar. Untersuchungen an diesen Nanostrukturen zeigen dabei stark lokalisierte Photonmoden (Hotspots) mit verlängerten Lebenszeiten im fs-Bereich. Dabei ermöglicht die Untersuchung der räumlichen Feldverteilung und deren Fluktuation die Klassifizierung der Lokalisierungsstärke. Die gemessenen Photonmoden lassen sich somit in den Bereich der starken Lokalisierung einordnen. Dabei sind die Stärke der Lokalisierung und die Lebenszeit der Photonmode miteinander korreliert. Die Stärke der Lokalisierung hängt von vielen Faktoren, wie dem Durchmesser der einzelnen Nadeln sowie deren Abstand zur nächsten Nadel, ab. Dies bezüglich konnte gezeigt werden, daß die geometrischen Eigenschaften der Nadeln und ihre räumliche Verteilung entscheidende Faktoren für die Lokalisierung sind. Des Weiteren wurden goldbeschichtete Zinkoxid-Nanonadeln mit einem Photo-Emissions-Elektronen-Mikroskops (PEEM) untersucht. Diese Methode ermöglicht die Charakterisierung der von den Nadeln emittierten Elektronen und damit die Charakterisierung der lokalen elektrischen Felder mit noch höherer räumlicher Auflösung. Die im Falle dieser Arbeit verwendeten Laser Intensitäten liegen weit unterhalb der Schwelle für einen "random laser", jedoch kann eine solche Probe von Zinkoxid Nanonadeln bei hinreichend hoher Pumpleistung auch zum lasen angeregt werden. Unter Verwendung der zeitaufgelösten 2-Photonen-Mikroskopie konnte zum ersten Mal die raum-zeitliche Dynamik der Lokalisierung von Licht experimentell verifiziert werden.

Schlagwörter: Nanostrukturen, Lokalisierung, zeitaufgelöste 2-Photonen-Mikroskopie, interferometrische Autokorrelation, PEEM, random lasing

Summary

The main research aspect of this thesis is experimental evidence for the spatial and temporal localization dynamics of light in strongly scattering, randomly arranged dielectric media. The physical concept is the Anderson localization, an interference phenomenon based on multiply scattered electromagnetic waves. The localization of light occurs on subwavelength length scales of a few hundred nanometers. For this reason the scattering events occur on timescales of a few femtoseconds. The combination of time-resolved experiments using ultrashort laser pulses and high-resolution optical microscopy to examine the localization properties of nanostructures is the key method and innovation presented in this thesis. It is based on a technique of ultra fast second harmonic microscopy and interferometric autocorrelation. Randomly distributed zinc oxide nano-needles turned out to be well suited for the investigation of the localization of light. The investigation of these nanostructures showed strongly localized photon modes (hotspots) with increased photon mode lifetimes. The fluctuations of the local electric field allow the classification of the localization strength. The localized photon modes can be classified into the regime of strong localization (Anderson localization). This shows that the localization strength and the photon mode lifetime are correlated. Many parameters influence localization, like the diameter of the needles and the distance to another adjacent needle. Therefore, the geometric shape and distribution of the needles scattering the light is crucial for the localization. Furthermore, gold coated zinc oxide nano-needles have been investigated with a higher spatial resolution by using a photo-emission electron microscope (PEEM). It allows the detection of localized electron emission generated by localized light and surface plasmon polaritons. Within this work, the used laser intensities are kept below the threshold to avoid "random lasing" from the sample. Nevertheless even random lasing can be observed by using higher intensities to pump the nano-needle array.

By using the above mentioned techniques, we were able to verify the spatial and temporal dynamics of the localization of light for the first time.

Keywords: Nanostructures, Localization, time resolved second harmonic microscopy, interferometric autocorrelation, PEEM, random lasing

Contents

Einleitung	iii
1 Introduction	1
2 Theory	5
2.1 Transport and localization of electrons	6
2.1.1 Classical transport and drift diffusion of electrons	7
2.1.2 Matter waves	8
2.1.3 The Anderson Model	11
2.1.4 Metal-insulator transition and the mobility edge	12
2.2 Transport and localization of light	13
2.2.1 Classical transport and diffusion of light	14
2.2.2 Random walk or photon diffusion	15
2.2.3 Propagation of light waves	16
2.2.4 Localization of light induced by interference	18
2.2.5 Single scaling theory	22
2.2.6 Multifractality	25
2.3 Light matter interaction	29
2.3.1 Density matrix	30
2.3.2 Optical Bloch equation	31
2.4 Interferometric Frequency Resolved AutoCorrelation and Second Harmonic microscopy	32
2.4.1 Distinguishing between coherent and incoherent emission processes	34
3 Spatiotemporal dynamics of localized photon modes in randomly arranged ZnO nano-needle arrays	37
3.1 Zinc oxide: A candidate for the localization of photon modes	38
3.1.1 Zinc oxide properties	38
3.1.2 ZnO nano-needles produced by metal-organic vapour phase epitaxy (MOVPE)	40
3.2 Spatial localization of light	42
3.2.1 Experimental set-up	42
3.2.2 Spatial localization in 100 nm thick ZnO nano-needles	45
3.2.3 Spatial localization in 30 nm thin ZnO nano-needles	48
3.2.4 FDTD calculation	56
3.2.5 Single scaling parameter	60
3.2.6 Multifractal analysis of the spatial intensity distributions	64

3.3	Temporal structure of the electric field	67
3.3.1	Experimental Set-up	67
3.3.2	Interferometric Frequency Resolved Autocorrelation	69
3.3.3	Temporal evolution of the FDTD	77
3.3.4	Spatial lifetime imaging of local photon modes	79
4	Influence of the geometric sample properties on the localization behaviour	85
4.1	Sample characterization by SEM	85
4.2	Experimental results	87
4.3	Dipole-dipole interaction model	91
4.4	FDTD calculation	98
5	Electron emission from ZnO nano-needles investigated by Photo-Emission Electron Microscopy	103
5.1	Gold-covered ZnO nano-needles	104
5.2	Experimental Set-up	105
5.3	Spatially localized electron emission	107
5.4	Single scaling parameter of the electron emission	109
5.5	Interferometric autocorrelation of the electron emission	112
6	Random Lasing in ZnO nano-structures	115
6.1	Power dependence at low fluence excitation	115
6.2	Power dependence for high fluences: Random lasing	117
7	Conclusion and Outlook	121
	Bibliography	125
	A Scattering cross section	135
	Publications and Conference contributions	141
	Curriculum vitae	143
	Danksagung	145
	Formale Erklärung	147

Einleitung

Licht einzufangen ist seit jeher ein Traum der Menschheit. Bereits im Jahre 1597 wurde in einem Kapitel des berühmten "Lalebuch", in welchem die skurrilen Geschichten der sogenannten "Schildbürger" erzählt werden, von dieser Idee berichtet. Die Geschichte erzählt vom Bau eines Hauses, in das die Schildbürger vergessen hatten, Fenster einzubauen. Um dennoch Licht ins Innere des Gebäudes zu bekommen, versuchten die Schildbürger das Licht außerhalb des Hauses in Säcken einzufangen. So ließen sie das Licht in die Säcke scheinen, schlossen diese und trugen diese ins Innere des Hauses. Beim Öffnen der Säcke stellten sie jedoch überrascht fest, dass sich darin kein Licht mehr befand. Den Schildbürgern war nicht klar, dass das Licht von den Säcken absorbiert wurde. Inwieweit diese Idee bei der richtigen Wahl der "Säcke" nicht unbedingt ein "Schildbürgerstreich" sein muss, wird in dieser Arbeit untersucht.

Die Untersuchung der Lokalisierung von elektromagnetischen Feldern oder dem Einfangen von Licht in zufällig angeordneten dielektrischen Strukturen ist zentraler Bestandteil dieser Arbeit. Dabei stellt die zeitaufgelöste Untersuchung von Nanostrukturen hinsichtlich ihrer Lokalisierungseigenschaften mit ultrakurzen Laserimpulsen in Verbindung mit hochaufgelöster Mikroskopie die eigentliche Innovation dar.

Das Konzept zur Lokalisierung beruht auf der Vorhersage P. W. Andersons im Jahre 1958 [1]. Er beschreibt in dieser Arbeit das Ausbleiben von Elektronen-Diffusion, dem unkontrollierten Ausbreiten von Elektronen, bei hinreichender Unordnung im Festkörper. Das von Anderson aufgestellte Konzept über die Lokalisierung von Elektronen wurde innerhalb der letzten 55 Jahre auf eine Vielzahl von modifizierten Theorien und Experimenten angewandt. Diese reichen von klassischer Diffusions- und Transporttheorie bis hin zur Vielfachstreuung von Wellen in ungeordneten Systemen und den daraus resultierenden Interferenzphänomenen [2]. Das Phänomen der starken Lokalisierung, auch als Anderson-Lokalisierung bezeichnet, wurde nach ihm benannt.

Der zugrundeliegende physikalische Prozess der Anderson-Lokalisierung ist die kohärente Vielfachstreuung von Wellen in zufällig angeordneten Medien. Dies führt durch konstruktive Interferenz der an verschiedenen Stellen innerhalb des Mediums gestreuten elektrischen Felder zur Lokalisierung an zufälligen Positionen. Dies konnte für Elektronenwellen in stark ungeordneten Festkörpern, wie z.B. in Quanten Drähten (quantum wires) gezeigt werden [3]. Die räumliche Dimension des untersuchten Systems beeinflusst dabei jedoch stark die Lokalisierung. Die angesprochenen quasi eindimensionalen "quantum wires" zeigen sogar Lokalisierung für Elektronen mit kinetischen Energien weit oberhalb der Potentialfluktuationen [4]. An jeder der Potentialfluktuationen existiert

eine endliche Wahrscheinlichkeit, dass die Welle gestreut wird. Dies führt zu einer Reduzierung der Transmissionswahrscheinlichkeit.

Die experimentelle Bestätigung von Lokalisierung ist aufwendig und nicht immer eindeutig. Transmissionsexperimente beispielsweise weisen die Problematik auf, dass sowohl Absorption als auch Lokalisierung zu einem exponentiellen Abfall der Amplitude des transmittierten Lichtes führen. Die Stärke des Abfalls skaliert mit der Probendicke und wird durch das Gesetz von Beer-Lambert beschrieben [5, 6]. Diesbezüglich ist der exponentielle Abfall keine Signatur, die zweifelsfrei der Lokalisierung zugeschrieben werden kann [2].

Die Lokalisierung in zwei- oder sogar dreidimensionalen Systemen ist aufwendig zu berechnen, da alle möglichen Streupfade zur Lokalisierung beitragen. Ein Ansatz, die Lokalisierungsstärke auch in komplexen mehrdimensionalen Systemen zu quantifizieren, wurde von Ioffe und Regel formuliert (Ioffe-Regel Kriterium) [7]. Es vereinfacht die komplexe Physik der Anderson-Lokalisierung durch das Produkt aus Wellenvektor und der mittleren freien Weglänge.

Viel allgemeiner können die hier behandelten Lokalisierungsphänomene als ein generelles Wellen-Phänomen betrachtet werden, das nicht nur für Elektronen zu beobachten ist. Der Transfer von Lokalisierung in elektronischen Systemen hin zu elektromagnetischen Wellen, wie z.B. für Licht, ist bereits hinreichend in der Literatur diskutiert [8, 9]. Lokalisierung tritt bei nahezu allen Wellen auf. Experimentelle Nachweise existieren für die Lokalisierung von Ultra-Schall [10], Oberflächen Plasmonen Polaritonen in metallischen Filmen [11] oder von Licht in zufällig angeordneten dielektrischen Materialien [12, 13]. Dabei kann es durch Lokalisation und geschlossene Trajektorien von vielfach gestreutem Licht sogar zu "Random Lasing" kommen [14].

Jedoch speziell im Falle der Lokalisierung von Licht, welche räumlich auf Sub-Wellenlängen Längenskalen von wenigen hundert Nanometer auftritt, ist die direkte mikroskopische und spektroskopische Untersuchung überaus anspruchsvoll [15]. Die Untersuchung der zeitlichen Struktur ist nochmals anspruchsvoller, da die Streuprozesse auf Zeitskalen von wenigen Femtosekunden stattfinden. Erst durch die Entwicklung ultrakurzer Laserimpulse, wie z.B. des Ti:Saphir Laser-Oszillators im Jahre 1986 [16], wurde die Möglichkeit geschaffen, die zeitliche Struktur von lokalisiertem Licht experimentell zu verifizieren.

Die hohen experimentellen Anforderungen an Lichtlokalisierung in Raum und Zeit führen vielfach zur Untersuchung indirekter Signaturen der Lokalisierung, wie z.B. der kohärenten Rückstreuung [5]. Diese ist ein Interferenz-Phänomen, das auf der konstruktiven Interferenz von vielfach gestreuten Wellen in einem elastisch streuenden Medium herrührt. Dabei interferieren Wellen einer zufälligen Streutrajektorie mit jeweils der Welle, die in entgegengesetzter Richtung ("time reversal") entlang derselben Trajektorie propagiert. Aufgrund der identischen Trajektorienlänge haben beide Wellen dieselbe Phase und interferieren konstruktiv. Entsprechend wird die kohärente Rückstreuung als eine Signatur für Lokalisierung betrachtet [5, 18, 19].

Bei Streuprozessen an Objekten, die kleiner als die Wellenlänge des einfallenden elektrischen Feldes sind, tritt vielfache Rayleigh-Streuung auf. Dabei werden die kohärenten Eigenschaften des elektrischen Feldes erhalten.

Für die starke Lokalisierung (Anderson-Lokalisierung) existieren Vorhersagen über starke Schwankungen der lokalen elektrischen Feldstärke, sowie Änderungen bezüglich der zeitlichen Struktur [2]. Die Interferenz führt zu starken,

räumlich eng begrenzten elektromagnetischen Feldern, die als "hotspots" bezeichnet werden. Diese "hotspots" wurden bereits ausführlich für Licht in photonischen Kristallfasern [20, 21, 22] und in metallischen Nanostrukturen [11, 23, 24, 25] untersucht. Zusätzlich führt die kohärente Vielfachstreuung zu einer Modifikation der zeitlichen Struktur des lokalisierten elektrischen Feldes im "hotspot", was jedoch nur theoretisch für Oberflächen-Plasmonen-Polaritonen in ungeordneten Metall-Nanopartikeln berechnet wurde [2, 27]. Somit besitzen Lokalisierungsphänomene aufgrund von Vielfachstreuung zwei charakteristische Eigenschaften: Zum einen räumlich eng begrenzte, starke Feldfluktuationen und zum anderen verlängerte, lokale Lebenszeiten der Felder.

Es gibt vielfache Anwendungen von lokalisiertem Licht. Neben dem "Random Lasing" in Zinkoxid-Nanopartikeln [14, 26, 28] und der verstärkten Oberflächen-Raman-Streuung, die sogar Spektroskopie an einem einzelnen Molekül erlaubt [29, 30], liegt eine weitere Anwendungsmöglichkeit in der Verstärkung der Konversionseffizienz in der Photovoltaik [31, 32].

Der Hauptaugenmerk dieser Arbeit liegt auf der experimentellen Untersuchung der raum-zeitlichen Dynamik von Licht-Lokalisierungseffekten in stark streuenden dielektrischen Medien. Die Untersuchung der räumlichen Feldverteilung und deren Fluktuation erlaubt die Klassifizierung der Lokalisierungsstärke. In Verbindung mit zeitaufgelösten Messungen kann die Lokalisierung aufgrund von Vielfachstreuung verifiziert werden. Die dafür notwendigen theoretischen Konzepte der Lokalisierung und der Quantifizierung der Lokalisierungsstärke werden eingeführt (chapter 2). Zufällig angeordnete Zinkoxid-Nanonadeln stellen dabei ein ideales Material zur Untersuchung der raum-zeitlichen Lokalisierungsdynamik von Licht dar.

Die Untersuchung erfolgt unter Verwendung eines 2-Photonen-Mikroskops in Kombination mit einem interferometrischen Autokorrelator (chapter 3). Dieser Aufbau erlaubt es auch unterschiedliche Probengeometrien der Zinkoxid-Nanonadeln bezüglich ihrer Lokalisierungseigenschaften zu untersuchen (chapter 4). Unter Verwendung eines Photo-Emissions-Elektronen-Mikroskops (PEEM) und der Untersuchung von lokalisierter Elektronenemission auf goldbeschichteten Zinkoxid-Nanonadeln, lässt sich die Lokalisierung elektrischer Felder mit noch höherer räumlicher Auflösung untersuchen (chapter 5). Abschließend werden auch die Eigenschaften eines "random lasers" untersucht (chapter 6).

Chapter 1

Introduction

For centuries people have been dreaming about trapping light, as already written down in the famous "Lalebuch" from 1597 which is better known as the "Schildbürger" and their foolish acts. One of the most famous stories deals with the town hall in which they forgot to implement windows. Due to that, it was dark inside. The Schildbürger thought about how to solve the problem and tried to catch light in bags and take them into the house. They wondered why it still remained dark after opening the bags. They did not realize that the light was simply absorbed.

Within this thesis, the localization or the trapping of electromagnetic fields in randomly arranged dielectric media will be investigated by a combination of time-resolved experiments using ultrashort laser pulses and high-resolution optical microscopy.

The concept of wave localization is based on a prediction by P.W. Anderson in 1958 [1] concerning the absence of electron diffusion and the resulting localization of electrons in solid state materials with a sufficient degree of disorder. Anderson's idea has been expanded and modified during the last 50 years to a variety of theories and experiments from classical diffusion and transport theory to multiple scattering wave interference phenomena [2]. Strong localization in disordered systems, also called Anderson localization, was named after him.

Coherent multiple wave scattering within random media is the underlying physical principle of localization, as demonstrated for electron waves in disordered solid media, for example in quantum wires [3]. The localization in general strongly depends on the dimension of the investigated system. It was shown that even electrons with kinetic energies that exceed the average height of the potential fluctuations localize in one-dimensional systems [4]. At each potential fluctuation, there is a finite probability of being scattered. This results in a decrease of the total transmission probability. A general problem of transmission experiments is that both, absorption as well as localization phenomena, lead to an exponential decrease of the transmitted intensity. This behaviour is related to the sample thickness as described by Beer-Lambert's law [5, 6]. Therefore the exponential decrease is not a signature unambiguously related to localization within a sample [2].

Localization in 2- or even 3-dimensions is difficult to simulate numerically, since all possible scattering paths can contribute to localization forming a locally con-

finer material excitation. An attempt to classify different regimes of localization is based on the Ioffe and Regel criterion [7]. It simplifies the complex physics of the Anderson localization to the product of the mean free path length and the wave vector.

However, localization phenomena are not restricted to electrons. They are a general wave phenomenon. The transfer from localization in electronic systems to electromagnetic waves, i.e. light, has been discussed in literature [8, 9]. Localization occurs for nearly all kinds of waves as recently demonstrated for ultrasonic experiments [10], surface plasmon polaritons at metallic films [11] or light in random dielectric media [12, 13], where closed loops of multiply scattered light can lead to random lasing [14].

But especially for light, a direct microscopic and spectroscopic investigation of the localization remains challenging to observe [15] since it involves wave localization on the sub-wavelength length scales in the order of a few hundred nanometers. The temporal investigation of the localization of light is even more challenging since the corresponding dynamical scattering processes occur on timescales of a few femtoseconds. Therefore, the invention of ultrashort laser pulses, as generated by Ti:Sapphire laser oscillators in 1986 [16], opened the possibility to investigate the temporal dynamics of localized states.

Due to the high experimental requirements for measuring localization of light in space and time, a lot of experiments were performed investigating indirect signatures of localization. One example is the coherent backscattering effect [5]. Coherent backscattering is an interference phenomenon resulting from the constructive interference of a multiply scattered wave subjected to a random walk in an elastically scattering medium and the wave propagating along the same trajectory in the opposite direction (time-reversed). Due to the same path length, the phase is the same and they interfere constructively. Therefore enhanced coherent backscattering is an indicator for localization [5, 18, 19].

In the regime of multiple Rayleigh scattering, strong fluctuations of the local field intensity distribution, as well as changes in the temporal response, are predicted due to interference and the formation of enhanced, spatially highly confined electromagnetic fields, so-called "hotspots" [2]. These hotspots have been studied for light in detail for photonic crystal waveguides [20, 21, 22] and for metallic nanostructures [11, 23, 24, 25]. In addition, multiple scattering leads to a distinct modification of the temporal structure of the electromagnetic fields within the localized spots as calculated for surface plasmon polaritons in disordered arrays of metal nanoparticles [2, 27]. Therefore, localization due to multiple coherent scattering has two hallmarks: enhanced spatial electromagnetic field fluctuations and enhanced local lifetimes.

Applications for the localized photon modes in strongly scattering media are random lasing in semiconductor powders [14, 26, 28] or surface enhanced Raman-scattering single molecule spectroscopy [29, 30]. Furthermore, localized or trapped light inside of structured photovoltaic devices enhance the conversion efficiency [31, 32].

The main research aspect within this thesis is the experimental evidence of the space and temporal localization dynamics of light in strongly scattering random dielectric media, i.e. ZnO nano-needles with diameters in the range of

30 to 200 *nm*. It is based on a new technique of ultra fast second harmonic microscopy in combination with interferometric autocorrelation. The investigation of the spatial confinement field fluctuations allows to determine the localization strength. In combination with time-resolved measurements the localization based on multiple scattering is investigated. Therefore, the basic theoretical concepts of localization and the classification of the localization strength are introduced (chapter 2). The spatial and temporal localization properties of photon modes are measured and classified (chapter 3). This set-up allows to investigate the localization behaviour of different geometric sample properties of the ZnO nano-needles (chapter 4). In addition, the localization is investigated with a higher spatial resolution by using a photo-emission electron microscope (chapter 5) detecting localized electrons emitted by localized light and surface plasmon polaritons from gold covered nano-needles. Furthermore, the random lasing behaviour of the bare ZnO nano-needles (chapter 6) is investigated.

Chapter 2

Theory

The main part of this thesis deals with the spatial and temporal localization of light waves. Therefore, the basic theoretical concepts of the localization are described in this chapter.

Historically, localization was not described for light waves at first. It was described by P.W. Anderson in 1958 according to the absence of electron diffusion at a certain amount of disorder. Later on, the localization theory was expanded to a more general class of wave localization phenomena. Here I follow this historical approach and first present a brief theoretical description of the transport and localization properties of electrons in the solid state media (section 2.1). In section 2.2 these concepts are transferred to the localization of light waves.

The propagation of electrons or matter waves is described by the Schrödinger equation (section 2.1.2), whereas the propagation of light is described by the wave equation (Helmholtz equation) derived from Maxwell's equation (section 2.2.4). Although conceptual differences in the theoretical description for the propagation of light and material waves exist, both can be described by plane waves interacting with a constant refractive index, i.e. a constant potential energy.

In order to understand the experimental results of localized photon modes, one must consider multiple scattering events. Strong localization or Anderson localization of light is based on the interference of coherent, elastically scattered light within strongly scattering media. In section 2.2.4 an indirect signature of localization, coherent backscattering, which is based on the constructive interference of time-reversed scattering paths, is described. In section 2.2.5 and 2.2.6 two ways of classifying the localization strength are introduced. The spatial intensity distribution can be divided into localized and delocalized regimes using the single parameter scaling theory (2.2.5) or the multifractal analysis (2.2.6). In section 2.3, the approach to describe the light-matter interaction is explained. It is described theoretically based on optical Bloch equations which allow the deduction of the temporal aspects of localized photon modes. To classify localization based on the constructive interference of multiply scattered waves, a distinction between coherent and incoherent photon modes is important. Therefore, section 2.4 introduces the interferometric frequency-resolved autocorrelation technique which is the essential tool when focusing on coherent light.

2.1 Transport and localization of electrons

The pioneering work of Anderson has spawned a rich variety of theories and experiments. At first only noticed by few of his colleagues, it took many years till Andersons publication was noticed more and more. Currently Anderson localization is a field of research with high priority [33].

In this context, a few other important publications will be mentioned. In 1994, Belitz and Kirkpatrick [3] reviewed a quantum phase Anderson transition and developed a general scaling theory of a metal-insulator and related transitions to compare them with the experimental results. This transition depends on the disorder and was demonstrated for electron waves in solid media. The metalinsulator transition, the general class of the quantum phase transition, is characterized by its threshold value. Above this threshold value, the solid acts as a metal whereas below the threshold it behaves like an insulator.

Theoretical simulations with a one-dimensional tight-binding model using long range correlations in disordered solids were performed in 2002 by Carpena et al [34] to investigate the effect on the physical properties of the electron wave function.

In 2008 Billy et al [35] reported the observation of the exponential localization of a BoseEinstein condensate released into a one-dimensional waveguide in the presence of a controlled degree of disorder generated by laser speckles. The direct imaging of the atomic density as function of the time allows to determine the disorder, which leads to a localized wave function. Therefore, the localization length within the system was determined as a function of the disorder. Enhanced disorder results in stronger localization and a decreased localization length. A small degree of disorder results in extended states which result in a Gaussian distribution of the local density of states (LDOS).

Richardella et al published an important article in 2010 [36]. They used energy resolved scanning tunneling microscopy to map electronic states in $Ga_{1-x}Mn_xAs$ relative to the Fermi energy. For a degree of disorder close to the metal-insulator phase transition, they observed strong spatial variations in the local value of the tunneling conductance, which is associated with the local density of states (LDOS). The spatial fluctuations of the LDOS are used to characterize the localization behaviour. Within the valence band, the probability distribution of the normalized LDOS has a Gaussian shape, whereas for energies close to the Fermi energy and disorders close to the metal-insulator transition, the probability distribution changes towards a log-normal distribution.

Furthermore, the localization of excitons in semiconductors was investigated. Hess et al. [37] investigated the spectral distribution of the fluorescence from GaAs/AlGaAs quantum wells by low-temperature near-field scanning optical microscopy. They found that distinct emission lines together with magnetic field and temperature measurements establish laterally localized excitons at interface fluctuations.

Later, Intonit et al. [38] used a similar technique to investigate single quantum wells. They observed spatially resolved photoluminescence spectra with sharp emission lines from localized excitonic states. The propagation of an exciton within a quantum theory in a 2-dimensional spatially disordered potential results in characteristic quantum mechanical energy level repulsion related to spatial and energetic correlations of excitons in disordered quantum systems.

In order to put these shortly mentioned results into perspective, a brief introduction to the transport and localization behaviour of electrons is given in this section. Later, this will be generalized for different kinds of waves, especially light waves.

2.1.1 Classical transport and drift diffusion of electrons

Electrons can either propagate diffusively or ballistically in the solid state media. Diffusive transport is a stochastic propagation process of the electrons which depends on the scattering properties of the medium. The propagation depends on aspects such as temperature, density of crystal defects, phonons, etc. All these aspects are described by the mean free path length l which is the distance between two scattering events. It can be used to classify the transport through a sample of the thickness d to be either in the diffusive or ballistic regime. The ballistic and diffusive drift propagation are schematically illustrated in figure 2.1. For diffusive transport, the mean free path length follows $l < d$. In the case

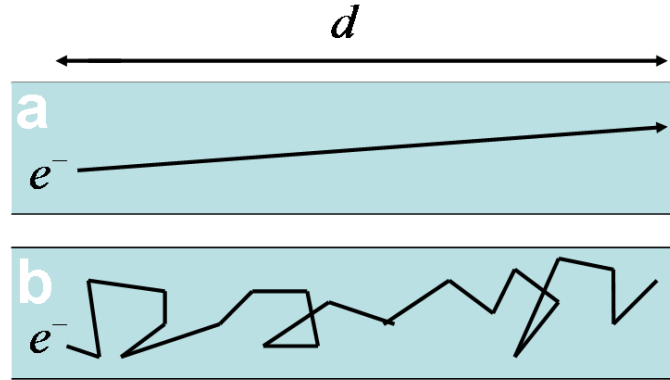


Figure 2.1: Schematic illustration of the transport of electrons through a solid state of the length d . The free mean path length l allows to distinguish **a** the ballistic propagation with $l > d$ and **b** the diffusive drift propagation with $l < d$.

of ballistic transport, the mean free path length is sufficiently large ($l > d$) for the electrons to propagate undisturbed.

Drude developed a model in order to describe the diffusive transport of electrons in solids. In general, however, the wave properties of electrons can not be ignored. In the case of diffusive propagation, multiple scattering leads to constructive and destructive interference of the different scattered waves. This results in averaging and allows to describe the propagation of an electron as a particle in a semi classical picture of motion. The Drude model qualitatively accounts for the drift diffusion of electrons through solids in an external electric field \vec{E} . Between the scattering events, the electrons move undisturbed on a straight line as described by the free-electron approximation. The electrons are scattered at the ions, defect states, phonons etc., while propagating through the solid, which strongly influences the mean free path length l . The free path length corresponds to a mean free propagation or collision time τ . The velocity of the electron directly after the collision is described by \vec{v}_0 . Due to the

acceleration of the external electric field, this yields to

$$m_e \left(\frac{d\vec{v}_0}{dt} + \frac{\vec{v}_d}{\tau} \right) = -e\vec{E} \quad (2.1)$$

by using the electron mass m_e and the elementary charge e . The scattering of an electron is uncontrolled which results in scattering trajectories in any direction. Therefore, the average speed of the electron is $\vec{v}_0 = 0$. This leads to

$$\vec{v}_d = \frac{-e\vec{E}}{m_e} \cdot \tau = \frac{-e\vec{E}}{m_e} \cdot \frac{l}{v_F} \quad (2.2)$$

connecting the drift velocity \vec{v}_d and the mean free path length l to the Fermi velocity $v_F = \sqrt{2E_F/m_e}$. The current density \vec{j} and the conductivity σ are then described by:

$$\vec{j} = -en\vec{v}_d = \frac{e^2 n \vec{E}}{m_e} \cdot \frac{l}{v_F} \quad \sigma = \frac{\vec{j}}{\vec{E}} = \frac{e^2 n}{m_e} \cdot \frac{l}{v_F} \quad (2.3)$$

with $n = \frac{N_A \cdot \rho}{M}$, the electron density calculated from the bulk density ρ , the atomic mass M and the Avogadro constant N_A . Equation 2.3 corresponds to Ohms law. For the case of a typical metal like copper, with a Fermi energy of approximately $7 eV$, the mean free path length¹ of the electrons is

$$l_{Cu} = \frac{\sigma m_e v_F}{ne^2} \approx 40 \text{ nm} \quad . \quad (2.4)$$

By using equation 2.2, the mean free path length can be expressed in the mean free propagation time

$$\tau_{Cu} = \frac{l_{Cu}}{v_F} \approx 25 \text{ fs} \quad (2.5)$$

for an electron in copper. The short time between two collisions makes it rather difficult to observe ballistically propagating electrons. The diffusive propagation of electrons in metals is the general transport condition. Ballistic transport of an electron, as illustrated in figure 2.1a is therefore limited to $t < \tau$. However, this can be achieved at low temperatures increasing the mean free path length l or in nanostructures with $l > \Lambda$ with Λ the size of the nanostructures [39].

2.1.2 Matter waves

More generally, electric motion in solids must be described in terms of the dynamics of electron wave packets. The propagation of a matter wave however can be described by the time-dependent Schrödinger equation and is characterized by its wave function $\Psi(x, t)$ [53]. The 1-dimensional Schrödinger equation

$$\left[\frac{-\hbar^2}{2m^*} \Delta + V(x) \right] \Psi(x, t) = i\hbar \frac{\partial}{\partial t} \Psi(x, t) \quad (2.6)$$

describes the temporal evolution of the wave function $\Psi(x, t)$ with an effective mass m^* , potential $V(x)$ and energy E . The solution of the Schrödinger equation depends on the potential energy distribution $V(x)$.

¹The conductivity at room temperature is $\sigma = 5.9 \cdot 10^7 \frac{1}{\Omega m}$, $v_F = 1.6 \cdot 10^6 \frac{m}{s}$ and $n_e = 8.5 \cdot 10^{28} \frac{1}{m^3}$.

i First, a constant potential which does not depend on the spatial position is considered. The solution of the Schrödinger equation results for $V(x) = const$ in plane waves

$$\Psi(x, t) = A_0 e^{i(kx - Et)} . \quad (2.7)$$

The dispersion relation is then described as:

$$\omega = \hbar k^2 / 2m^* . \quad (2.8)$$

The wave function $\Psi(x, t)$ contains all the information and allows for a complete characterization of the system.

ii In a second case, a non-constant, spatial varying potential is assumed. In order to do this, the dispersion relation and the wave function are modified. For the case of a perfect periodic potential $V(x)$ the solution of the Schrödinger equation results in Bloch waves which are extended across the solid [51]. In order to describe the propagation of an electron, the wave function should be represented by a coherent superposition of Bloch waves forming a wave packet. At some positions in space, the constructive interference results in regions with a high probability of finding the electron, whereas averaging over constructive and destructive interference of different waves at other positions results in a small probability [53].

On time scales $t < \tau$, the scattering of wave packets can be neglected. On these short femtosecond time scales, they propagate undisturbed and have a well defined phase relation, i.e dephasing and the loss of coherence can be neglected.

At later times $t > \tau$, scattering occurs, which can destroy the phase coherence depending on the type of scattering. The coherence is destroyed, due to inelastic scattering at phonons. However, the coherence is conserved for elastically scattered waves at stationary, yet spatially varying potential fluctuations.

The spatial extent of the electron wave function, which corresponds to the probability of finding the electron wave packet as a function of the position, strongly depends on the spatial potential fluctuations $V(x)$. By assuming elastic scattering of the wave packet at $V(x)$, the spatial extent of the wave packet depends on the potential strength and the correlation length L_c .

For plane waves in a constant potential, the wave packet propagates undisturbed over the complete system and the electron wave function is extended.

Where increasing potential fluctuations $V(x)$ are still smaller than the kinetic energy of the electrons, the solution of the wave equation does not result in plane waves and the electron wave function is not extended across the solid anymore. However, the wave function is still spread over a large area as illustrated in figure 2.2. For kinetic energies of the electrons smaller than the embedding potential energy fluctuations, the amplitude of the wave function decreases exponentially in space as illustrated by the dashed lines in figure 2.2c.

The signature of localization is a decrease in the amplitude of the wave function Ψ at a certain length scale which is called the localization length ξ . In the case of strong localization (Anderson localization) it behaves like

$$|\Psi(x)| \propto \exp\left(-\frac{|x - x_0|}{\xi}\right) \quad (2.9)$$

as function of the position x with x_0 being the position of the localized wave function. The direct measurement of the wave function is challenging. There-

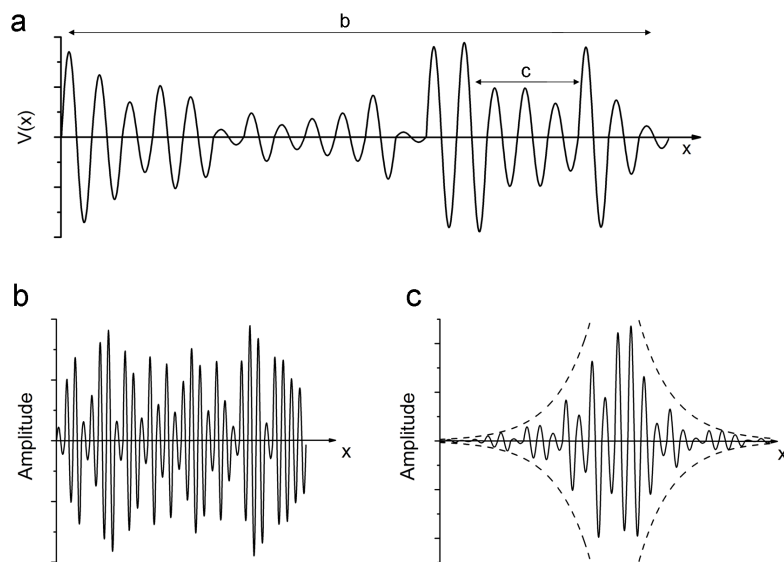


Figure 2.2: **a** Schematic illustration of spatial random potential fluctuations. Electrons with energies far above the potential fluctuations act on these spatial scales as extended wave functions **b** whereas electrons with lower kinetic energy localize as illustrated in **c**.

fore, a lot of indirect measurements are performed. However, indirect measurements like transmission experiments with an exponential decrease of the amplitude of the wave function are not a signature unambiguously related to localization. Absorption processes also show an exponential decrease of the amplitude of the wave function depending on the sample thickness as described by Beer-Lambert's law [6]. Therefore it remains challenging to assign the decrease in the transmission unambiguously to localization [2].

The analysis of the coherence properties allows to distinguish absorption and localization. While the coherence is destroyed by absorption, localization based on elastic scattering conserves the coherence properties. This will not be explained in further detail in this section. However, the concepts to distinguish between coherent and incoherent processes are explained in more detail for light in section 2.4.1.

Due to the exponential drop of the intensity, localized states should be insensitive to changes of the total sample size as long as the sample size is larger than the localization length ξ . In contrast, extended Eigenfunctions should be sensitive to the sample size, especially to changes in the boundary conditions.

2.1.3 The Anderson Model

The theoretical model introduced by P.W. Anderson is known as the "nearest neighbour tight binding model" [1]. The model is based on solving the Schrödinger equation on a periodic lattice of i atoms. Electrons propagate by hopping from one lattice position to the other. The periodic atomic arrangement results in discrete energy values that enable the hopping. The hopping is described by the matrix element $t_{i,j}$ and the operators a_i^\dagger for creating and a_j for annihilating an electron on the lattice position i, j , respectively [40]. This results in an expression of

$$T = \sum_{i,j} t_{i,j} a_i^\dagger a_j \quad (2.10)$$

for the kinetic energy, neglecting spin interaction [40]. Disorder is introduced by the potential energy

$$V = \sum_i V_i a_i^\dagger a_i \quad (2.11)$$

in terms of a randomly varying amplitude V_i at each lattice position. The Hamiltonian of the system is therefore described by:

$$H = T + V = \sum_{i,j} t_{i,j} a_i^\dagger a_j + \sum_i V_i a_i^\dagger a_i . \quad (2.12)$$

Electrons with kinetic energy ε localize if the disorder of the system, respectively the spread of the amplitude of the potential energies V_i , is sufficiently large compared to ε . While the electron wave function is extended for a periodically arranged lattice of equal atomic potentials, the Eigenstates of the wave function localize at a sufficient amount of disorder [41].

The classical diffusion and transport theory is based on many scattering events but does not consider phase information from previous scattering events. However, the Anderson localization is based on the coherence of elastic multiply scattered matter waves. Neglecting previous scattering events and their phases is simply not correct when describing the Anderson localization.

2.1.4 Metal-insulator transition and the mobility edge

Various processes, like electron-electron interaction, temperature or disorder can convert a solid state from metallic to insulating behaviour [47, 48, 49]. However, this also occurs in bare media with sufficiently strong Coulomb interaction between electrons and nucleus, leading to an overlap of energy levels known as the Mott Hubbard insulator transition [17]. In the following, only the metal-insulator transition (MIT) induced by disorder is considered [1, 50] and strong Coulomb interaction is neglected.

The induced disorder can be modeled by the use of the Kronig-Penney model. Within this model, the lattice of a solid state is described by a square potential well as shown in figure 2.3. Solving the Schrödinger equation for such a system

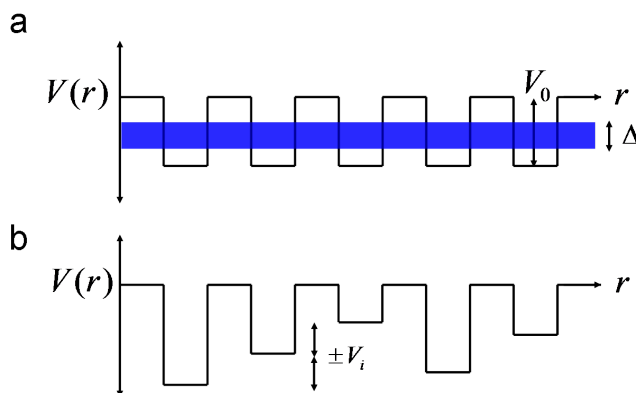


Figure 2.3: **a** Steady potential wells with extended states described by Bloch waves with an energetic bandwidth Δ . **b** The depth of the wells varies by $\pm V_0/2$.

of periodically arranged potential wells results in the known Bloch waves and energy bands extended over the whole system with a corresponding energetic bandwidth Δ [51]. Disorder is induced by using fluctuations in the potential energy which is chosen to be $\pm V_i$ as illustrated in figure 2.3b. The disorder of the system is characterized by $\delta = V_i/\Delta$ using the undisturbed energetic bandwidth Δ . The statistic fluctuations of the potential energy wells result in an increasing energetic bandwidth [41, 42]. As shown by Mott, implementing a minimum of disorder immediately leads to localized states at the energetic edges of the band [17] as illustrated in figure 2.4. The energy that separates extended and localized states, is called the mobility edge. When further increasing disorder, the mobility edge shifts towards the center of the energy band and more states become localized. At a sufficient disorder δ_c all states become localized. This disorder is also called the critical disorder strength. Therefore, the increase of disorder changes the conductivity from metallic behaviour into an insulator. As in every solid, the position of the Fermi energy allows to classify the system into metallic or insulating behaviour. Therefore, a metal can become an insulator if the mobility edge at a sufficient amount of disorder reaches the Fermi energy. This is called Anderson metal-insulator transition and stands in contrast to the Mott metal-insulator transition, which is due to Coulomb interaction and exhibits a gap in the energy spectrum (band structure).

A simplification of the complex physics of the Anderson localization is based on

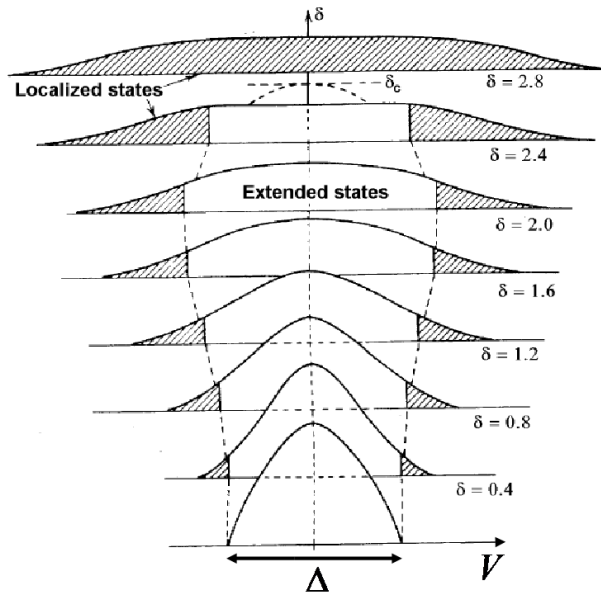


Figure 2.4: Schematic illustration of the metal-insulator transition. An increase of the disorder δ leads to a shift of the mobility edge towards the centre of the energetic band and more states are localized. The mobility edge separates localized and delocalized states. At the critical disorder δ_c all states are localized.[50, 42]

the Ioffe-Regel criterion.

The Ioffe Regel criterion connects the complex physics behind the Anderson localization to the mean free path length [7]. If the product of the free mean path-length l and the wave vector k is equal or less than 1, the system is considered to be in the localized regime. For the case that the product is bigger than 1, the system is delocalized. The transition from metallic to insulator behaviour, i.e. delocalized to localized states, takes place, if

$$k \cdot l \approx 1 \quad . \quad (2.13)$$

2.2 Transport and localization of light

In 1984, S. John realized that the Anderson localization goes far beyond the localization of electrons. It is a general wave phenomenon in systems with disorder and the theoretical description can easily be transferred to electromagnetic waves, which has been discussed in the literature [8, 9].

In contrast to the propagation of electrons, which are influenced by incoherent scattering at thermally excited phonons and the strong electron-electron interaction, the propagation of light is not as strongly influenced. Light consists of photons, uncharged bosons. Therefore, they are undisturbed by Coulomb interaction with each other. The undisturbed propagation of light makes it quite interesting to investigate localization phenomena for light.

Due to these circumstances, the experiments presented in this thesis are performed with light. The theoretical treatment of the transport and localization theory for light are explained in the following section.

2.2.1 Classical transport and diffusion of light

The propagation of light is very similar to the propagation of electrons concerning their behaviour. However, in general, the propagation of light in a transparent medium is a ballistical process. As already introduced for electrons, the mean free path length l allows to distinguish between ballistic propagation and diffusion. The mean free path length of light in air is in the range of meters and decreases to several μm for the case of $BaSO_4$ -powder [56], which is an ingredient in white paint. Schematically, the propagating behaviour is illustrated for light and a fixed propagation direction in figure 2.5. However, the localization

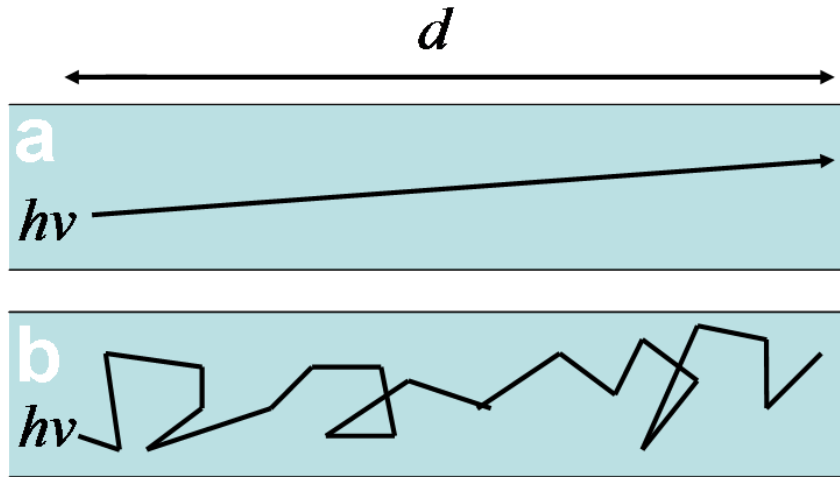


Figure 2.5: Schematic illustration of ballistic propagation **a** and diffusive propagation **b** of light in a certain direction through a medium.

of light requires sufficiently strong scattering which results in a short mean free path length. One way to describe this kind of propagation is based on the diffusion equation, which is based on the continuity equation and Fick's law. It is described without external sources by

$$-D \frac{\partial^2 \Psi}{\partial t^2} + \frac{1}{L_D^2} \Psi = 0 \quad (2.14)$$

with the diffusion length $L_D = \sqrt{D/S_a}$, the absorption cross section S_a and the diffusion coefficient D [41]. The diffusion coefficient is a measure of the mobility of the photons. The probability of finding a photon after time steps t_i is illustrated in figure 2.6. The photon can diffuse in a 1-dimensional system in the positive or negative direction which results in a spread of the probability distribution. Within this transport theory all the characteristics of a wave, like the coherence, are neglected. The photon behaves like a classical particle within this description.

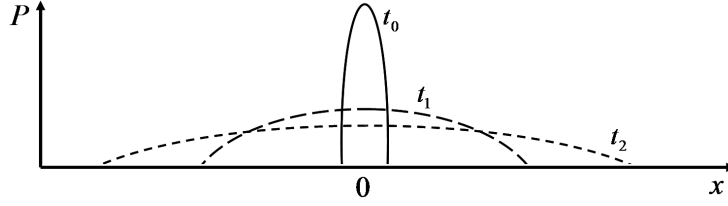


Figure 2.6: Probability of finding a photon in a 1-dimensional system at time steps t_i . The photon starts to diffuse in any direction.

2.2.2 Random walk or photon diffusion

Another way to describe the propagation of strongly scattered photons is based on the random walk model, dividing the propagation into individual ballistic propagation steps. The random walk model, first discussed by Richard Feynman [46], calculates the probability of finding a photon at a certain position in time and space. The initial starting position of the photon is assumed to be $x_0 = 0$. In one dimension, it can propagate in the positive x_p or negative direction x_n . Within a time step dt the photon travels the fixed distance s and the displacement is given after i time steps by $x(t_i) = x(t_{i-1}) \pm s$.

The total mean displacement of a photon is $\lim_{t \rightarrow \infty} \langle x(t) \rangle = 0$ because the probability that the photon will travel in the positive or negative direction is the same.

The spread of the random walk is related to the propagation length of a photon. This is given by the mean squared displacement:

$$\langle x_j(t_i)^2 \rangle = \frac{1}{N} \sum_{j=1}^N x_j^2(t_i) = \frac{1}{N} \sum_{j=1}^N (x_j(t_{i-1})^2 \pm 2x_j(t_{i-1})s + s^2) \quad (2.15)$$

with N being the total number of photons. Since the probability of the photon propagating in the positive or negative direction is equal, the term $\langle 2x_j(t_{i-1})s \rangle = 0$ in equation 2.15 vanishes [57].

Assuming that the photon starts to propagate at $x_0 = 0$ the mean squared displacement changes at each time step by the value of s^2 and equation 2.15 can be written as:

$$\langle x(t_i)^2 \rangle = i \cdot s^2 \quad (2.16)$$

The distance of the photon after i propagation steps to the origin is described by $x = (x_n - x_p) \cdot s = m \cdot s$. The mean squared distance is given by $\langle m^2 \rangle = i$ with $m = \frac{x}{s}$ and $i = \frac{t}{dt}$. this leads to

$$\langle m^2 \rangle = \frac{\langle x(t_i)^2 \rangle}{s^2} \quad (2.17)$$

By using these relations, the mean square displacement

$$\langle x(t_i)^2 \rangle = s^2 \cdot \langle m^2 \rangle = s^2 \cdot i = s^2 \frac{t}{dt} = \frac{s^2}{2dt} \cdot 2t = D \cdot 2t \quad (2.18)$$

can be described with the diffusion constant $D = \frac{s^2}{2dt}$. Expanding this expression to three dimensions, this results in the total mean squared displacement of

$$\langle r(t_i)^2 \rangle = \langle x(t_i)^2 \rangle + \langle y(t_i)^2 \rangle + \langle z(t_i)^2 \rangle = 3i \cdot s^2 = 6D \cdot t \quad (2.19)$$

The characteristic diffusion length

$$l = \sqrt{\langle r^2(t_i) \rangle} = \sqrt{6D \cdot t} \quad (2.20)$$

is described by the square root of the mean squared displacement. The probability distribution with discrete time steps is shown schematically in figure 2.7. However, after a sufficient number of scattering events, the random walk of the

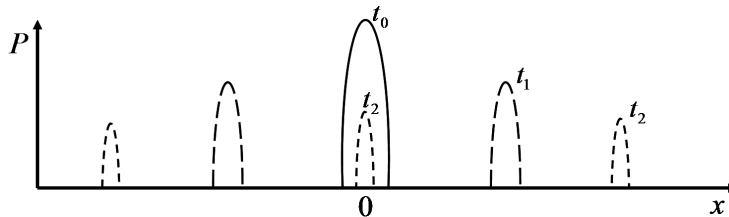


Figure 2.7: Schematic illustration of the probability of finding a photon within the random walk model at certain time steps t_i .

photon and the diffusion theory deliver the same result.

In order to consider interference effects of light waves, the description based on the diffusion equation and the random walk are not sufficient. However, to implement this, the explicit propagation of the electromagnetic wave has to be considered, i.e. its coherence properties. As well as for the electrons, the coherence of light is conserved for elastically scattered waves at stationary, yet spatially varying potential fluctuations, i.e. changes in the refractive index. The coherence length ξ_{coh} is the characteristic length scale on which interference effects occur. For distances larger than the coherence length, the information about its initial phase is destroyed by inelastic scattering at phonons etc. Experimental confirmation of the influence of disorder in a system on the propagation properties of light was observed by Schwartz et al [13]. Within his experiment, the transition from ballistic transport to diffusive propagation of light in the presence of disorder is observed. In the case of strong disorder, even the transition to localization based on constructive interference is observed.

In order to take interference properties into account a theory based on Maxwell's equations will be introduced in the following.

2.2.3 Propagation of light waves

The propagation of electromagnetic waves, i.e. light, is fully described by the electromagnetic wave theory as formulated by Maxwell. The four Maxwell equations

$$\nabla \vec{E} = \frac{\rho}{\varepsilon} \quad (2.21)$$

$$\nabla \vec{B} = 0 \quad (2.22)$$

$$\nabla \times \vec{E} = -\frac{\partial \vec{B}}{\partial t} \quad (2.23)$$

$$\nabla \times \vec{B} = \mu \vec{j} + \varepsilon \mu \frac{\partial \vec{E}}{\partial t} \quad (2.24)$$

with $\varepsilon = \varepsilon_0 \varepsilon_r$ and $\mu = \mu_0 \mu_r$ describe the spatial and temporal evolution of \vec{E} and \vec{B} and allow to consider coherence properties of electromagnetic waves. The general validity of the Maxwell equations enables the calculation of various phenomena of classical electrodynamics. Here I will concentrate on the behaviour of the propagation of electromagnetic waves in spatially homogeneous and inhomogeneous media. Therefore in the following the wave equation is developed from the Maxwell equations.

The wave equation in homogeneous media can directly be retrieved from the Maxwell's equations. In homogeneous media, the permittivity $\varepsilon_r(\vec{r}) = \varepsilon_r = \text{const}$ and permeability $\mu_r(\vec{r}) = \mu_r = \text{const}$ is position independent. By assuming a charge free medium, i.e. $\rho = 0$ and $\vec{j} = 0$, the curl of equation 2.23 leads to

$$\begin{aligned} \nabla \times (\nabla \times \vec{E}) &= -\nabla \times \frac{\partial \vec{B}}{\partial t} \\ \underbrace{\nabla(\nabla \cdot \vec{E})}_{=0} - \Delta \vec{E} &= -\frac{\partial}{\partial t} \nabla \times \vec{B} \\ -\Delta \vec{E} &= -\frac{\partial^2}{\partial t^2} \varepsilon \mu \vec{E} \end{aligned} \quad (2.25)$$

which could be written as

$$\Delta \vec{E} - \frac{n^2}{c^2} \frac{\partial^2}{\partial t^2} \vec{E} = 0 \quad (2.26)$$

using the relations for the speed of light $1/c^2 = \varepsilon_0 \mu_0$ and for the index of refraction $n^2 = \varepsilon_r \mu_r$. The solutions of the wave equation are plane waves described by

$$E(\vec{r}, t) = \vec{E}_0 e^{i(\vec{k}\vec{r} - \omega t)} \quad (2.27)$$

which is the same solution as the solution for the Schrödinger equation. In contrast, the dispersion relation for electromagnetic waves

$$\omega = \frac{ck}{n} \quad (2.28)$$

differs from the dispersion relation for matter waves as described by equation 2.8.

This close relation of the Schrödinger equation to the wave equation in electrodynamics allows to transfer the theory developed for the localization of electrons to the localization of photons, i.e. light [8, 9].

The wave equation in inhomogeneous media can also be retrieved directly from Maxwell's equation. In the case of an inhomogeneous media the spatial position influences the electromagnetic wave, described by the position dependent permittivity $\varepsilon_r(\vec{r})$ and permeability $\mu_r(\vec{r})$. In the following, the permeability is not considered, i.e. $\mu_r(\vec{r})=1$, assuming non magnetic media. Therefore, the refractive index is determined by $n(\vec{r})^2 = \varepsilon_r(\vec{r})\mu_r(\vec{r}) = \varepsilon_r(\vec{r})$.

The dependence of the spatial position of $\varepsilon_r(\vec{r})$ using the first Maxwell equation in 2.21 in a charged free medium $\rho = 0$ leads to

$$\nabla \varepsilon(\vec{r}) \vec{E}(\vec{r}) = \vec{E}(\vec{r}) \nabla \varepsilon(\vec{r}) + \varepsilon(\vec{r}) \nabla \vec{E}(\vec{r}) = \rho = 0 \quad (2.29)$$

By assuming a non-conductive medium ($\sigma = 0$) the curl of equation 2.23 leads to

$$\begin{aligned}
\nabla \times (\nabla \times \vec{E}) &= -\nabla \times \frac{\partial \vec{B}}{\partial t} \\
\nabla \left(\underbrace{\nabla \vec{E}}_{= \frac{\vec{E}(\vec{r}) \nabla \varepsilon(\vec{r})}{\varepsilon(\vec{r})}} \right) - \Delta \vec{E} &= -\frac{\partial}{\partial t} \nabla \times \vec{B} \\
\nabla \frac{\vec{E}(\vec{r}) \nabla \varepsilon(\vec{r})}{\varepsilon(\vec{r})} - \Delta \vec{E} &= -\frac{\partial^2}{\partial t^2} \varepsilon \mu \vec{E} \quad . \quad (2.30)
\end{aligned}$$

This can be written as

$$2\nabla \left(\frac{\vec{E}(\vec{r}) \nabla n(\vec{r})}{n(\vec{r})} \right) - \Delta \vec{E} - \frac{n^2}{c^2} \frac{\partial^2}{\partial t^2} \vec{E} = 0 \quad (2.31)$$

by using $n(\vec{r}) = \sqrt{\varepsilon(\vec{r})\mu(\vec{r})}$ and $\frac{\nabla n(\vec{r})^2}{n(\vec{r})^2} = \frac{2n(\vec{r}) \nabla n(\vec{r})}{n(\vec{r})^2}$. The solution of equation 2.31 is explicitly dependent on the spatial change of the refractive index.

A waveguide with a stepwise change in the refractive index $n(\vec{r})$ is one example for inhomogeneous media. The stepwise change of the refractive index, however, leads to problems in the derivation of the refractive index in equation 2.31 [52]. Solution strategies are known from quantum mechanics and a particle in a finite potential well [53]. If the diameter of the inner waveguide is much smaller than the wavelength, the wave is not trapped anymore. In this case, the spatial variation in the refractive index acts only as a scattering source.

Much more complex problems, like randomly distributed scattering objects, can be calculated by Finite Difference Time Domain (FDTD) calculations [98]. They are used to calculate time dependent differential equations in section 3.2.4.

2.2.4 Localization of light induced by interference

Another possibility for the localization of electromagnetic waves, apart from the localization within a structure due to large spatial distortions of the refractive index, is based on the constructive interference of waves. An inhomogeneous spatial distribution of the refractive index with a diameter in the sub-wavelength region acts as a scattering source. This is known as Rayleigh scattering [108]. The scattered waves can interfere with each other resulting in Anderson localization [13, 41].

To understand the behaviour of propagating waves and the interference of multiply scattered waves, the individual wave trajectories have to be considered. In general, there is a countless number of different propagation trajectories which all have to be taken into account. The propagation from a point A to a point B using different trajectories is schematically illustrated in figure 2.8. However, within the quantum mechanical approach it is not possible to deduce the exact position of the propagating photon. Therefore the exact propagation path of the i -th propagation trajectory can only be determined by its probability amplitude p_i . The total probability of a photon getting from A to B is described by the square of the absolute value when considering the sum over all probability

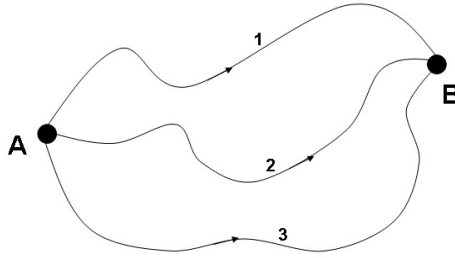


Figure 2.8: Schematic illustration of the propagation of light. The light is scattered and propagates from point A to B using different propagation trajectories.

amplitudes:

$$\begin{aligned}
 P_{total} &= \left| \sum_i p_i \right|^2 \\
 &= \sum_i |p_i|^2 + \sum_{i \neq j} p_i p_j^* = 1.
 \end{aligned}
 \tag{2.32}$$

The classical transport and diffusion theory is based on the propagation of photons described as classical particles without considering their phase relations. Therefore the first term in equation 2.32 describes the classical diffusion. The second term is the quantum-mechanical contribution which describes the interference of two different propagation trajectories i and j . This second term is neglected within the classical transport theory. This quantum-mechanical contribution describing the interference is essential to understanding the weak localization phenomenon.

The Weak localization is one of the most famous indirect experimental confirmations of the localization of electromagnetic waves. It was first discovered by van Albada and Lagedijk [18] and by Wolf and Maret [19] who illuminated strong scattering sub-micron-size polystyrene spheres with light in the visible spectral range. Similar results were obtained ten years later by Wiersma who also observed coherent backscattered light from amplifying random Ti:Sapphire powders [58].

During these experiments, it was observed that for the same position of radiation source and detector, the signal was two times higher compared to larger backscattering angles. This phenomenon is called enhanced coherent backscattering and is based on the coherent interference of propagating light of different wave trajectories within strongly scattering media.

In order to investigate this phenomenon in more detail, the different scattering trajectories in an array of randomly distributed spheres are analysed. One possible example from a countless number of random propagation trajectories is schematically illustrated in figure 2.9a. The electromagnetic wave can propagate clockwise or counter clockwise along the given trajectory indicated by the red and green lines. The light scattering is assumed to be elastic. Many different scattering paths contribute to the backscattered intensity. Variations in the different path length of the scattering trajectories lead to different phases and therefore to constructive and destructive interferences. These typically cancel

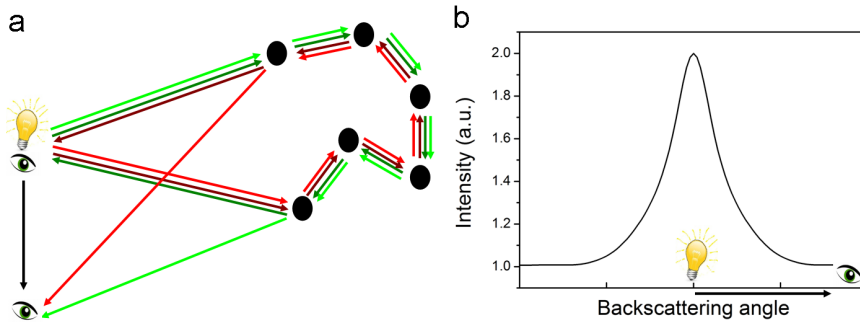


Figure 2.9: **a** Schematic illustration of coherent backscattering. Multiply scattered light is detected as a function of the backscattering angle resulting in the coherent backscattering cone shown in **b**.

out over ensembles of backscattering trajectories and a smearing of the speckle pattern becomes visible. Only the trajectory propagating in the opposite direction on a given trajectory (time reversal) has the same phase and survives the averaging.

This was verified by measuring the backscattered light as a function of the backscattering angle [58], i.e. the angle between radiation source and detector, as depicted by the electric bulb and the eye in figure 2.9**b**. At a backscattering angle of zero degrees, the scattering trajectory and its time reversal path have the same phase and they coherently add up (constructive interference).

These observations are supported by the calculation of the probability of different trajectories by equation 2.32. Now, the probability p_1 describes the light propagating clockwise and p_2 the light propagating counter clockwise. For the case that origin and end of the trajectory are at the same place, both the clock- and counter clockwise propagation have the same phase. This results in $p_1 = p_2 = p$. By using equation 2.32 this results in the probability of:

$$\begin{aligned} P_0 &= 2|p|^2 + p_1 p_2^* + p_1^* p_2 \\ &= 4|p|^2 \end{aligned} \quad (2.33)$$

If the origin and the end of the trajectories are separated in space, they have a nonzero phase difference resulting in constructive and destructive interference and the averaging of both waves. Hence we can neglect the contribution of the interference in equation 2.32. The result is described by

$$P_\alpha = 2|p|^2 \quad (2.34)$$

and corresponds to the classical transport theory. This result supports the doubled intensity observed within the coherent backscattering measurements at zero degrees [58]. Coherence has to be conserved during all scattering processes, so elastic scattering is an essential criterion for coherent backscattering. The closed loops induced by the multiple coherent scattering reduce the diffusion of the system to a non classical behaviour. This leads to a deviation from the classical random walk. A loss of coherence during the scattering process would destroy the interference of phase matched time and time reversal paths of

multiply scattered waves. The weak localization and the coherent backscattering cone are therefore precursors for the Anderson localization.

Anderson localization of light has recently received a lot of attention in different experimental observations. In 2006 Störzer et al. [54] presented time-resolved transmission experiments of light through strongly scattering samples. They observed deviations from classical diffusion which could not be explained by absorption. The deviation strongly depends on the mean free path length. For a short mean free path length, the deviation is much stronger than expected for a phase transition in the approach of Anderson localization. This observation was supported by the work of Schwartz et al [13] in 2007. They reported about Anderson localization in disordered 2-dimensional photonic lattices and observed the transition from ballistic to diffusive propagation for increasing disorder and the Anderson localization of photon modes.

In 2010 Sapienza et al [12] used disordered photonic crystal waveguides to generate strongly confined Anderson-localized cavity modes. The Anderson localized photon mode enhanced the light emission from an embedded semiconductor quantum dot in the waveguide strongly. In general, this allows the use of disordered photonic media for quantum information devices.

The localization of electromagnetic waves is not limited to light, as explained earlier. The Anderson localization is a general wave phenomenon as established in the selection of recent publications presented in the following.

The localization of surface plasmon polaritons was given in 1999 by Gresillon et al [11]. They reported about Anderson localized surface plasmon modes in a semi continuous metal film leading to optical excitation from sub-wavelength areas. These strongly confined local electric fields, with huge fluctuations (hotspots) compared to the surrounding in combination with typical resonance peaks in the near field spectra, were observed. In 2000 Stockman predicted fluctuations of local electric fields [27]. He calculated rough surfaces and F metal nano-particles excited by femtosecond laser pulses. The fluctuations of the local electric fields were predicted to occur on femtosecond time scales and clearly show enhanced lifetimes compared to the exciting laser pulse. Confined to nanometer-size regions, the spatial distribution of those fields dramatically changes as a function of time and differs highly from a steady-state excitation.

Localization of acoustic waves can be considered as the localization of a longitudinal wave in contrast to the transverse wave, i.e. light. Nevertheless, the localization caused by constructive interference also occurs in acoustics as described by Hu et al [10] for localization of ultrasound in a three-dimensional elastic network. They reported about the first "transverse localization" in three dimensions by studying the time-dependent transmission of ultrasound waves below the mobility edge for aluminum scattering spheres of different diameters.

2.2.5 Single scaling theory

The single scaling theory was introduced by Abrahams in 1979 [72]. Within this theory, the complex physics of localization is expressed in a single scalar, the single scaling parameter g . This value allows to classify the strength of localization based on electric field fluctuations into localized and delocalized regimes as demonstrated by Riboli et al. [61]. Here, the theory does not distinguish between different localization mechanisms or microscopic details anymore. All these properties are completely determined by g . Abrahams deduces the dimensionless scaling parameter g in a d -dimensional hyper cube with the side length L :

$$g = \left(\frac{e^2}{\hbar}\right)^{-1} \cdot \frac{1}{R} = \left(\frac{e^2}{\hbar}\right)^{-1} \sigma L^{d-2} \quad . \quad (2.35)$$

Therein R is the resistance, e the elementary charge and σ is the classical conductivity.

In 1975 already Thouless discussed the explicit dependance of g on the side length L of the investigated system (cube) in a paradigm-setting work [45, 59]. Within this approach localized or delocalized Eigenfunctions are set to the centre of the hyper-cube. For metallic behaviour the conductivity σ is length-independent per definition. This assumption corresponds to the extended wave functions (delocalized Eigenfunctions) in metallic solid states [51]. Therefore $g \propto L^{d-2}$. This dependency on the length and the dimension of the system, indicated by equation 2.35, leads to a high sensitivity to changes in the boundary conditions by increasing the cube size L . In the case of insulating behaviour, the wave function is not extended over the solid state. It localizes due to the small extent of the wave function and shows an exponential relation to the expansion. Localized states are not sensitive to changes in the boundaries of a sample as long as $L > \xi$ is fulfilled [44].

In-between localized and delocalized states, there is a critical value of $g = g_c$ which describes the transition from one behaviour to the other. At this transition the dimensionless value g becomes independent of the scale of the investigated system, i.e. g_c is scale-invariant [45].

Due to the exponential decrease of the localized mode, a characteristic length can be defined. Beyond this length, which is given by the localisation length ξ (section 2.1.2), the mode can be neglected [44]. For the investigation of the degree of localization of a given system, the system is divided in b^d d -dimensional cubes (b the number of cubes) with the edge length L . The scaling parameter $g(bL)$ of the newly compounded big cube with the total side length $b \cdot L$ is now a function f of $g(L)$ and b involving any additional values describing the microscopic structure. Abrahams et al. assumed that the new system can be described by the single scaling parameter g of a single cube neglecting all the microscopic details [72]:

$$g(bL) = f[b, g(L)]. \quad (2.36)$$

By using equation 2.36 the so called renormalization group scheme [45] is estimated to

$$g(L) = f[b, g(L/b)] \quad . \quad (2.37)$$

Using these equations, the β function is now defined by

$$\beta(g) = \frac{d \ln(g)}{d \ln(L)} \quad . \quad (2.38)$$

The β function describes the change of the single scaling parameter as a function

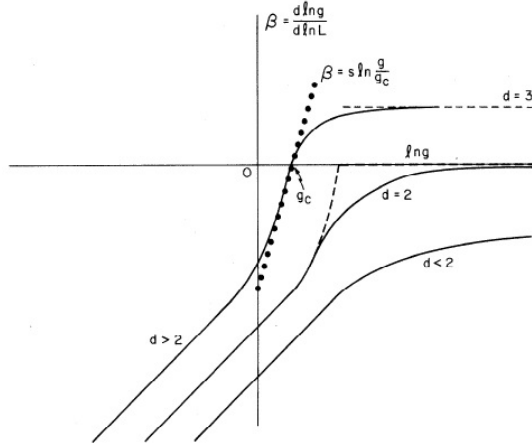


Figure 2.10: Plot of $\beta(g)$ vs $\ln(g)$ published by Abrahams et al. [72]. The figure presents the change of the single scaling parameter g as a function of the system size L . It allows to distinguish between localized ($\beta < 0$) and extended states ($\beta > 0$) for different dimensions d of the system under investigation.

of the system size L shown in figure 2.10. It depends strongly on the dimension of the system.

For $d = 1$ and $d = 2$ the β function is always negative or equal to zero. This corresponds to localized states. Increasing L always leads to a decrease of g and therefore to an insulating behaviour. As indicated by figure 2.10, there is always localization for one-dimensional and even two-dimensional systems. Within these systems, there will never be purely extended states.

For the case of $d > 2$, localized as well as delocalized states can exist. This is indicated by the zero crossing of β at the critical conductance $g = g_c$. In the region of $g > g_c$ an increase of L leads to an increase of the single scaling parameter. Thus the sample leans toward a conducting behaviour. For $g < g_c$ the increasing sample size again decreases the conductance and leads to insulating behaviour.

A different approach for the single scaling parameter can be deduced by looking at the spectrum of electromagnetic modes [62]. Electromagnetic modes can be described by their spectral width $\delta\omega$ and the average frequency spacing to neighbouring modes $\Delta\omega$. The degree of spectral mode overlap is expressed by the dimensionless single scaling parameter

$$g = \frac{\delta\omega}{\Delta\omega} \quad . \quad (2.39)$$

This results in two different scenarios:

1. $\delta\omega \gg \Delta\omega \Rightarrow g > 1$ Electromagnetic modes with diffusing behaviour correspond to extended modes. Therefore, the energy does not persist in the sample (cube). It dissipates through the boundaries of the cube. This results in a short lifetime of the mode and a corresponding broad spectral line width. In this case, the spectral width of the mode $\delta\omega$ exceeds the spectral average spacing between neighbouring modes allowing the Eigenstate to couple to the Eigenstates of the surrounding neighbours easily. The overlap of the Eigenstates create a new wave function which is extended across the sample. This behaviour tends to $g \rightarrow \infty$ and can be considered to be a perfect conductor for electrons, or to be transparent for light.

2. $\delta\omega \ll \Delta\omega \Rightarrow g < 1$ In contrast to that, an exponentially spatially localized mode preserves the energy within the cube. This results in a long lifetime and a corresponding sharp spectral line width. The sharp spectral width leads to a small overlap with adjacent Eigenfunctions and coupling is ineffective. The formation of an extended new wave function is nearly impossible. This behaviour tends to $g \rightarrow 0$ and is comparable to a perfect insulator, i.e. intransparent for light not considering absorption.

The single scaling parameter g may also be used as a quantitative measure of the degree of localization as shown by Nieuwenhuizen and van Rossum [63]. They introduced a model to describe the intensity distribution of waves transmitted through multiple scattering media. This semi-analytical model describes fluctuations in the total transmission through a three-dimensional scattering medium that couples to different input modes.

Then the probability $P(I_{norm})$ to find the normalized intensity $I_{norm} = \frac{I}{\langle I \rangle}$, i.e. the intensity normalized to the average intensity $\langle I \rangle$, of the scattered and transmitted electromagnetic field is given as a function of g .

$$P(I_{norm}) = \int_{-i\infty}^{i\infty} \frac{1}{2\pi i} e^{x I_{norm} - \Phi(x)} dx \quad (2.40)$$

The function $\Phi(x)$ is called the generation function and is assumed to be an incident plane wave $\Phi(x) = \Phi_p(x)$ or an incident Gaussian wave $\Phi(x) = \Phi_g(x)$.

$$\Phi_p(x) = g \cdot \ln \left(\sqrt{1 + \frac{x}{g}} + \sqrt{\frac{x}{g}} \right)^2 \quad (2.41)$$

$$\Phi_g(x) = g \int_0^{-1} \frac{1}{y} \ln \left(\sqrt{1 + \frac{x}{g}} + \sqrt{\frac{x}{g}} \right)^2 dy \quad (2.42)$$

The corresponding probability distributions for the case of a Gaussian incident wave are shown in figure 2.11 for different values of g . The intensity distribution strongly depends on the scaling parameter g . For large values of g , the distribution is close to a Gaussian distribution centered around $I / \langle I \rangle = 1$. In contrast, for small values of g , the distribution is described by a log-normal distribution. For this case, the distribution is much broader due to the increasing probability for high intensity values.

In-between these two limiting cases, a characteristic transition from the Gaussian distribution towards the log-normal distribution can be seen. Based on this theory, localization ($g < 1$) is expected to show large fluctuation in the intensity.

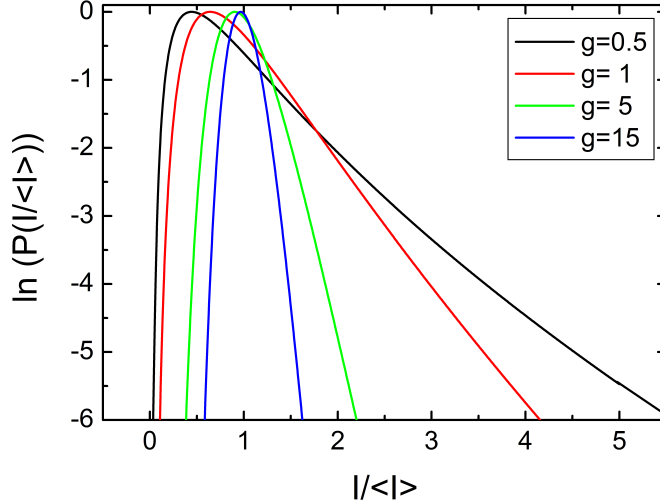


Figure 2.11: Intensity distributions of a Gaussian wave at different values of the single scaling parameter g . The intensity values are Gaussian distributed for large values of g , whereas low values of g allow larger intensities, which results in a log-normal distribution.

Therefore the single scaling theory can be used to classify the localization strength. This has been verified experimentally by comparing the intensity distribution emitted from samples to the calculated distribution of different values of g [36, 61]. The best fitting distribution classifies the localization strength by using the corresponding value of g .

2.2.6 Multifractality

The localization strength can alternatively be investigated based on a multifractal analysis [36, 64, 65]. Therefore the distribution of a measure P on a geometric carrier (for example a spatially or temporally resolved measurement) is divided in (fractal) sub distributions of small boxes B with length l_{box} . Each of these boxes can then be described by a different Hölder exponent

$$\alpha = \lim_{l_{box} \rightarrow 0} \frac{\log P(l_{box})}{\log l_{box}} . \quad (2.43)$$

The Hölder exponent is also called singularity strength and describes the scaling of the probability, i.e. the fluctuations within a box. For different boxes, the Hölder exponent produces different values. The distribution of the Hölder exponents results in the singularity spectrum $f(\alpha)$, also called fractal dimension or Hausdorff dimension. Therefore the multifractal analysis delivers the singularity spectrum which describes the dynamic of the measure. The singularity spectrum allows to give any metric structure a fractal dimension. A system can be called fractal in character, if the fractal dimension is unequal to the real dimension of the investigated system.

In many cases, the calculation of the singularity spectrum is affected by numerical errors. One possibility to avoid the occurrence of numerical errors when calculating the singularity strength α and the singularity spectrum $f(\alpha)$ was developed by A. Chabra and R.V. Jensen [64]. This method is demonstrated in the following by an example of randomly generated values, spatially arranged in a two-dimensional distribution ($N \times M$ pixel) which represents a map of local intensities $I(x, y)$. Each intensity value corresponds to a single box described by the theory. Thereby, the single box size l_{box} is a fixed value given by the resolution of $I(x, y)$. The values $I(x, y)$ in figure 2.12a are Gaussian distributed² and the values in figure 2.12b are log-normal distributed³ as can be seen in the corresponding histograms in figure 2.12c and d.

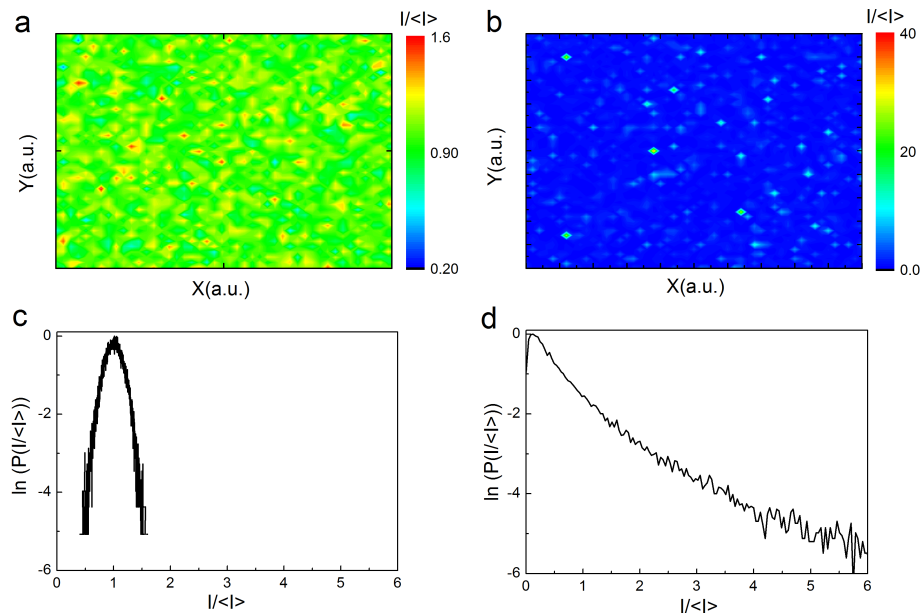


Figure 2.12: Spatial random intensity distributions for **a** Gaussian distributed values and **b** log-normal distributed values normalized to the mean intensity. The corresponding histograms are shown in **c** and **d**.

For the multifractal analysis, the data has to be vectorized $I(x, y) \rightarrow I_{vec,j}$ with j being the index of the vector ranging from $j = 1, 2, \dots, N \cdot M$ with $N \cdot M$ as the total number of elements of $I(x, y)$. In order to consider the original dimension, which gets lost by the transformation from the matrix to the vector representation of the data, L^* is set for a two dimensional quadratic scan to

$$L^* = \sqrt{L} = \sqrt{M \cdot N} \quad (2.44)$$

with L being the length of I_{vec} or simply to the side length N , assuming $M = N$. Within the theory, the probability P_j of finding the intensity I_j within a single

²normal distribution with a mean value of 1 and the standard deviation $\sigma = 0.25$ with 40,000 data points

³log-normal distribution with a mean value of 1 and the standard deviation $\sigma = 1.2$ with 40,000 data points

box is given by:

$$P_j = \frac{I_j}{\sum_j I_j} \quad (2.45)$$

with $\sum_j P_j = 1$. The probability to find a certain intensity value in a box with size l_{box} is then given for a one parameter family in q of normalized data by $\mu(q)$.

$$\mu_j(q) = \frac{P_j^q}{\sum P_j^q} \quad (2.46)$$

The parameter q acts like a "microscope" for exploring different regions of the singular measure [64]. For $q > 1$, the regions of stronger singular strength (regions with strong fluctuations) of P_j are amplified by $\mu_j(q)$, whereas for $q < 1$ it delivers insight into regions of weak singularity strength (regions of weak fluctuations) of P_j .

With this microscope parameter q , a relationship between the dimensionality and therefore the localization strength and the singularity strength, can be provided. The singularity spectrum $f(q)$ is associated with the fractal dimensionality by a Legendre transformation. It is calculated with:

$$f(q) = \frac{\sum \mu_j(q) \ln[\mu_j(q)]}{\ln(L^*)} . \quad (2.47)$$

The singularity strength $\alpha(q)$ is described by:

$$\alpha(q) = \frac{\sum \mu_i(q) \ln[P_i]}{\ln(L^*)} . \quad (2.48)$$

The singularity spectrum $f(q)$ and the singularity strength $\alpha(q)$ are connected by q . It is obvious, that for $q = 1$, $f(q)$ and $\alpha(q)$ have the same values, i.e. an intersection point can be seen if plotted as a function of q as shown in figure 2.13 for the generated Gaussian and log-normal spatial intensity distributions. The

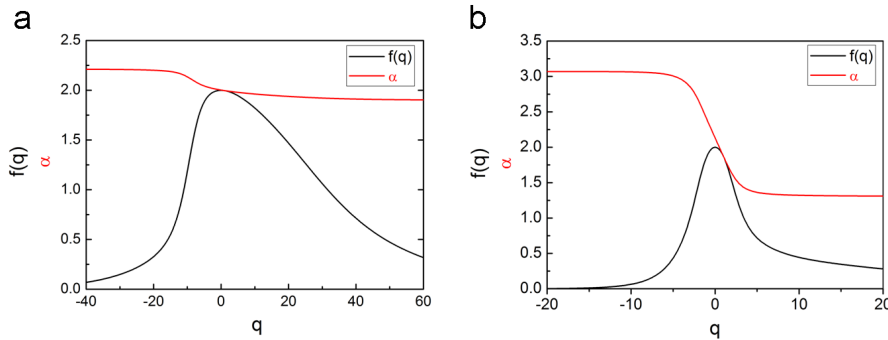


Figure 2.13: The figure shows the singularity spectrum $f(q)$ and the singularity strength α for a Gaussian **a** and a Log-normal distribution **b**.

singularity spectrum always has a maximum at $q = 0$. The corresponding value of the singularity strength determines the localization strength. By simply plotting $f(q)$ over $\alpha(q)$, the singularity spectrum $f(\alpha)$ can be estimated as shown

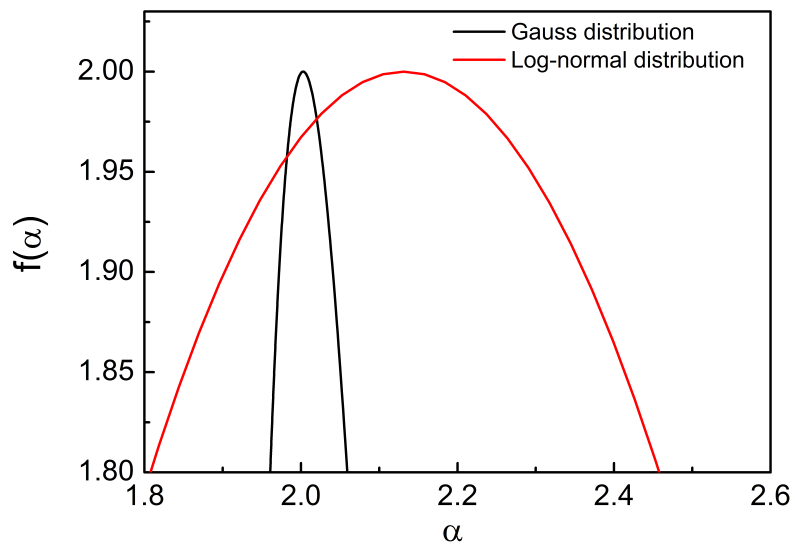


Figure 2.14: Singularity spectrum $f(\alpha)$ of a multifractal analysis of a Gaussian and a log-normal two-dimensional spatial intensity distribution. The singularity spectrum for the Gaussian distribution is centered around $\alpha_0^{gauss} = 2$, whereas the maximum in the singularity spectrum of the log-normal distribution is shifted to higher values of $\alpha_0^{log} \approx 2.1$. In addition, the spectral width is much broader for the log-normal distribution compared to the Gaussian distribution.

in figure 2.14. For a Log-normal distribution, the $f(\alpha)$ singularity spectrum gets broadened with a maximum in the spectrum at a singularity strength of $\alpha_0^{log} \approx 2.1$. In contrast, the spectral width of $f(\alpha)$ is narrowed for the Gaussian distribution and the spectrum is centered at $\alpha_0^{gauss} = 2$. This corresponds to the dimension of the two-dimensional intensity distribution. The strong deviation in the spectral width of $f(\alpha^{log})$ is due to the much stronger fluctuation in the intensity distribution. This results in a larger spread of the Hölder exponent.

In conclusion, this allows the classification of intensity distributions in terms of their localization strength by using the multifractal analysis and the analysis of the maximum of the singularity spectrum $f(\alpha)$. Experimentally, this has been demonstrated by Richardella et al [36]. They observed strong spatial fluctuations of the local conductivity on doped $Ga_{1-x}Mn_xAs$ in the two-dimensional STM measurement. Within these measurements, the singularity spectrum shows a strong shift of its maximum to $\alpha_0 = 2.1$ corresponding to a single scaling parameter of $g < 1$.

2.3 Light matter interaction

In a classical manner, light-matter interaction is the excitation of charges in a matter by an oscillating electromagnetic field.

Quantum mechanically, electromagnetic fields couple to discrete quantum states of the matter [66].

In the following, a semi-classical approach is discussed. Within this approach, the light matter interaction consider the discrete quantum states of the matter. However, it does not consider changes in the exciting electromagnetic field. Semi-classical, the light field is not influenced by absorption. This approach is justified, if the excitation is sufficiently strong allowing to neglect changes in the light field, induced by the interaction.

The spectroscopic behaviour of the states can be calculated by using the semi-classical approach in combination with time-dependent optical Bloch equations. This gives insight into the time dynamics of photon modes. Therefore a model based on the density matrix formalism is introduced in the following to describe the temporal evolution of a system (section 2.3.1), i.e. a single localized photon mode.

In the case of strongly confined photon modes with sufficient field strength (hotspot), this can result in nonlinear light matter interaction. Nonlinear light matter interaction enables the examination of the temporal behaviour of localized photon modes [88] (section 2.4).

A single localized mode in terms of Anderson localization within a random media can be described by a two-level system. The system consists of a ground state $|0\rangle$ and an excited state $|1\rangle$. An external electromagnetic field couples to the ground state $|0\rangle$ and excites the electron by a dipole allowed transition to the excited state $|1\rangle$, as illustrated in figure 2.15.

The system can then be described by the wave function

$$\psi = a|0\rangle + b|1\rangle \quad (2.49)$$

with a,b as the amplitude of the both states. The temporal evolution of the

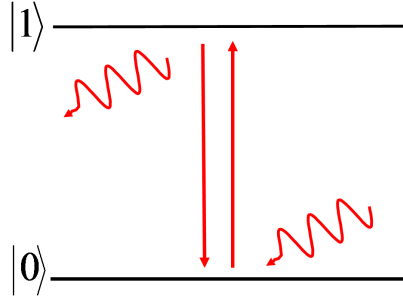


Figure 2.15: Coupling of an electromagnetic wave to a two level system consisting of a ground state $|0\rangle$ and an excited state $|1\rangle$. Both absorption of an electromagnetic wave and the emission of the wave are allowed.

system is described by the Schrödinger equation 2.6.

2.3.1 Density matrix

By using the Schrödinger equation, which describes the time evolution of pure quantum states, the dynamic of mixed states can easily be derived [53]. To achieve this the density matrix is splitted into pure states which fulfill the dynamic of the Schrödinger equation. Consequentially the dynamic of the mixed state can be calculated by the Liouville-von-Neumann equation as explained in the following.

Within a mixed state, the phase relation of the states is unknown, so that it is not possible to write them as a linear combination of pure states. However, it is possible to indicate the probability p_i to find the system in the pure state $|\psi_i\rangle$. In the case of mixed states, the density matrix for our system is described by

$$\rho = \sum_i p_i |\psi_i\rangle \langle \psi_i| \quad . \quad (2.50)$$

For pure states, the density matrix results in

$$\rho = |\psi_i\rangle \langle \psi_i| \quad (2.51)$$

with ψ as the total wave function of the two-level system. The corresponding density matrix is described by

$$\rho = (a|0\rangle + b|1\rangle)(a^*\langle 0| + b^*\langle 1|) \quad . \quad (2.52)$$

Multiplication from left and right with the ground and the excited states leads to different elements of the density matrix

$$\rho = \begin{pmatrix} \rho_{00} & \rho_{01} \\ \rho_{10} & \rho_{11} \end{pmatrix} = \begin{pmatrix} |a|^2 & ab^* \\ a^*b & |b|^2 \end{pmatrix} \quad (2.53)$$

that describes the population of the ground state ρ_{00} and of the excited state ρ_{11} as the diagonal elements. The off-diagonal elements $\rho_{01} = \rho_{10}^*$ describe the coherence terms between the two states.

2.3.2 Optical Bloch equation

The temporal evolution of a system can be obtained by solving the Liouville-von-Neumann equation.

$$\dot{\rho} = \frac{i}{\hbar} [H, \rho] = \frac{i}{\hbar} (H\rho - \rho H) \quad (2.54)$$

Solving this equation of motion results in the temporal evolution of all matrix elements, which gives complete information about the temporal evolution of the polarisation and population.

The undisturbed Hamiltonian of a two level system is described by the Eigenfrequencies of the ground state ω_0 and the excited state ω_1 :

$$H_0 = \begin{pmatrix} \hbar\omega_0 & 0 \\ 0 & \hbar\omega_1 \end{pmatrix} . \quad (2.55)$$

Based on the Liouville von Neumann equation 2.54, the equation of motion looks like this:

$$-i\hbar \frac{\partial}{\partial t} \begin{pmatrix} \rho_{00} & \rho_{01} \\ \rho_{10} & \rho_{11} \end{pmatrix} = \begin{pmatrix} 0 & (\omega_0 - \omega_1)\rho_{01} \\ (\omega_1 - \omega_0)\rho_{10} & 0 \end{pmatrix} . \quad (2.56)$$

In the absence of external influences, the undisturbed system does not show any changes in the population. It only shows changes in coherence of the two-level system.

The influence of damping, i.e. the relaxation of the population from the excited state to the ground state, is considered by implementing a relaxation rate $\Gamma_1 = 1/T_1$, which is determined by the lifetime of the excited state T_1 . By considering the conservation of the total population, changes of the ground state population are connected to the changes of the excited state $\dot{\rho}_{00} = \Gamma_1\rho_{11} = -\dot{\rho}_{11}$. These contributions are added to the Liouville equation of the undisturbed system which reads as

$$-i\hbar \frac{\partial}{\partial t} \begin{pmatrix} \rho_{00} & \rho_{01} \\ \rho_{10} & \rho_{11} \end{pmatrix} = \begin{pmatrix} \Gamma_1\rho_{11} & (\omega_0 - \omega_1)\rho_{01} \\ (\omega_1 - \omega_0)\rho_{10} & -\Gamma_1\rho_{11} \end{pmatrix} . \quad (2.57)$$

To include possible dephasing between the two states, for example induced by electron-electron or electron-phonon coupling, the Liouville von Neumann equation has to be extended to a more general form. The polarisation of the excited state is changed by the rate $\Gamma_2 = 1/T_2$ with T_2 as the dephasing time. The dephasing time T_2 is connected to the lifetime of the excited state by $T_2 \geq 2T_1$. Due to this term, the coherence between the two states will decay exponentially at the dephasing Γ_2 . This is known as free induction decay [67]. The general form of the Liouville-von-Neumann equation considering this results in [68]

$$-i\hbar \frac{\partial}{\partial t} \begin{pmatrix} \rho_{00} & \rho_{01} \\ \rho_{10} & \rho_{11} \end{pmatrix} = \begin{pmatrix} \Gamma_1\rho_{11} & (\omega_0 - \omega_1)\rho_{01} - \Gamma_2\rho_{01} \\ (\omega_1 - \omega_0)\rho_{10} - \Gamma_2\rho_{10} & -\Gamma_1\rho_{11} \end{pmatrix} . \quad (2.58)$$

So far the system is undisturbed, i.e. external forces are not taken into account. In a next step, the influence of an external electromagnetic field is considered. The spatial extent of the two-level system is assumed to be much smaller than the wavelength of the incident electromagnetic field. In the case of single atoms

or nano-structures, this criterion is justified by more than two orders of magnitude using excitation around 800 nm . This allows us to treat the light matter interaction in dipole approximation.

The Hamilton operator

$$H_1 = -\vec{d}_{kl} \cdot \vec{E}(t) \quad (2.59)$$

of the light matter interaction is expressed with the dipole moments expectation value of the dipole operator

$$\vec{d}_{kl} = \langle \Psi_k | q\vec{r} | \Psi_l \rangle \quad (2.60)$$

using the position operator r and the electric charge q . The dipole operator acts as the projection from an initial state Ψ_l to the final state Ψ_k . Considering equation 2.59 and 2.60, the light-matter interaction Hamiltonian H_1 can be expressed by

$$H_1 = \begin{pmatrix} 0 & \vec{d}_{01}\vec{E}(t) \\ \vec{d}_{10}\vec{E}(t)^* & 0 \end{pmatrix} := \begin{pmatrix} 0 & \alpha(t) \\ \beta(t) & 0 \end{pmatrix} \quad (2.61)$$

with the substitution $\alpha(t) = \vec{d}_{01}\vec{E}(t)$ and $\beta(t) = \vec{d}_{10}\vec{E}(t)^*$. The total Hamilton operator consists of the undisturbed part describing the system H_0 and the light matter interaction H_1 .

$$H_{total} = H_0 + H_1 \quad (2.62)$$

The Liouville-von-Neumann equation considering external perturbation by an electric field and additional dephasing and changes in the population of the states than reads:

$$-i\frac{\partial}{\partial t} \begin{pmatrix} \rho_{00} & \rho_{01} \\ \rho_{10} & \rho_{11} \end{pmatrix} = \begin{pmatrix} \Gamma_1\rho_{11} + \alpha\rho_{10} - \beta\rho_{01} & \hbar(\omega_0 - \omega_1)\rho_{01} - \Gamma_2\rho_{01} + \alpha(\rho_{11} - \rho_{00}) \\ \hbar(\omega_1 - \omega_0)\rho_{10} - \Gamma_2\rho_{10} + \beta(\rho_{00} - \rho_{11}) & -\Gamma_1\rho_{11} + \beta\rho_{01} - \alpha\rho_{10} \end{pmatrix}. \quad (2.63)$$

The emitted electric field $E_{loc}(t)$ from the two-level system is proportional to the induced polarisation ρ_{01} between the ground state $|0\rangle$ and the excited state $|1\rangle$. Therefore, it is now possible to apply equation 2.63 to calculate the temporal evolution of the local electric field $E_{loc}(t)$ emitted from the two-level system by using the excitation of an external field, i.e a localized photon mode described by a certain resonance frequency and dephasing time.

2.4 Interferometric Frequency Resolved Auto-Correlation and Second Harmonic microscopy

While Interferometric Frequency Resolved AutoCorrelation (IFRAC) is a technique to determine the pulse structure of ultra-short laser pulses [73], it can also be used to distinguish between coherent and incoherent emission from a sample [70]. Coherent waves have a constant relative phase allowing interference effects, whereas incoherent waves have a random phase relation. The IFRAC technique is an essential tool within this work and will be discussed in this section.

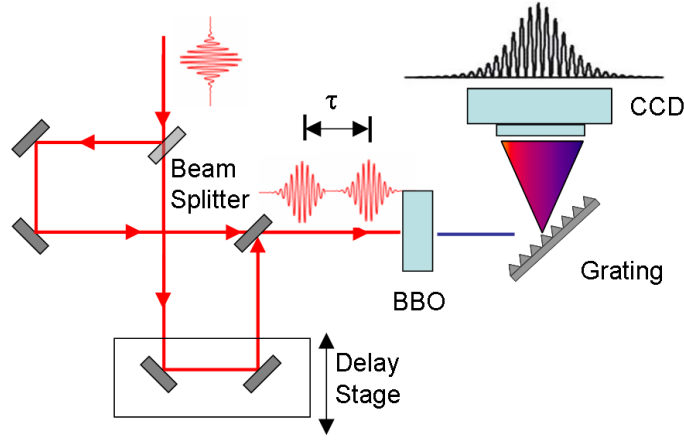


Figure 2.16: Schematical illustration of a Mach Zehnder interferometer. An incident laser pulse is splitted into the laser pulses $E(t)$ and $E(t + \tau)$ using two identical beam splitters and a variable delay stage to adjust the delay τ . Later, the nonlinear emission from a BBO crystal can be detected spectrally resolved.

The IFRAC is based on an interferometer generating a pulse pair with a variable time delay τ as illustrated in figure 2.16. The electric field for each of the laser pulses can be described by $E(t) = \varepsilon(t)\exp(i\omega_L t)$ with the amplitude $\varepsilon(t)$ and the laser frequency ω_L . The electric field behind the interferometer consists of both laser pulses which are used to excite a BBO crystal in order to generate light at the SH frequency. The generation of the SH is assumed to be instantaneously and frequency independent. This results in the electric field of the IFRAC signal

$$E_{IF}(\omega_d, \tau) = \int_{-\infty}^{\infty} (E(t) + E(t + \tau))^2 \exp(-i\omega_d t) dt \quad (2.64)$$

depending on the detection frequency ω_d and the applied time delay τ [69]. The measured intensity of the IFRAC signal

$$I_{IF}(\omega_d, \tau) = \left| \int (E(t) + E(t + \tau))^2 \exp(-i\omega_d t) dt \right|^2 \quad (2.65)$$

is given by the absolute square value of the electric field and can be seen at the detector. By expanding equation 2.65 to its single terms one obtains:

$$\begin{aligned} I_{IF}(\omega_d, \tau) = & 2 |E_{SH}(\omega_d)|^2 + 4|E_{IF}(\omega_d, \tau)|^2 \\ & + 8\cos\left[\left(\omega_0 + \frac{\omega_d}{2}\right)\tau\right] \Re\left[E_{IF}(\omega_d, \tau)E_{SH}^*(\omega_d)\exp(i\frac{\omega_d}{2}\tau)\right] \\ & + 2\cos[(\omega_0 + \omega_d)\tau] |E_{SH}(\omega_d)|^2 \quad . \end{aligned} \quad (2.66)$$

The four different terms in equation 2.66 allow to assign clearly the different appearing signals shown in an exemplarily measured IFRAC trace I_{IF} of a Beta-Barium-Borat (BBO) crystal excited by sub 10 fs Ti:Sapphire laser pulses in figure 2.17a and its Fourier transform $\tilde{I}_{IF}(\nu) = \frac{1}{\sqrt{2\pi}} \int I_{IF}(\tau) e^{-2\pi\nu\tau} d\tau$ in b.

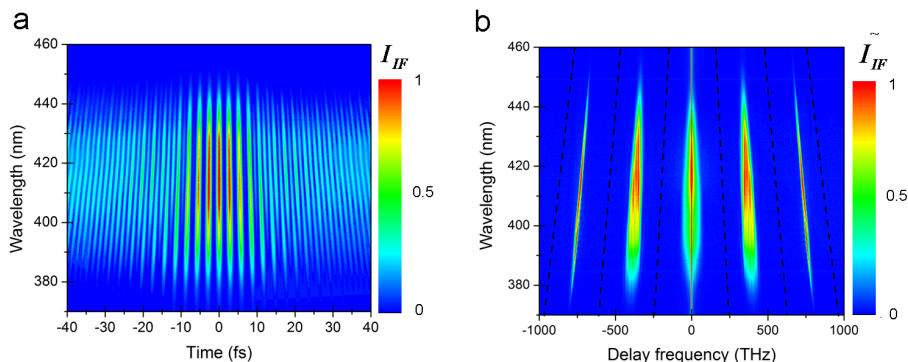


Figure 2.17: **a** IFRAC trace of a sub 10fs laser pulse **b** Fouriertransformed IFRAC trace

The first term $E_{SH} = E_{IF}(\omega_d, \tau = 0)$ describes the time delay independent second harmonic (SH) emission. The second term $|E_{FRAC}(\Delta\omega, \tau)|^2$ corresponds to a standard Frequency Resolved Optical Gating (FROG) trace [88]. These terms form the "DC-Baseband" which appears at zero delay frequency in figure 2.17b. The third term contains an oscillating cosine term which modulates the signal at $\omega_0 + \frac{\Delta\omega}{2}$. This results in the sidebands appearing in the Fourier transform at the frequency $\pm\omega_0$. Due to its oscillating behaviour at the fundamental frequency, this term is also called the fundamental modulated (FM) FROG trace. The last term is modulated at the SH frequency resulting in sidebands at $\pm 2\omega_0$ [69].

The IFRAC technique is a useful tool to retrieve the electric field $E(t)$ of the laser pulse but requires a nonlinear source of radiation as demonstrated for the emission of a BBO crystal [73, 70]. However, for measurements from samples with incoherent background emission in addition to the SH radiation, the reconstruction of the local electric field can become challenging. But even for spectral overlap of coherent and incoherent emission, the IFRAC technique still provides a clear distinction of both processes. The retrieval of these incoherently influenced measurements will be explained in the following section.

2.4.1 Distinguishing between coherent and incoherent emission processes

A direct retrieval of the electric field is sometimes rather challenging since the coherent emission is influenced by some incoherent background. In cases like this, it is necessary to separate the coherent from the incoherent emission. One way to achieve this was recently introduced based on the IFRAC technique [70]. Within this work, the spectral emission from a thin film of zinc oxide (ZnO) on a sapphire substrate was used as an example to demonstrate the potential of the IFRAC technique to distinguish between coherent and incoherent emission. The spectral emission from ZnO, illuminated by short laser pulses from a Ti:Sapphire laser operating at a central wavelength of 870 nm, consists of SH radiation, spectral clearly separated from an incoherent emission band emitted from defect states within the ZnO. The recorded spectral emission as a function of the time

delay is shown in the IFRAC trace in figure 2.18a and the corresponding Fourier transform in **b**. The coherent SH emission ranging from 380 – 460 nm shows

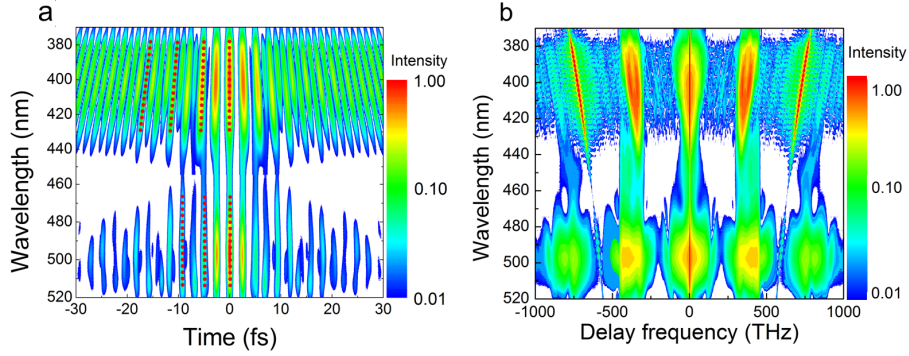


Figure 2.18: **a** IFRAC of a sub 10fs laser pulse on a thin film of ZnO. The emission consists of coherent emission (tilted red line) and incoherent emission (not tilted red line) **b** Fourier transformed IFRAC.

significantly different properties in the IFRAC trace compared to the incoherent emission around 460 – 520 nm . The origin of the incoherent emission stems from defect states within the ZnO and is known from the literature as green photoluminescence [71]. The excitation based on the ultrashort laser pulse in the near-IR requires multiphoton induced luminescence. In the case of the SH, the emission of both laser pulses has a constant phase relation, whereas the phase relation of the incoherent luminescence excited by the pulse pair is random. Within the measured IFRAC trace, detection wavelength λ_d dependent interference fringes with an oscillation period

$$T = \frac{2\lambda_d}{c} = \frac{4\pi}{\omega_d} \quad (2.67)$$

with the detection frequency ω_d were observed for the coherent second harmonic (SH) emission from 360 to 440 nm . This is illustrated by the red tilted lines at a delay time of approximately 20 fs in figure 2.18a. For the incoherent emission from 450 to 520 nm , the interference fringes are detection wavelength independent, as indicated by the red vertical lines. The interference of the incoherent luminescence shows interference even with the random phase relation. This interference, however, is not based on the interference of the incoherent emission generated from the laser pulse pair. It is rather due to the constructive and destructive interference of the excitation pulse pair on the sample. The oscillating period depends on the fixed absorption frequency ω_a of the multi-photon induced excited state. For the photoluminescence, the coherence gets lost due to inelastic relaxation processes after absorption of the incident light. A representative spectrum measured from a pure ZnO wafer at a fixed time delay of approximately 100 fs is shown in figure 2.19. The spectrum shows the well-known interference fringes for the coherent emission on top of some incoherent background. The spectrum was Fourier-transformed to the frequency domain. This results in a signal at the frequency which corresponds to the time delay between the laser pulse pair (not shown here). This signal is filtered by a super

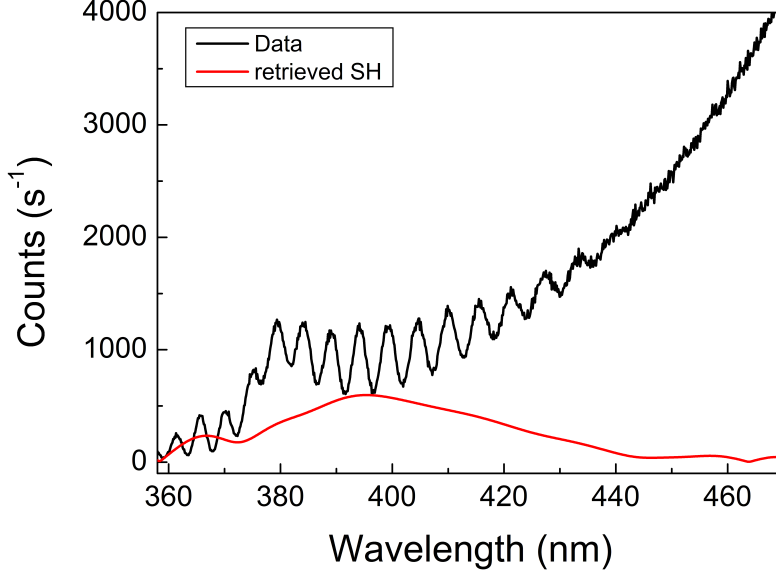


Figure 2.19: Emission spectrum (black) from ZnO. The extracted SH spectrum shown in red is retrieved by filtering in the Fourier-domain using a super Gaussian filter.

Gaussian function and transformed back by the inverse Fourier-transformation. This results in the background free coherent emission shown by the red line in figure 2.19. This easily allows the distinction between coherent and incoherent emission from samples. However, at zero time delay, a clear distinction between coherent and incoherent emission is not possible by using this technique. Therefore a clear retrieval of the electric field from the IFRAC trace, which is influenced by the incoherent emission, is rather challenging. Nevertheless, this technique is an essential tool within this thesis in order to concentrate on coherent emission from samples and on strongly localized photon modes in terms of Anderson localization.

In order to describe the experimentally deduced results theoretically, we used a model based on the optical Bloch equations, introduced in section 2.3.2, to solve the Liouville-von-Neumann equation for a four level system [70]. The incoherent emission is described by spontaneous relaxation from the excited state to the ground state. The coherent SH can directly be described by the induced polarisation assuming the dipole coupling to be nonlinear. Therefore equation 2.60 changes when a nonlinear two-photon excitation is taken into account:

$$H_1 = -\vec{d}_{kl}^{(2)} \cdot \vec{E}(t)^2 \quad \vec{d}_{kl}^{(2)} = \sum_m \frac{\langle \psi_k | q\vec{r} | \psi_m \rangle \langle \psi_m | q\vec{r} | \psi_l \rangle}{(\omega - \omega_{mk})(\omega - \omega_{ml})} \quad . \quad (2.68)$$

By the use of this retrieval approach, we were able to fully describe the experimentally emitted light and the recorded ZnO IFRAC trace.

Chapter 3

Spatiotemporal dynamics of localized photon modes in randomly arranged ZnO nano-needle arrays

The following chapter presents the main research conducted for this thesis. It is the experimental evidence of the spatial and temporal localization dynamics of light in strongly scattering dielectric media. The results were obtained with high-resolution optical microscopy in combination with time-resolved experiments using ultrashort laser pulses, which allow the direct microscopic and spectroscopic investigation of the localization. The experimental idea to localize photon modes within randomly arranged nanostructures is schematically illustrated in figure 3.1. An incident laser pulse (red beam) is multiply scattered within a non-absorbing random needle structure. The scattering is assumed to be elastic in order to conserve the coherence properties of the incident laser pulse, which allows the interference of different scattering paths. This leads to constructive interference of laser pulses from different scattering paths, which results in spatially highly confined electromagnetic fields, i.e localized photon modes. The electric field in these photon modes is much higher than in the surroundings. Therefore spatially confined strong electromagnetic fields are also called "hotspots". The electric field amplitude within a hotspot is sufficiently strong to generate second harmonic radiation at the nano-needles which can be used as a measure to determine the strength of the confined localized light mode at the fundamental frequency. Therefore the experimental set-up requires sufficient spatial resolution since the localization occurs on sub-wavelength scales, i.e. length scales in the order of a few hundred nanometers. The spatial confinement and the emission strength of the hotspot are the first hallmark of light localization.

The second hallmark is a modification of the temporal structure of the electric field within a localized photon mode. This is induced by multiple coherent scattering and the propagation of the fundamental light within the sample leading to an increased lifetime of the localized photon modes. Since multiple

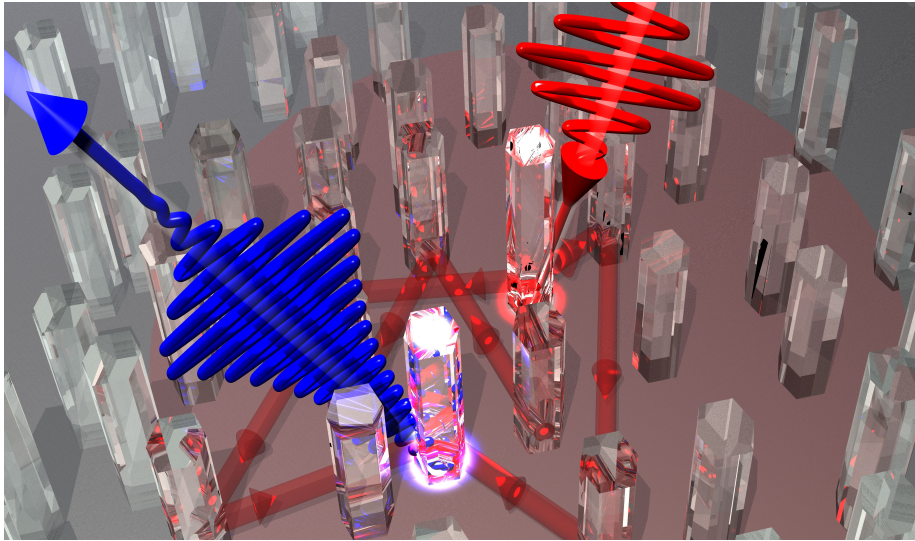


Figure 3.1: Schematic illustration of the experimental idea. The incident laser pulse (red beam) is multiply scattered within a random needle structure forming spatially confined high electromagnetic fields by constructive interference. The electric field is sufficiently strong to generate second harmonic radiation (blue beam) with an increased lifetime.

scattering occurs on length scales of a few hundred nanometers, the temporal measurements require ultra fast time resolution on timescales of a few femto-seconds.

In order to perform localization measurements, the sample has to fulfill several requirements such as strong coherent multiple scattering without too much absorption and sufficient second harmonic generation. Therefore, zinc oxide (ZnO) is an ideal candidate as will be confirmed in the following.

3.1 Zinc oxide: A candidate for the localization of photon modes

3.1.1 Zinc oxide properties

In this section the basic properties of zinc oxide (ZnO) will be discussed. ZnO has a wide range of different applications, ranging from medical applications or as an add-on in the chemical industry to physical applications like an efficient antireflection coating to enhance the performance of solar cells [74].

The energetically most favourable atomic structure of ZnO is the Wurtzite structure as schematically shown in figure 3.2a. Due to the non centro symmetric primitive cell with $b_1 = b_2 = 3.2\text{\AA}$ and $c = 5.2\text{\AA}$, ZnO is known to be piezo-electric [75]. The typical type of bond is covalent. ZnO binding in the crystal lattice involves four similar sp^3 hybrid orbitals in a tetrahedral geometry [76]. Four Zn^{2+} ions form a tetraeder within a O^{2-} ion in the center resulting in a hexagonal Bravais grid. The electric band structure results from the overlap

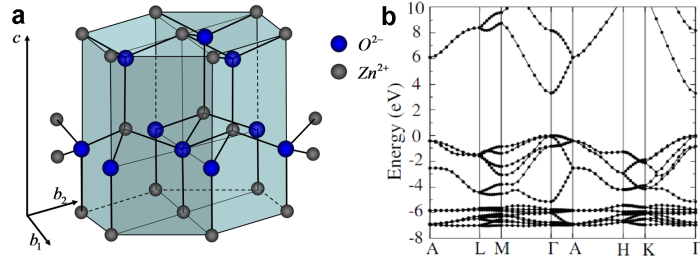


Figure 3.2: **a** The ZnO crystal in the Wurtzite structure based on covalent sp^3 hybrid orbitals. The primitive cell formed by the Zn^{2+} atoms (grey) and the O^{2-} (blue) is with non centro symmetric with $b_1 = b_2 = 3.2$ and $c = 5.2$. **b** Schematic illustration of the band structure of ZnO [77].

of the four sp^3 hybrid orbitals and is shown in figure 3.2b. The band formed by the bonding orbitals decrease in energy because of the favourable interaction between the parallel spin-paired electrons. The resulting band is called the valence band. In contrast, the energy band formed by the antibonding orbitals is called the conduction band, which is separated from the valence band by the band-gap [78]. ZnO is a II-VI semiconductor with a direct band gap of 3.37eV [79]. Due to this high band gap, ZnO absorbs light in the UV region as shown in the measured transmission spectrum $T(\lambda)$ in figure 3.3. The absolute transmission is therefore characterized for a 1 mm thick ZnO crystal. For excitation in the

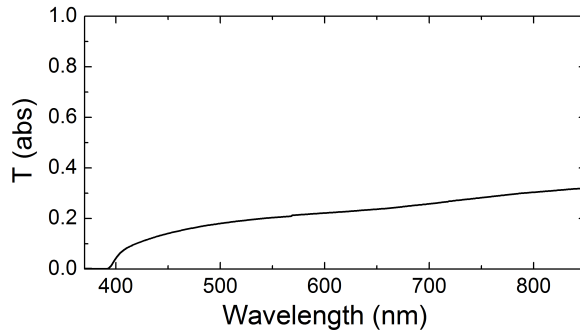


Figure 3.3: Absolute transmission through a 1 mm thick ZnO crystal.

red and near-IR spectral region, ZnO is nearly transparent. These properties make ZnO a promising material for opto-electronic applications [79]. Even at room temperature the large exciton binding energy of approximately 60meV allows efficient emission from exciton states [80]. Due to the influence of the crystal field and the spin-orbit interaction of the 2p-level of oxygen at the Γ point of the Brillouin zone, the valence band splits up into 3 different bands [81]. These 3 levels are named A,B and C. They are only separated by 5 meV. Optical excitation in the A and B band is only possible for a polarization perpendicular to the polar hexagonal axis c . For optical excitation of the C band,

the polarisation has to be along the polar hexagonal axis c .

In addition ZnO has a high refractive index of almost $n \approx 2$ at 800nm wavelength as shown in figure 3.4. Therefore the scattering of light, which results in a change of the propagation trajectory, is strong in ZnO. Furthermore, the second

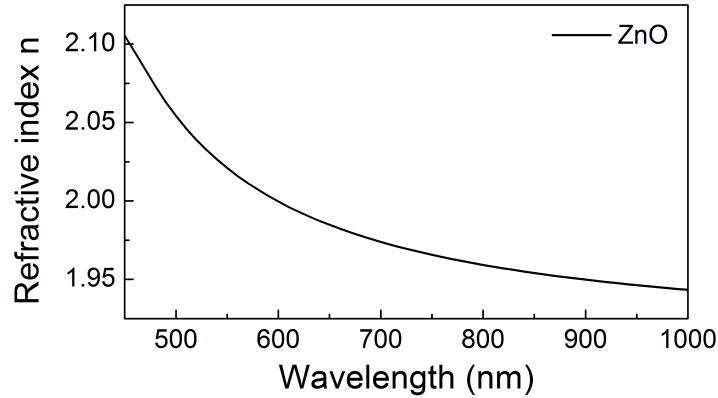


Figure 3.4: Refractive index for ZnO as a function of the wavelength [83].

harmonic efficiency, described by second-order susceptibilities $\chi^{(2)}$, is strong for ZnO [120, 79]. Even a larger effective second order nonlinearity was demonstrated for thin films of ZnO compared to that of a BBO-crystal measured by a 20 fs excitation pulse from a Ti:Sapphire oscillator with an almost negligible group velocity dispersion [84]. The absolute value of $\chi^{(2)}$ differs strongly and depends on the ZnO surface structure and crystal orientation [85]. The angularly resolved SHG signal shows a pronounced dependence on the incidence laser pulses. However, in thin films bulk effects dominate surface effects for the second-harmonic generation. The strong scattering and the efficient SH generation response makes ZnO an interesting applicant for localization measurements using a two-photon microscope.

3.1.2 ZnO nano-needles produced by metal-organic vapour phase epitaxy (MOVPE)

Within this work the spatiotemporal dynamics of light localization will be investigated. This requires a highly scattering, non absorbing pointlike scatterer. Due to the mentioned properties, randomly arranged ZnO needles with diameters in the sub μm range are chosen. The samples of randomly arranged ZnO nano-needles are grown on a sapphire (0001) substrate by our cooperation partners at the University of Tokio by using Metal-Organic Vapour Phase Epitaxy (MOVPE) [86].

ZnO crystallises mainly in two different forms: hexagonal cubic zincblende and hexagonal wurtzite structure. To receive the zincblende structure, ZnO is grown on substrates with a cubic lattice structure. However, the most stable and common structure is the wurtzite structure. To obtain this the ZnO assembles itself to hexagonal mono-crystalline rod structures on a substrate, e.g. sapphire, growing along the c -axis as illustrated in figure 3.2. The ZnO nano-needles

are produced by using diethyl zinc (DEZn) and oxygen as reactant gas. In addition, argon is used as a carrier gas in the catalyst-free MOVPE system. The diameter of the ZnO structures depends on the used temperature. By using a two-temperature growth technique two different diameters of the needles are obtained [86]. The growth technique is schematically illustrated in figure 3.5a. In the first step, 450°C is kept constant for 35 min. This results in approximately 100nm thick and $1\mu\text{m}$ long hexagonal needles, which are characterized by SEM and shown in figure 3.5b. In a second growth step, the temperature is raised

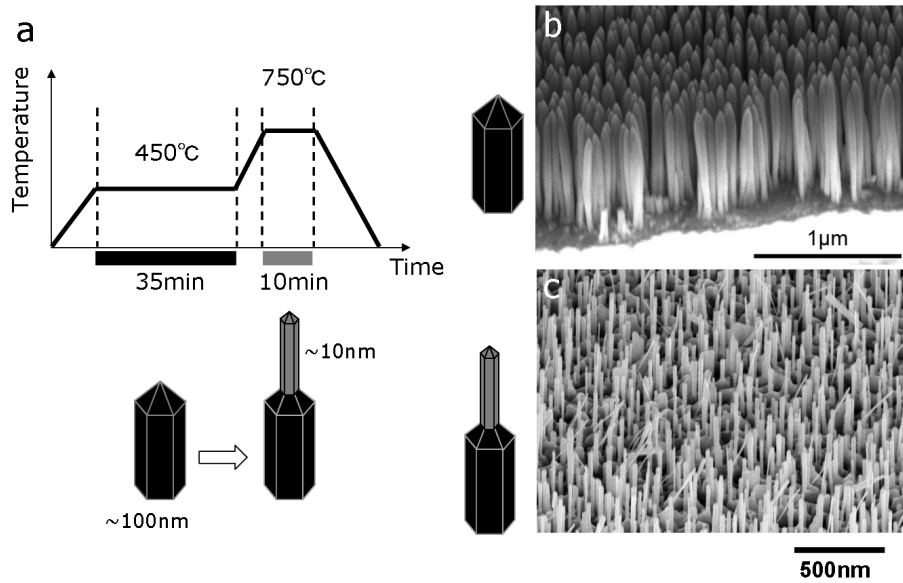


Figure 3.5: **a** Schematic illustration of the two-temperature growth method resulting in a approximately 100 nm thick needles at the bottom and 10 nm thick needles on top. The thick needles **b** and the small needles **c** are characterized by scanning electron microscopy.[86]

up to 750°C for 10 min. The needles are again characterized using SEM and are shown in figure 3.5c. The SEM image shows approximately $30 - 50\text{ nm}$ thin ZnO needles in diameter on top of most of the thick needles. Therefore, the higher temperature reduces the needle diameter.

Both samples, the ZnO sample with 100nm thick needles as well as the samples with additional thin needles on top, are almost transparent for the visible spectrum. Within this spectral range the ZnO leads to sufficiently strong coherent scattering of light without getting absorbed within a needle. The needle diameter is more than one order of magnitude smaller than the wavelength of the light in the visible region of the spectrum. Therefore, they can be seen as individual structureless pointlike scatterers. In conclusion, the ZnO nano-needles fulfill all the sample requirements needed to analyse the spatiotemporal dynamics of light localization.

3.2 Spatial localization of light

3.2.1 Experimental set-up

The spatiotemporal dynamics of localized photon modes can experimentally be verified by measuring both hallmarks of localization: spatially confined electric fields, i.e. hotspots, and an increased lifetime of the localized photon mode. Within the first experimental part, the spatial confinement of the localized photon mode is investigated, which is the first hallmark. To achieve this a highly suitable method was chosen, which is based on using the ultrafast second harmonic (SH) microscope. The SH microscope has an enhanced spatial resolution compared to a classical microscope due to the detection of the nonlinear second harmonic emission. Furthermore, the nonlinearity allows an increased sensitivity to changes in the local electric field.

The set-up to verify the spatial localization is shown schematically in figure 3.6a. Here, 6 fs p-polarized laser pulses from a Ti:Sapphire oscillator operating at an 82 MHz repetition rate at 870nm central wavelength with pulse energies of up to 2.5 nJ are used. The positive dispersion of the pulses induced on the experiment during the propagation is compensated by a pair of chirped mirrors (Femtolasers GSM014) and fine-tuned by a pair of wedges (Femtolaser UA124). This conserves the time structure of the laser pulse to 6 fs. The light intensity acting on the sample is controlled by a continuous neutral density filter. The laser beam diameter is enlarged by a pair of concave mirrors by a factor of 3 from 1 mm to 3 mm which slightly overfills the entrance aperture of the all-reflecting objective (Davin Optronics 5004-000) with a numerical aperture of $NA = 0.5$. By using an all-reflective objective, the laser beam can be focused down to the diffraction limit of about 1 μm . Simultaneously, the temporal structure of the ultrashort laser pulse within the focal plane is preserved. Within a classical microscope objective, a femtosecond laser pulse gets broadened up to several picoseconds [87].

The spatial beam profile of the diffraction limited laser pulses in the focal plane is shown in figure 3.6b. The image of the focus is achieved by raster scanning an aluminium coated scanning near-field fibre tip through the focal plane of the 6 fs laser pulses. The aperture of the tip is approximately 200 nm which allows a high spatial resolution. The light coupled into the fibre is detected by a photomultiplier as a function of the position within the focal plane. The spatial intensity distribution shows a nearly circular focus spot and additionally clearly visible Airy rings. The Airy rings are diffraction patterns due to the limited wave vector spectrum $I(k_{lat})$ of the all-reflecting objective [87]. The construction of the all-reflecting objective with a small inner mirror and a large focusing mirror does not allow central lateral wave vectors k_{lat} as illustrated in figure 3.7. This results in Airy rings.

The full width at half maximum of the experimentally deduced intensity distribution in the focal plane is estimated at $x_r \approx 1\mu m$ which is in good agreement with the theoretical value calculated by

$$x_r(\lambda, NA) = \frac{0.61 \cdot \lambda}{NA} \approx 1\mu m \quad (3.1)$$

for an objective with a numerical aperture of $NA = 0.5$ and a wavelength of $\lambda = 870 nm$.

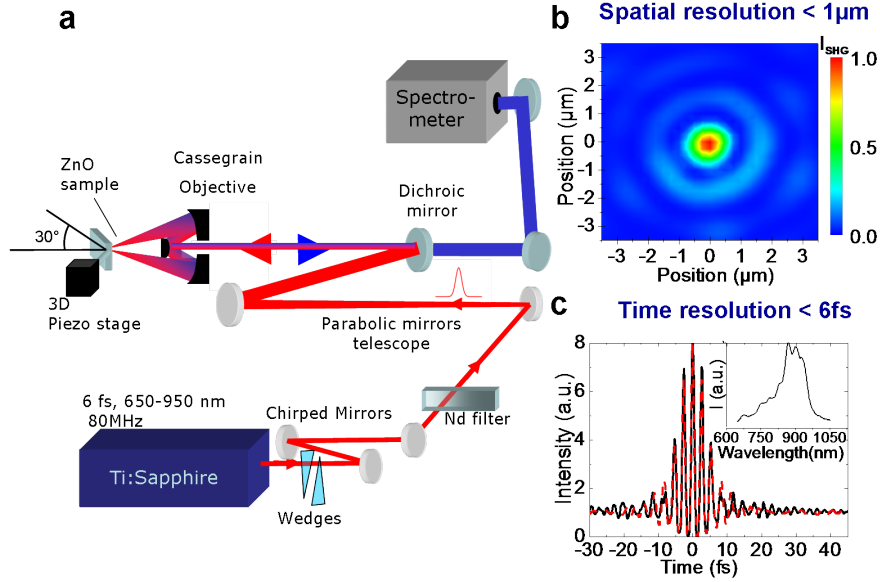


Figure 3.6: **a** Experimental set-up: An ultrashort, dispersion-controlled 6 fs laser pulse is focused by an all-reflecting objective on the sample. The light emitted from the sample is detected in reflection geometry as a function of position by raster-scanning the sample and separated from the incident light by a dichroic mirror. The emission is spectrally resolved using a monochromator in combination with a CCD camera. **b** Spatial intensity map of the focal plane deduced by raster-scanning an aluminium-coated scanning near-field fibre tip through the focus. The Ti:Sapphire laser is focused on the diffraction limit allowing a spatial resolution of less than $1\mu\text{m}$. **c** Interferometric autocorrelation (IAC) trace taken in the reflecting objective showing the preserved time structure of the 6 fs laser pulse. The measured IAC (black line) trace is compared to a calculated transform-limited IAC (red line) deduced from the spectrum shown in the inset.

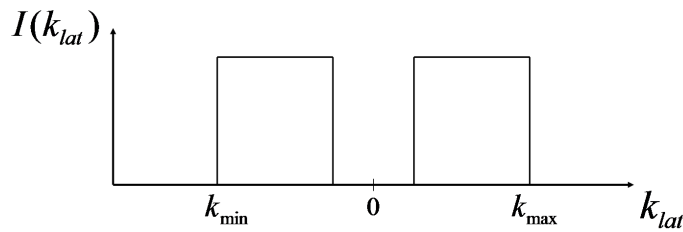


Figure 3.7: Wave vector spectrum k_{lat} of the Cassegrain objective. The central wave vector components are cut out by the small inner mirror of the objective.

In addition to the verification of the spatial resolution of the SH microscope, also the temporal resolution is verified. This is proven by an interferometric autocorrelation (IAC) measurement using a $10\mu\text{m}$ thick BBO crystal. IAC measurements are a common technique to characterize ultrashort laser pulses using a pulse pair separated by the time delay τ [88]. The IAC is described by

$$I_{IAC}(\tau) = \left| \int (E(t) + E(t + \tau))^2 dt \right|^2 \quad (3.2)$$

with the electric field $E(t)$. The experimentally deduced IAC is shown in figure 3.6c in black. It is compared to a theoretical IAC (red), that is calculated from the laser spectrum shown in the inset of figure 3.6c. Therefore the Fourier-limited laser pulse is calculated from the spectrum. By using additional dispersion the theoretical IAC trace matches the measured trace. This results in a time duration of the intensity of the electric field of 6 fs (FWHM) within the focal plane. Therefore the all-reflective objective preserves the temporal structure of the focused 6 fs laser pulses emitted from the Ti:Sapphire oscillator.

In conclusion, the SH-microscope provides 6 fs laser pulses at a central wavelength of 870 nm focused on an area of $1\mu\text{m}$ in diameter to investigate the spatial emission from samples. The light emitted from the sample is collected by the all-reflecting objective in reflection geometry. Light below 550 nm is separated from the fundamental incoming laser beam by a dichroic mirror (Thorlabs UV Cold mirror FM204) and spectrally dispersed in a monochromator (Acton Spectra Pro 2500i with a 300lines/500Blaze grid). The spectrum is finally detected by a liquid- N_2 cooled CCD camera (Princeton Instruments Spec-10). Additionally, BG23 filters (BG23 Schott) are used to avoid scattered fundamental light and to restrict the detection only on wavelength components below 500 nm .

The ZnO samples are mounted on a hardware-linearized three-axis piezo scanner (PI NanoCube) at an oblique angle of 30° with respect to the incident horizontally polarized laser pulses. The used piezo scanner allows to raster scan the sample through the focused laser spot with a position accuracy of less than 10 nm . The tilt of the sample with respect to the incident light allows the highest electric field components along the ZnO needle axis with the p-polarized incident laser pulses without blocking the high wave vector components k_{lat} and destroying the diffraction limited focus spot. Due to the tilt of the sample, the needles are mainly affected by p-polarized light. However, due to the rotation symmetry and the angular projection, they are also affected by a small amount of s-polarized light.

Several samples are examined using this experimental method. The investigated samples shown in this thesis consist of **a** 100 nm thick and **b** $30 - 50\text{ nm}$ thin randomly arranged ZnO nano-needle arrays. Both needle diameters are chosen to be smaller compared to the incident wavelength in order to be in the regime of coherent Rayleigh scattering. Both samples were produced from our cooperation partners Takashi Yatsui and Kokoro Kitamura in the group of Prof. Ohtsu from the University of Tokyo [86]. The characteristics for these two samples and the experimental results concerning the spatial localization of light are presented in the following.

3.2.2 Spatial localization in 100 nm thick ZnO nano-needles

In a first experimental investigation, the 100 nm thick ZnO nano-needles were examined in terms of the spatial localization of photon modes. The sample has been produced using only one growth step in the MOVPE at a temperature of 450°C for 35 min as illustrated in figure 3.5. The surface structure is characterized using scanning electron microscopy (SEM) imaging. The SEM image of the sample is shown in figure 3.8a. It shows a rough surface structure of vary-

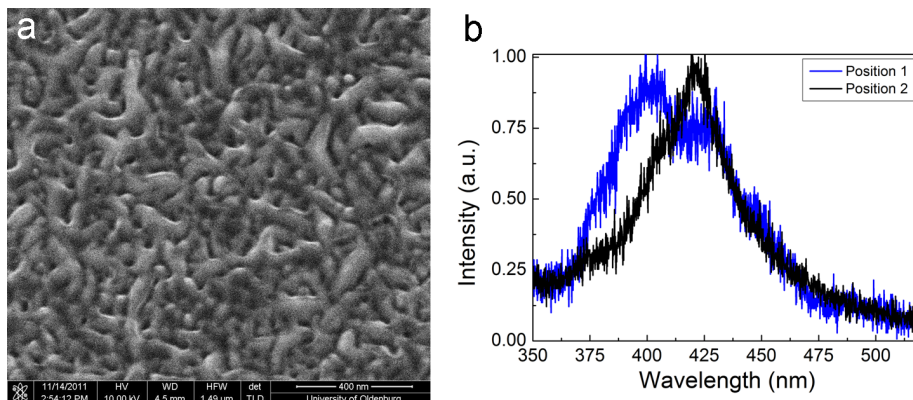


Figure 3.8: **a** SEM image of the investigated 100 nm thick ZnO nano-needles. Top view of the sample shows randomly distributed cones of ZnO together with needles in the range of 80 to 120 nm. **b** Spectral emission from the 100 nm thick ZnO nano-needles. The two spectra shown consist mainly of SH emission but show different localized modes. The band gap emission known to occur in ZnO at 375 nm and green luminescence above 450 nm are weak.

ing, randomly distributed larger ZnO cones and smaller needles with diameters between 80 nm and 120 nm. The average diameter of the needles is estimated to be approximately 100 nm. Therefore, in the following the sample is referred as the 100 nm thick ZnO nano-needle array.

The spatial localization of photon modes is investigated by the use of the SH-microscope set-up introduced in figure 3.6. Therefore the sample is excited with a pulse energy of 50 pJ. The light emitted at the SH frequency from the sample is spectrally resolved as a function of the excitation position. Typical normalized spectra of the emitted SH from two different spatial positions on the 100 nm thick ZnO nano-needle array are shown in figure 3.8b.

The light emitted from the two different positions clearly shows different spectral components. It mainly consists of coherent SH emission checked by interferometric frequency resolved autocorrelation which is not shown here. Furthermore, spectral identification of the band gap transition at approximately 375 nm (3.3 eV) and the green photoluminescence above 450 nm only indicate a very weak emission intensity of these incoherent emission processes. However, the shape of the two emitted coherent SH-spectra clearly differ from each other due to photon modes at the two positions.

Spectral integration of the recorded emission from 380 to 440 nm results in the SH intensity I_{SH} . By raster scanning the sample through the focus and spectrally integrating the SH emission, a two-dimensional map of the local I_{SH}

is obtained which is shown in figure 3.9a. The emitted SH intensity shows moderate fluctuations as a function of the spatial position. These moderate fluctuations are far away from the fluctuations occurring at hotspots as known from literature [64, 27]. In order to classify the fluctuating emission from the sample, several methods can be applied.

One method is based on the enhancement of the SH emission which is defined as $\eta = I_{SH_{max}}/I_{SH_{min}}$. This results in the case of the 100 nm thick ZnO nano-needle with an enhancement factor of $\eta \approx 6$. The SH emitted from the sample is only used as an indirect measure for the fundamental electric field strength. The interesting parameter within all the measurements is the local electric field at the fundamental wavelength. The fluctuations at the SH intensity allow to calculate the fundamental local field enhancement factor f . The general nonlinear response

$$I_b \propto \left(\frac{E_{loc}}{E_0} \right)^{2b} = f^{2b} \quad \Rightarrow \quad f = (\eta)^{1/2b} \quad (3.3)$$

scales with the nonlinearity b and is defined by the relation of the local electromagnetic field maximum at the fundamental wavelength E_{loc} and the minimum electric field at the fundamental frequency E_0 [94]. In the case of the SH, $I_b = I_{SH}$ the nonlinearity is given by $b_{SH} = 2$. Therefore, the nonlinear behaviour of the SH intensity scales with the fourth power of the local electromagnetic field at the fundamental wavelength. Analysing the spatial SH intensity distribution, the local field enhancement of the 100 nm thick ZnO needles can be estimated by using equation 3.3 with $f_{100nm} \approx 1.5$, which is quite a low value.

Another concept is based on the normalized fluctuations of the SH intensity. This will be referred to in the following as normalized enhancement and is defined by

$$\kappa = I_{SH_{max}} / \langle I_{SH} \rangle \quad (3.4)$$

with respect to the average SH intensity $\langle I_{SH} \rangle$. In the case of the 100 nm thick ZnO nano-needles, this results in $\kappa_{100nm} = 2.4$. The normalized enhancement κ will be used in the following section 3.2.5 to deduce the localization strength.

Not only strong fluctuations of the intensity are a characteristic for a hotspot, but also the spatially confined emission as a second criterion. Analysing the cross section of I_{SH} in figure 3.9b shows that the SH emission is extended over approximately 3.5 μm (FWHM). This value is much larger than the optical resolution of the SH-microscope of $x_r(\lambda = 400 nm, NA = 0.5) \approx 500 nm$ calculated by equation 3.1. An additional way to visualize this spatial extent of the SH emission can be achieved by calculating the spatial correlation

$$C_s(\Delta x, \Delta y) = \frac{\sum I_{SH}(x, y) \cdot I_{SH}(x + \Delta x, y + \Delta y)}{\sqrt{\sum I_{SH}(x, y)^2} \sqrt{\sum I_{SH}(x + \Delta x, y + \Delta y)^2}} \quad (3.5)$$

with a shift along the x-, y-axis described by Δx and Δy , respectively. The spatial correlation is generally used to deduce the typical width, which corresponds to the average size of a speckle pattern on a surface [89], near-field images in disordered dielectric structures [90] or quantum dots [91]. In order to calculate the spatial correlation for the SH intensity distribution of the 100 nm thick

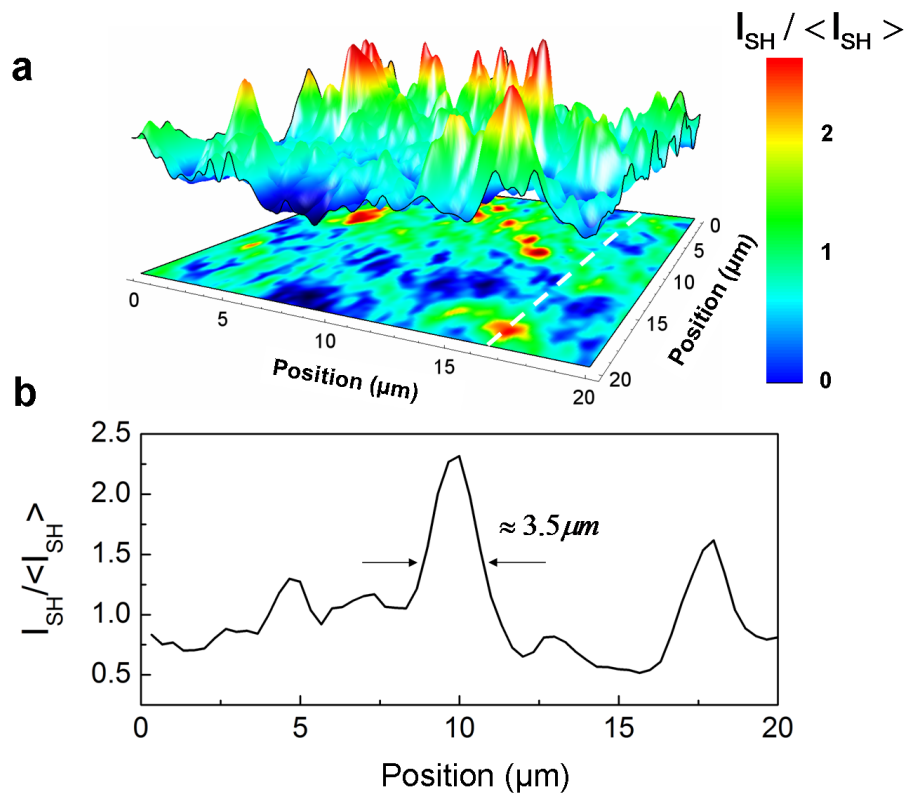


Figure 3.9: **a** Spatial emission map of the local SH emission I_{SH} (integrated from 380 to 440 nm) from the 100 nm thick ZnO nano-needle array. The sample is excited by 6 fs laser pulses with a central wavelength of 870 nm . **b** Cross section along the dashed line in **a**. The spatial spread of the emission spots is much larger than the optical resolution of the SH-microscope.

ZnO needles by using equation 3.5, a two dimensional zero-padding is applied to the spatial SH intensity map. The resulting two-dimensional correlation as a function of the shift along the x and y-axis of the SH emission map is presented in figure 3.10a for the 100 nm thick ZnO nano-needle array. The cross section for a shift along the x-axis $C_s(\Delta x, 0)$, as well as the y-axis $C_s(0, \Delta y)$ is shown in figure 3.10b. The spatial autocorrelation function C_S shows a broad background in the absence of the characteristic spatial autocorrelation spike, as expected for a hotspot. This broad background stems either from the spatial resolution of the SH microscope or the spatial region of the emission. However, the resolution of the SH microscope is in the order of 500 nm, as proven in section 3.2.1. A characteristic value of the spatial autocorrelation is the spread at FWHM ΔC_S . The correlation shows a wide spread of $\Delta C_S \approx 28 \mu m$, which is much larger than twice the resolution of the microscope. Therefore the results are associated with the spatial extent of the photon modes. From these autocorrelation plots it appears, that mode localization due to multiple scattering is weak and the emission from the sample stems mainly from spatially delocalized photon modes.

In conclusion, the investigated sample shows only marginal fluctuations of the local SH intensity from delocalized photon modes with a spatial extent over several μm . The localization strength is determined in detail in section 3.2.5.

3.2.3 Spatial localization in 30 nm thin ZnO nano-needles

The small amount of localization within the investigated 100 nm thick ZnO nano-needle array suggests using samples with changed parameters to increase the localization of light. Therefore, the sample was modified by using a second temperature during the MOVPE production process by our cooperation partners from the University of Tokio [86]. The used two-temperature MOVPE was already introduced in section 3.1.2. The SEM-image of the sample is shown in figure 3.11 to deduce the geometric sample properties. The bottom layer produced by the first heating process leads again to an ensemble of larger ZnO cones and needles with diameters of approximately 100 nm. It is in good agreement with the structure shown in figure 3.8. The thin needles produced by an increased temperature have diameters varying between 20 – 50 nm mainly grown on most of the thick needles. The average diameter is determined to be approximately 30 nm. Therefore, the sample is referred to in the following as the 30 nm thin ZnO nano-needle array. Furthermore, the needles are homogeneously distributed, for which most of the 30 nm sample do not show any big deviations. The homogeneous distribution allows to deduce that the average density of the needles from the SEM-image shown in figure 3.11a is approximately 60 needles μm^{-2} .

The investigation of the localization properties is performed by placing the sample of thin ZnO nano-needles in the experimental set-up and measuring the light emitted from the sample as a function of the excitation position, as shown in figure 3.6. To achieve this the sample is excited with a pulse energy of 50 pJ. The spectral integrated SH emission map $I_{SH}(x, y)$ is shown in figure 3.12a. The local emitted SH intensity shows numerous occurring regions of strong fluctuations. These fluctuations are characterized by the enhancement η reaching more than a factor of $\eta_{30nm} = I_{SHmax}/I_{SHmin} \approx 80$, comparing the

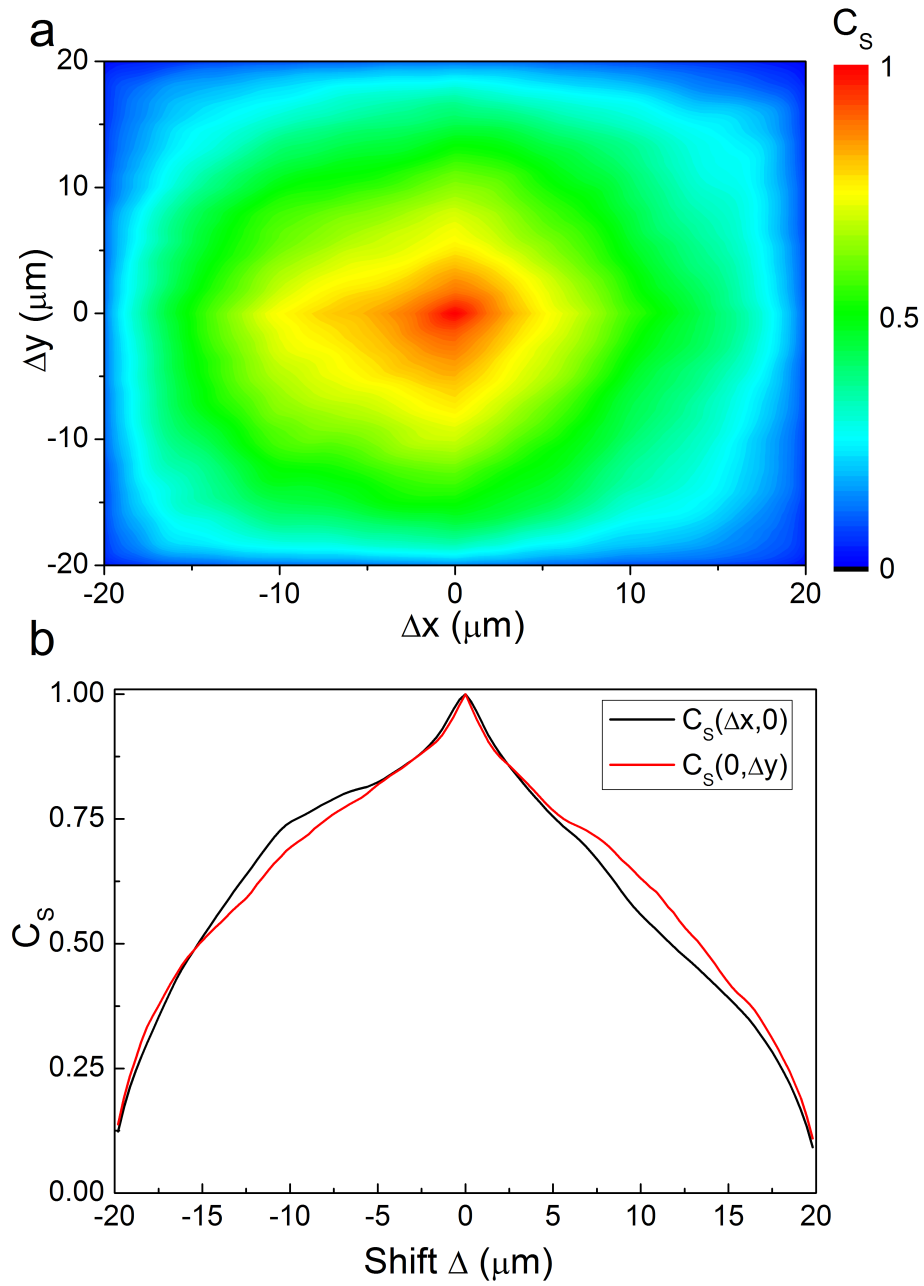


Figure 3.10: **a** Two-dimensional spatial intensity correlation of the SH emission map of the thick ZnO nano-needle array. **b** Cross section of the spatial intensity correlation along the x- and y-axis.

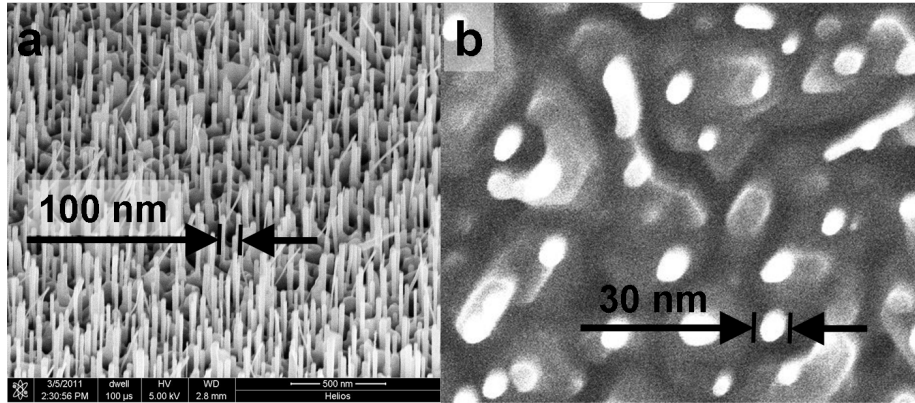


Figure 3.11: SEM pictures of the investigated ZnO 2step sample. **a** Side view at an oblique angle of 52° shows randomly arranged ZnO nano-needles homogeneously distributed over the sample. The average distance between the needles is approximately 100 nm . **b** Top view of the needle array shows needle diameters between $20\text{ to }50\text{ nm}$ with an average diameter of approximately 30 nm .

maximum $I_{SH_{max}}$ to the minimum SH intensity $I_{SH_{min}}$. The fluctuations of the SH allow to calculate the fundamental local field enhancement factor f using equation 3.3 and taking the nonlinearity of the SH $b_{SH} = 2$ into account. This results in a local field enhancement for the 30 nm thin ZnO nano-needle array of $f_{30nm} \approx 3$. The field enhancement of the tips enhances not only the local electromagnetic field at the fundamental frequency, but also the SH emission is increased [92, 93, 94].

In order to classify the fluctuation strength and to compare the results, the mean enhancement $\kappa = I_{SH_{max}} / \langle I_{SH} \rangle$ is used. For the 30 nm thin ZnO nano-needle array on top of the underlying layer of 100 nm thick needles, this results in $\kappa_{30nm} \approx 33$. This value, as well as the local field enhancement f , is obviously much larger compared to the 100 nm thick ZnO nano-needle array with $f_{100nm} \approx 1.5$ and $\kappa_{100nm} = 2.4$ from the previous measurement in section 3.2.2.

The spatial extent of the SH hotspots is inspected by the cross section of I_{SH} along the white dashed line in figure 3.12a. This cross section through one of the strongly emitting SH regions is shown in 3.12b. Here the SH emission is confined to an area of approximately $x \approx 500\text{ nm}$ in diameter. This diameter corresponds to the optical resolution of the SH-microscope at the detection wavelength of $\lambda_d = 400\text{ nm}$ calculated from equation 3.1. The strong enhancement of the local SH intensity in combination with the spatially confined emission fulfill the criterion of a hotspot and a localized photon mode in terms of the first hallmark of light localization.

The high optical resolution of the SH microscope is sufficient to mainly probe a single localized mode within the spatial measurements. This claim will be supported by measurements as well as theoretical work in the following sections and chapters.

One obvious result of the spectrally resolved two-dimensional intensity mea-

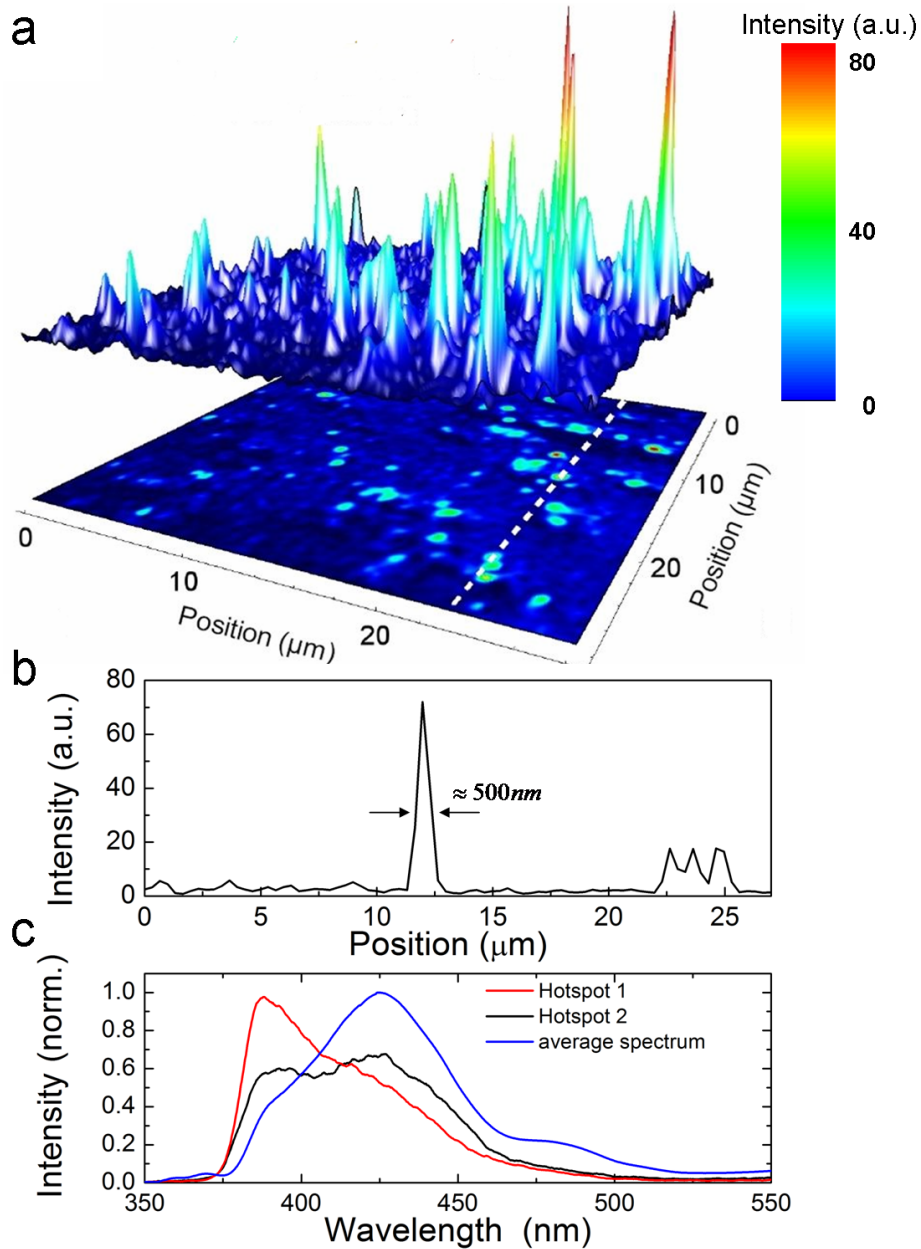


Figure 3.12: **a** Spatial emission map of the spectral integrated local SH from the thin ZnO nano-needle array. The array is excited by 6 fs laser pulses at a central wavelength of 870nm . **b** Cross section along the dashed line in **a**. The hotspots have a diameter of $x \approx 500\text{nm}$. This corresponds to the optical resolution of the SH microscope. **c** Local SH spectra from different hotspots (red and black) and the normalized spectrum averaged over the whole sample (blue).

surement is the strong spectral dependence on the spatial position. The spectrum of different hotspots is presented in figure 3.12c. It clearly shows somehow individual spectral shapes at different hotspots. This is supported by a more detailed spectral analysis of the strongest hotspot and its surrounding presented in figure 3.13. The emission within the hotspot position is dramatically stronger and almost confined to one pixel within the scan. This very confined, highly enhanced emission in combination with the high spatial resolution allows to observe spectral changes of the emitted light on the sub μm scale. The emission at each spatial position delivers different spectral components. The spectrum shifts from one localized photon mode at the hotspot position in figure 3.13b.e to another in figure 3.13b.i. This behaviour is caused by the random distribution of the nano-needles. The incident light at the fundamental frequency is scattered at each needle. This leads to a large number of scattering trajectories as explained in section 2.2.4.

At a certain position in space, the elastically scattered light interferes constructively at individual resonance frequencies depending on the scattering trajectory forming locally very confined hotspots with varying spectral components. These localized photon modes at the fundamental frequency are sufficiently strong to excite the SH at the ZnO interface of the nano-needles. This results in a broad range of observed spectral shapes at different sample positions. These strong variations of the local emitted SH spectra correspond to different localized photon modes and are also a strong indicator of photon localization [11].

The excitation below the band gap with sufficient laser pulse energies mainly leads to SH emission. However, multi-photon induced luminescence from the band gap or defect states in the ZnO can be observed as well, checked by interferometric frequency resolved autocorrelation and further explained in section 3.3.

The spatial confinement of the localized photon modes within the 30 nm thin ZnO nano-needle array can additionally be visualized by calculating the spatial correlation of the two-dimensional SH intensity distribution using equation 3.5. Therefore two dimensional zero-padding is applied to the spatial SH intensity map. The resulting two-dimensional correlation distribution $C_S(\Delta x, \Delta y)$ as a function of the shift along the x- and y-axis of emission map I_{SH} of the 30 nm thin ZnO nano-needles is presented in figure 3.14a. The cross section along the x-axis $C_S(\Delta x, 0)$, and the y-axis $C_S(0, \Delta y)$ is shown in figure 3.14b.

The spatial autocorrelation function C_S shows the characteristic sharp spatial autocorrelation spike, as expected for the emission from hotspots. The characteristic value of the spatial autocorrelation is $\Delta C_S \approx 1.6 \mu m$, which is slightly more than twice the spatial resolution of our microscope. This behaviour indicates, that not all emission spots on the sample are confined to the optical resolution of the microscope. From these autocorrelation plots it appears that mode localization due to multiple scattering is strong and the hotspot emission from the sample stems mainly from spatially localized photon modes which are essentially determined by the spatial resolution of the SH microscope.

In conclusion, the investigated sample of 30 nm thin randomly arranged dielectric ZnO nano-needles shows strong fluctuations of the local SH intensity from localized photon modes. This is the first hallmark for the localization of light.

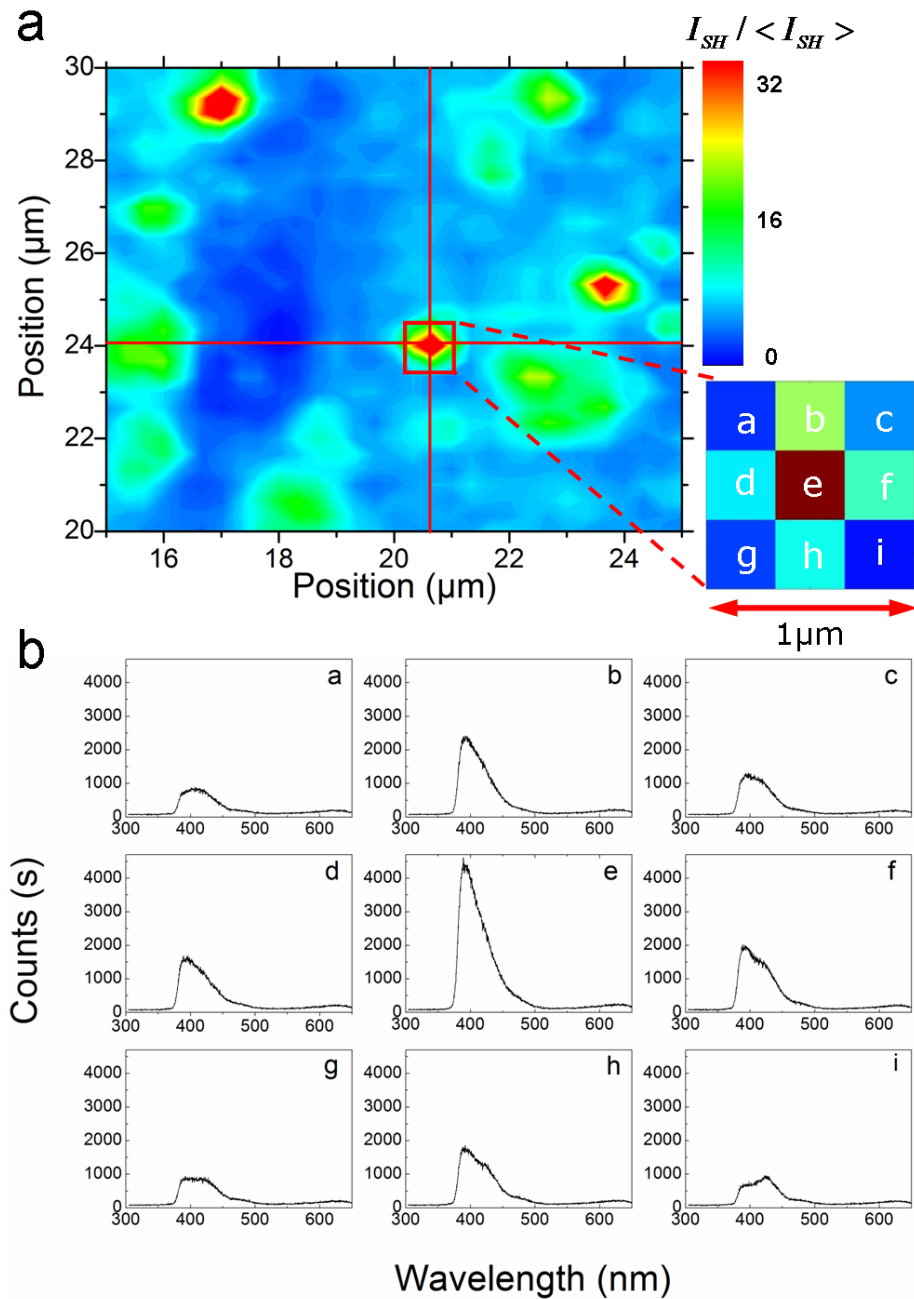


Figure 3.13: **a** Two-dimensional intensity distribution of the SH normalized to the mean intensity emitted from the thin ZnO nano-needle array. **b.a-i** Recorded spectra of the indicated area (red square) of the integrated SH image. The spectral shape and the emitted SH intensity depends strongly on the spatial position on a sub- μm scale.

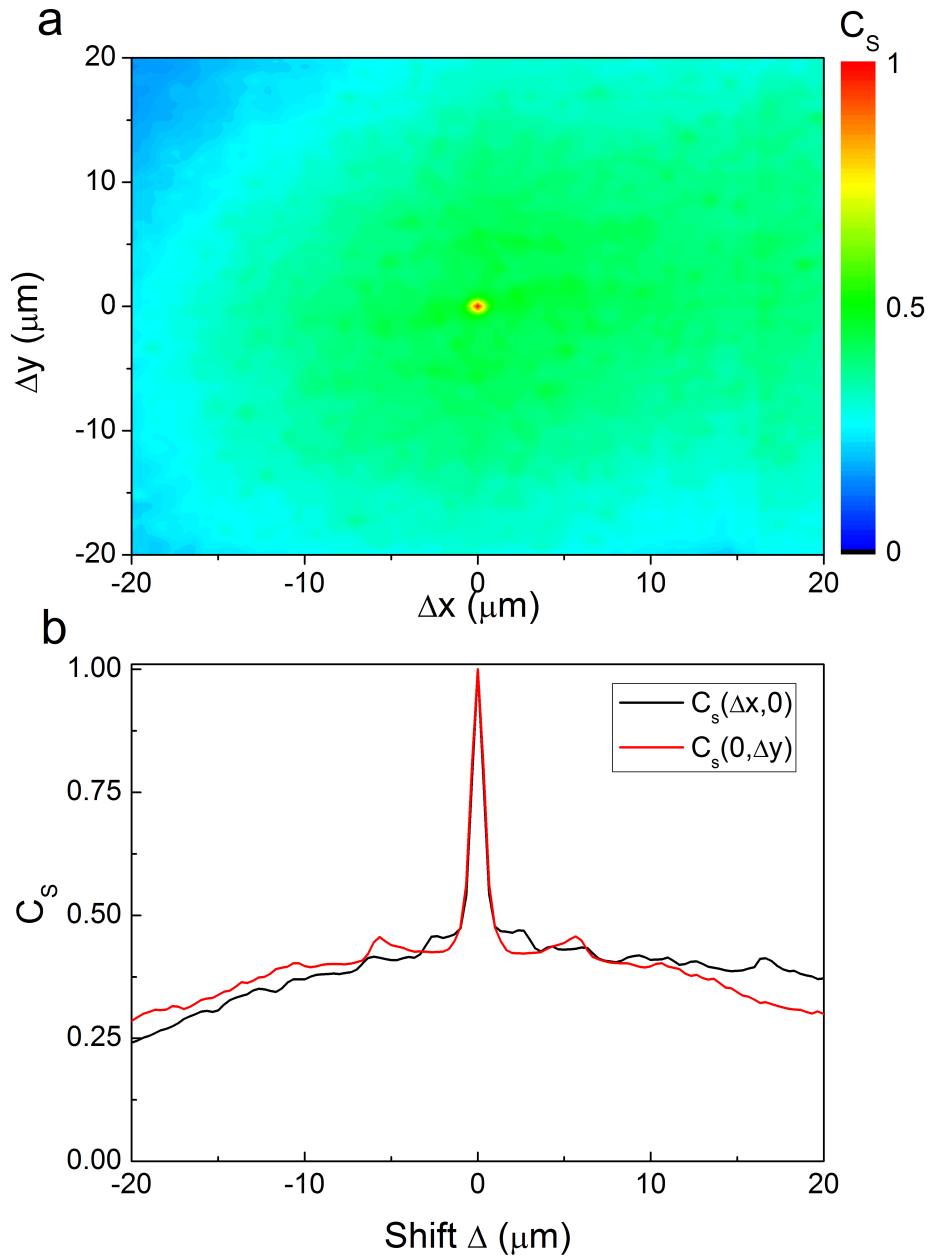


Figure 3.14: **a** Two-dimensional spatial intensity correlation of the SH emission map of the thin ZnO nano-needle array. **b** Cross section of the spatial intensity correlation along the x- and y-axis.

Localization strength is classified by using spatial intensity fluctuations and discussed in detail in section 3.2.5. The influence of random lasing, induced in disordered nano-structures or powders forming a random laser cavity [14], is ruled out by the low applied incident laser power. The applied laser power is well below the threshold of random lasing as will be shown in chapter 6.

3.2.4 FDTD calculation

In addition to the measurements, a three dimensional Finite Difference Time Domain (FDTD) simulation has been performed by David Leipold within a collaboration with the TU Ilmenau and the group of Prof. Runge. The simulations were performed by using the MIT Electromagnetic Equation Propagation (MEEP) software suite [95]. This is a method to solve time dependent differential equations, by which the time-dependent Maxwell's equations are solved for a simulated randomly arranged array of ZnO nano-needles with parameters comparable to the experimentally investigated samples.

The geometric parameters of the needle distribution are deduced from the SEM images of the investigated sample. The ZnO nano-needles are simulated by randomly distributed cylinders on a sapphire substrate in vacuum. In order to consider the geometric and material properties, the sample is modeled by a spatial dependent three-dimensional refractive index distribution $n(\vec{r})$ at the fundamental wavelength by assuming that $n(\text{ZnO}) = 1.96$ and $n(\text{Sapphire}) = 1.75$ are assumed. A section of the used spatial distribution of $n(\vec{r})$ is shown in figure 3.15a from a top view (left) and side view (right).

It shows a cylinder density of approximately 60 cylinders per μm^2 . The cylinders have diameters of 100 nm with a randomly varied length between $0.9 - 1.0\ \mu\text{m}$ to avoid backscattered light from the flat cylinder caps. The excitation source is assumed to be a plane wave illuminating the whole sample at once with a laser pulse at an incident angle of 30° with respect to the sample surface. The laser pulse is set to a Gaussian temporal envelope of 6 fs (FWHM) at 800 nm central wavelength. Due to a limited amount of computing capacity, the electric field $E(\vec{r}, t)$ is calculated with a spatial resolution of 10 nm on a $4.5 \times 4.5 \times 2\ \mu\text{m}$ grid which corresponds only to a small section compared to the measurement. In this case, the time-dependent Maxwell's equations are solved by calculating the electric field in the simulation area at a given instant in time to continue with the magnetic field in the same simulation area at the next instant of time. This procedure is repeated until the temporal evolution of the electromagnetic field is fully developed for the simulation area. To obtain the localization behaviour of the local electromagnetic field, the electromagnetic field of the excitation laser pulse has to leave the calculation area to deduce the localized electric field modes, which are small compared to the electric field of the excitation. To compare the calculated intensity maps at the fundamental wavelength to the experimental data, the relation for the local SH intensity $I_{SH}(\vec{r}, t) \propto |E(r, t)|^2$ is used. The resulting spatial distribution of $E(\vec{r})^4$ is shown at time t , after the excitation pulse has left the simulation area in figure 3.15b. The calculation itself is expected to be very robust hence neither dispersive nor non-linear or absorbing materials are involved within the calculation. The simulation shows bright localized spots of strong spatial electric field fluctuations $E(\vec{r})^4$. As in the experiment, the incident plane wave is multiply scattering within the cylinder array and different scattering trajectories are interfering with each other forming locally enhanced electric fields. These bright localized spots are the spatial hallmark of localized photon modes and are in general agreement with the experimental results. The spatial confinement of the bright localized spots of the electric field is analysed along the dashed line in figure 3.15b. The resulting cross section in figure 3.15c shows the spatial extent of this hotspot emission. Within the simulation, the hotspots are localized within a small region in the

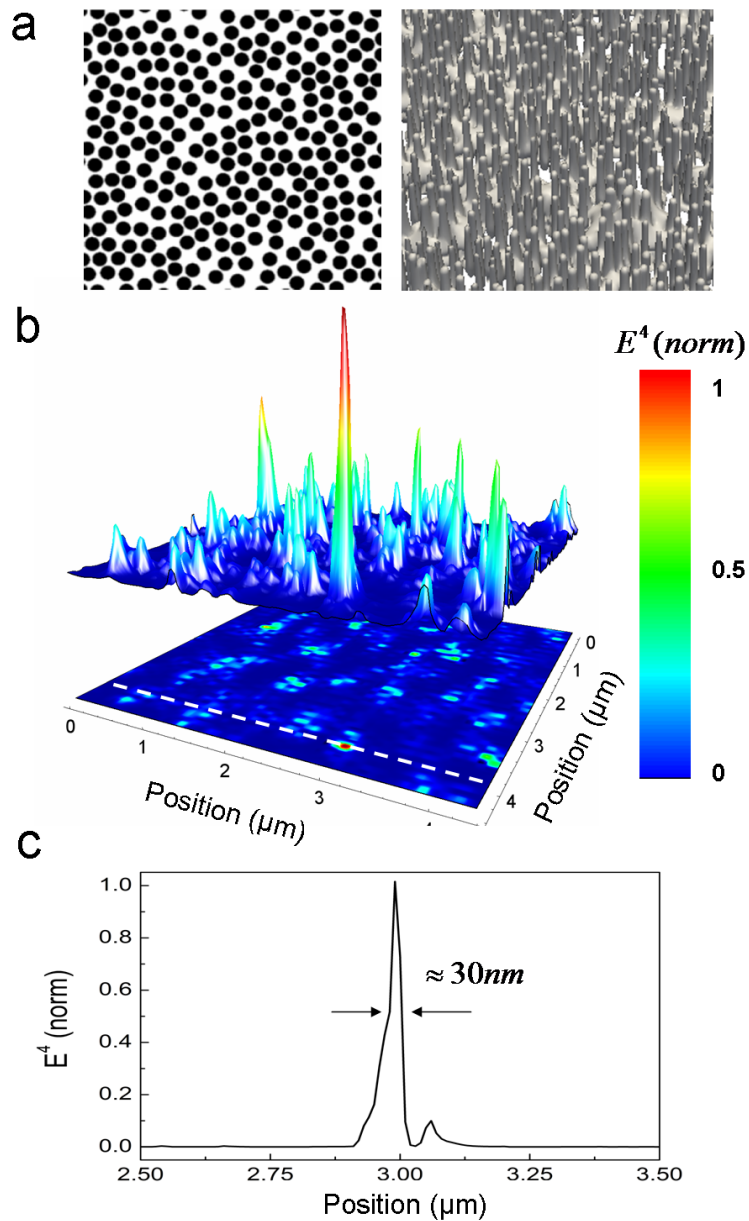


Figure 3.15: **a** Top view (left) and side view (right) of the refractive index $n(\vec{r})$ arranged to simulate randomly arranged dielectric cylinders in vacuum on sapphire. The needle length is randomly varied between $0.9 - 1.0 \mu\text{m}$. The density is set to 55 needles per μm^2 with a diameter of 100nm . **b** Two dimensional intensity distribution of the fourth power of the local electric field $E(\vec{r})$ at large times t for $n(\vec{r})$ calculated by using a three-dimensional FDTD method with a resolution of 10nm . The fourth power of the electric field corresponds to the SH intensity. **c** Cross section along the dashed line delivering the localization on a spatial scale of 30nm .

$E(\vec{r})^4$ map of approximately 30 nm (FWHM) in diameter. This is at least one magnitude smaller than the measured spatial localization in the experiment. In order to verify this behavior, experiments with an increased optical resolution would be highly desirable. Experiments with much higher spatial resolution are presented in chapter 5.

The enhancement of the electric field within the simulation $\kappa = I_{SH_{max}} / \langle I_{SH} \rangle \propto E_{loc}^4 / \langle E^4 \rangle \approx 95$ is much higher than in the experiments. This behaviour can be explained by the different optical resolution. The experiment is performed with a resolution of $\lambda_d = 500\text{ nm}$ measuring at the SH frequency. In contrast, the FDTD simulation is calculated with a spatial resolution of only 10 nm . To compare both, the FDTD calculation has to be convoluted with a Gaussian filter comparable to the experimental resolution. The convolution leads to an averaging of the calculated electric field distribution. This averaging decreases the mean enhancement κ even below the experimentally deduced value, as shown for four different Gaussian filters with an alterable width at FWHM ranging from 10 nm up to 500 nm in figure 3.16. This result

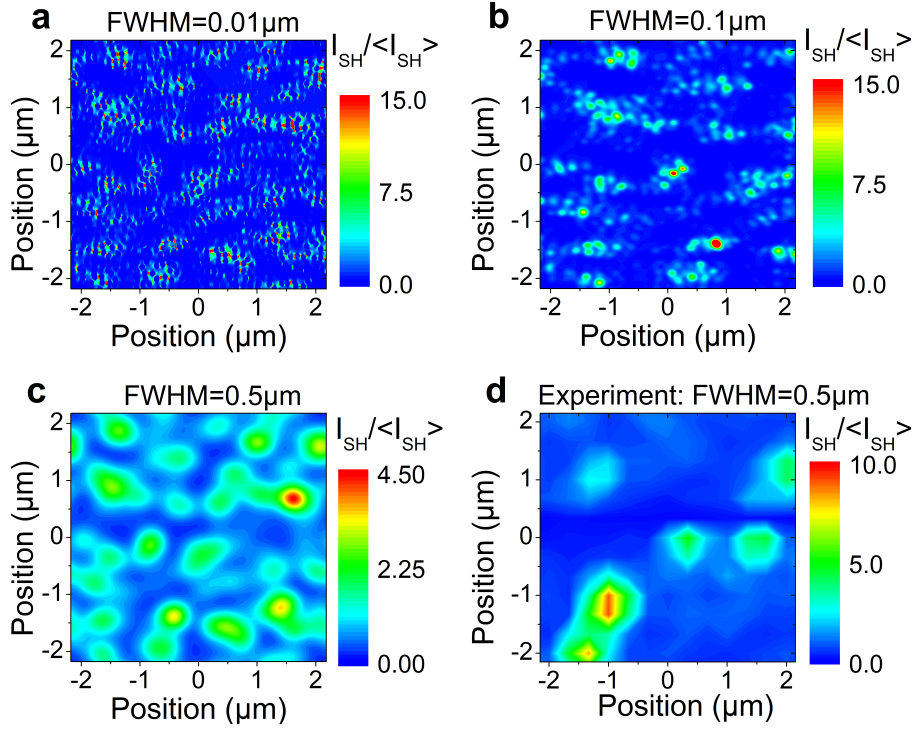


Figure 3.16: **a-c** Calculated spatial intensity distribution convoluted by different Gaussian filters of alterable FWHM widths. **d** Representative section of the spatial localization within the thin ZnO nano-needles from sample 1 to compare the emission with the theoreticly calculated intensity-maps [97].

indicates that the experimentally deduced fluctuations of the electric field are strong. They are even stronger than the calculated fluctuations. The calculated electric fields strongly depend on the geometric distribution of $n(\vec{r})$. Different

geometries varying the distances between the cylinders and their diameter are calculated and shown in section 4.4.

The investigation of the localized photon modes within the cylinders calculated by the FDTD shows different properties:

a) First the influence of the convolution with the Gaussian filter on the number of hotspots is examined. A hotspot within this analysis is defined as a local maximum surrounded by smaller intensity values at each side. The comparison of the number of hotspots m within the spatial intensity distribution deduced by FDTD adapted to the experimental conditions using a Gaussian filter with a FWHM of $0.5\mu m$ (figure 3.16c-d) shows clear deviations from the measured spatial intensity distribution of the thin ZnO nano-needles. It is evident that the density of hotspots within the simulation $m_{FDTD} = 0.5\mu m^{-1}$ is approximately two times larger than in the experiment with the $30nm$ thin ZnO nano-needle array $m_{30nm} = 0.3\mu m^{-1}$ as illustrated by the blue star in figure 3.17. However,

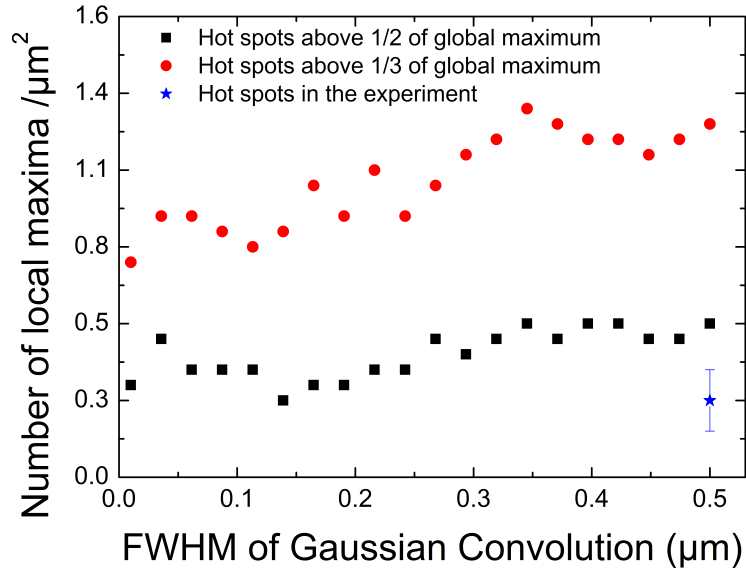


Figure 3.17: Density of local maxima on the calculated $4.5 \times 4.5 \mu m$ grid as a function of the width of the convoluted Gaussian filter. The convolution hardly influences the density of hotspots at $1/2$, respectively $1/3$, of the electric field maximum. The experimentally deduced density of $0.3 \mu m^{-1}$ for the $30 nm$ thin ZnO nano-needle array (blue star) differs significantly from the theoretical values.

the number of hotspots deduced from the calculation stays almost constant for $1/2$ and $1/3$ of the global maximum of $E(\vec{r})^4$ for the different convolutions of the FDTD calculation with Gaussian functions of alterable widths.

b) The enhancement $\eta_{30nm} \approx 80$ between bright and dark modes is detected at $\lambda_d = 400 \text{ nm}$ with an optical resolution of 500 nm . The excitation area is defined by the focus diameter of the reflecting objective to be $1 \mu\text{m}^2$ at the fundamental wavelength. Within this area, approximately 60 needles are illuminated simultaneously. Nevertheless the experimentally deduced density of the hotspots $m_{30nm} = 0.3 \mu\text{m}^{-1}$ already indicates that a hotspot is a rather rare event. In the case of averaging above adjacent modes this would result in a spatial broadening and a much more homogeneous $E(\vec{r})^4$ map.

These arguments support the conclusion that the resolution within the experiment is sufficient to mainly probe a single localized mode. In addition this is supported by the temporal measurement in section 3.3.

The random alignment of the cylinders has a strong influence on the localization and the occurring hotspots in terms of density and intensity. The ZnO nano-needles distributed are more randomly arranged than the cylinders in the simulation, which is even increased by the influence of the underlying layer in the experiment.

However, the excitation of the whole sample at once within the FDTD calculation shows a discrepancy between simulation and experiment. Within the experiment, the sample is only excited in a confined area. Unaware of the exact geometry and shape of the investigated area, it is difficult to compare the results in detail. Nevertheless, all these deviations within the FDTD calculation from the experimental conditions and the unique characteristics to the spatially localized and strong electric fields show a good agreement. Many different variations are still under investigation. Including the underlying layer of cones bringing the simulation closer to the experimental results. However, this will not be explained here.

3.2.5 Single scaling parameter

One way to classify the localization strength of light is based on the single scaling theory, as already introduced in section 2.2.5 [59, 72]. Thouless argued that localization sets in if the level width ∂E is smaller than the level separation ΔE of the Eigenmodes, as described by equation 2.39 which allows a connection between the spectrum and the transport [60], i.e. between the spectrum and the single scaling parameter. This single scaling parameter $g = \partial E / \Delta E$ governs all aspects of localization, including statistical fluctuations, and is used as a quantitative measure of the localization strength g [10, 61]. In the following, the semi-analytical model derived from Nieuwenhuizen and van Rossum [63] calculates the intensity distribution of a propagating wave through a multiply scattering medium for certain values of g . Therefore the localization strength is classified by the intensity fluctuations. The single scaling parameter g allows to distinguish between the weak and strong localized regimes. The transition from one regime to the other occurs at $g = 1$. Values of $g < 1$ denote stronger localization within the sample.

The model derived from Nieuwenhuizen and van Rossum describes the intensity fluctuations at the fundamental frequency. Therefore the intensity distribution at fundamental frequency I is calculated from the measured spatial SH intensity distribution I_{SH} . The relative probability on logarithmic scale of I normalized to the mean emission intensity $\langle I \rangle$ is shown in a histogram for the different investigated samples in figure 3.18. The histogram of the intensity values

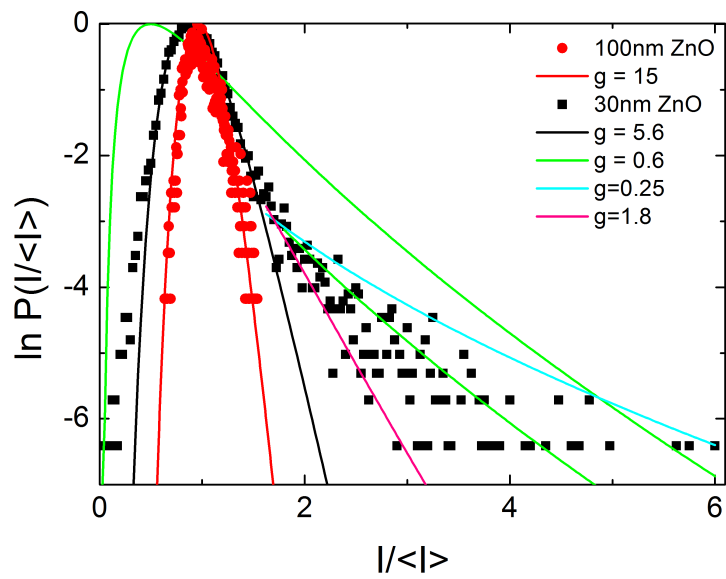


Figure 3.18: Logarithmic probability distribution $P(I/\langle I \rangle)$ of the normalized intensity distributions of the 100 nm thick and 30 nm thin ZnO nano-needle arrays with the corresponding single scaling parameter g . The histogram of the 30 nm thin ZnO nano-needle array shows two signatures. A part described by $g = 5.6$ and a part above $1.8 \cdot \langle I \rangle$ with $g = 0.6$. The part above $1.8 \cdot \langle I \rangle$ is between $g = 0.25$ and $g = 1.8$ acting like an error bar in the determination of the localization strength. The emission intensity of the 100 nm thick ZnO nano-needle array is Gaussian distributed and described by $g = 15$.

I_{100nm} corresponding to the emission from the 100 nm thick ZnO nano-needle array show a Gaussian distribution centered around $I_{100nm}/\langle I_{100nm} \rangle = 1$. This behaviour reflects the weak fluctuations in the spatial intensity map I_{SH} and the low value of κ .

In contrast, the histogram of intensity values corresponding to the emission of the 30 nm thin needles shows a more complex distribution of I_{30nm} . The histogram of the thin needle array is a composition of two different distributions. Most of the intensity values are again Gaussian distributed. In addition to the dominating Gaussian distributed part for values below $1.8 \cdot I_{30nm}/\langle I_{30nm} \rangle$, a deviation from the Gaussian distribution at larger intensity values than $1.8 \cdot I_{30nm}/\langle I_{30nm} \rangle$ can be observed. The origin of this deviation, described by a log-normal distribution, are the bright emission spots, i.e the pronounced fluctuations of I_{SH} shown in figure 3.12. The hotspot emission leads to the characteristic shift of the maximum of the histogram to $I_{30nm}/\langle I_{30nm} \rangle \approx 0.9$ as already shown in section 2.2.5.

In order to classify the localization strength, the single scaling parameter is adjusted to match the experimentally deduced intensity distribution $P(I/\langle I \rangle)_{exp}$ by using the least square calculation χ^2 described in equation 3.6. The value

$$\chi^2 = \sum (P(I/\langle I \rangle)_{exp} - P(I_n))^2 \quad (3.6)$$

takes a minimum for the best matching fit by comparing the experimental distribution to the calculated probability distribution $P(I_n)$ (equation 2.40) [96]. For the best fit between the calculated and experimentally deduced intensity distributions, the χ^2 value takes a minimum. In the case of the 100 nm thick ZnO nano-needle array, this results in a value of $g_{100nm} = 15$. The description of the histogram for the intensity values of the 30 nm thin ZnO nano-needles in terms of g is challenging. By using a value of $g = 0.6$, a strong discrepancy of the calculated distribution (green solid line) and the experimental results (black squares) is obvious, as can easily be seen from figure 3.18. The dominating Gaussian distribution and the log-normal distribution influence each other in the histogram. Therefore, the histogram can simply not be described by a single value of g . However, the Gaussian distribution does not effect the slope of the histogram for values above $1.8 \cdot \langle I \rangle$. Consequently the localization strength is determined for the Gaussian distribution and log-normal distribution of I_{30nm} individually by using the least square method for the intensity values below and above an intensity threshold of $1.8 \cdot \langle I_{30nm} \rangle$. The behaviour of χ^2 as a function of g for the thin ZnO nano-needle array is shown in figure 3.19. This results in a single scaling value of $g = 5.6$ for the Gaussian distributed part of the histogram of the thin needles. For the case of the log-normal distributed part of the histogram, the single scaling parameter is estimated at $g = 0.6$

As mentioned earlier, the large value of $g_{100nm} = 15$ indicates delocalized photon modes within the 100 nm thick ZnO nano-needle array. In the case of the 30 nm thin ZnO nano-needle array both phenomena, localized and delocalized photon modes, can be found. Most of the modes correspond to a single scaling parameter of approximately $g = 6$, which describes delocalized photon modes. However, a small fraction is described by $g = 0.6$. Therefore, the hotspots can be identified as localized photon modes.

In order to estimate the precision in the calculation of the localization strength, additional distributions for certain values of g are plotted. The less in-

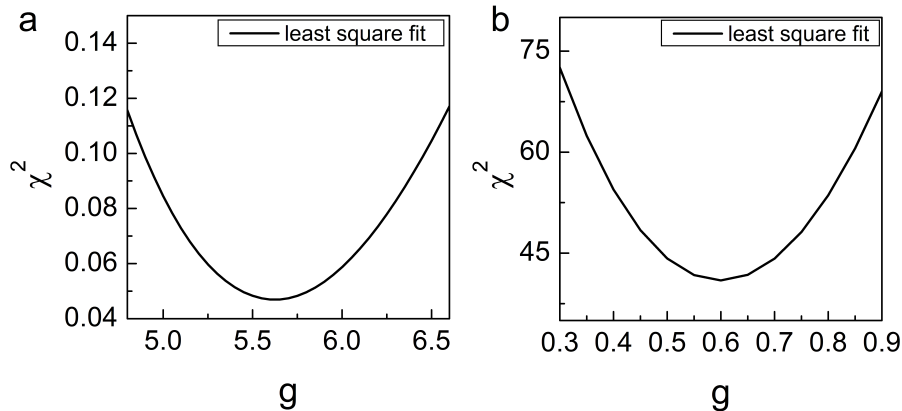


Figure 3.19: Least square value χ^2 as a function of single scaling parameter g of the Gaussian distributed part in **a** and the log-normal distributed part above $1.8 \cdot \langle I \rangle$ in **b** of the histogram of the thin ZnO nano-needle array. The minimum of the distribution equals the best fitting value of the single scaling parameter describing the experimental results.

tense intensity values in the histogram can best be described by $g = 1.8$ whereas the most intense values are described by $g = 0.25$. These additional distributions can be seen as "error bars" within the calculated localization strength which is in between. This finally allows the classification of the electric field within the hotspot to be at least at the transition from weak to strong localization within the investigated sample of 30 nm thin ZnO nano-needles.

The FDTD simulation shows very strong hotspots, but the resolution of the calculation differs from the experimental resolution. In order to consider this, the spatial intensity map is convoluted with Gaussian filters of different widths. The FDTD intensity distributions are strongly influenced by the Gaussian width of the convolution. For a width corresponding to the optical resolution, this results in a decreased value of the FDTD enhancement at SH $\kappa_{FDTD} \approx 4$, which is much smaller than the value measured for the thin ZnO nano-needle array $\kappa_{30nm} \approx 33$. Beside the intensity the histogram and consequently the corresponding single scaling parameter are influenced by the convolution. The resulting histograms with their associated values of g are shown in figure 3.20. The single scaling parameter deduced for a Gaussian width of 500 nm for the FDTD calculation shows a huge discrepancy from the experimentally deduced value. Within the FDTD, it is described by $g_{FDTD500nm} \approx 4$ which is far from the experimentally deduced value of $g_{30nm} = 0.6$. This might be due to the simplification of the ZnO sample with simple cylinders. Additional calculations, which are not part of this thesis¹, implementing an underlying layer of cones below the thin cylinders change the shape of the histogram and lead to a deviation from the almost Gaussian distribution of the convoluted FDTD calculation. The influence of the arrangement of needles and underlying layer within the FDTD calculation is still under investigation and will be discussed in a further publication.

¹Part of the work by David Leipold and not shown in this thesis

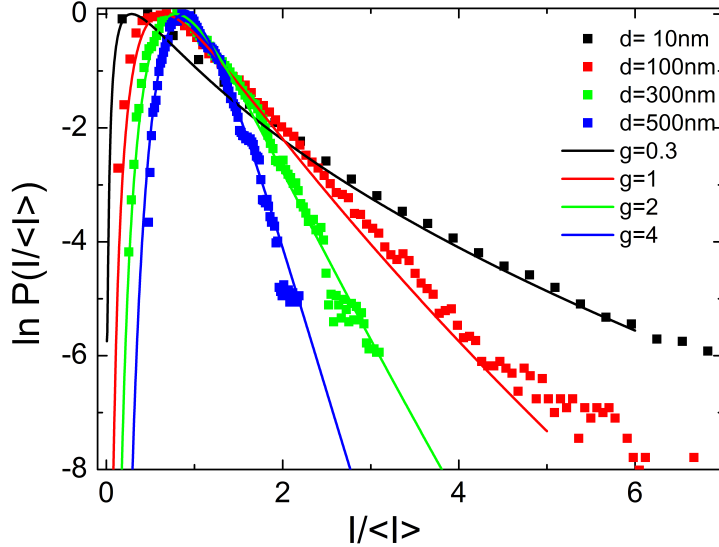


Figure 3.20: Convolution of the FDTD calculation with a Gaussian function to match the experimental resolution changes in the probability distribution as well as the estimated single scaling parameter.

3.2.6 Multifractal analysis of the spatial intensity distributions

The strength of localization can also be classified using the multifractal analysis that has been presented in section 2.2.6. The singularity strength α , also called the Hölder exponent, can be used to classify the localization strength [36]. α is calculated from the spatial intensity distributions for the 100 nm thick and 30 nm thin ZnO nano-needle arrays. In addition, it is calculated for the FDTD calculation and for a theoretical log-normal distribution in order to rank the experimental results and to support the classification of the localization strength deduced in the previous section 3.2.5.

By using the description from Chhabra and his co-workers [64], the multifractal analysis requires a sufficient small box size, i.e. a sufficient scanning resolution within the experiment. The performed spatial measurements fulfill this criterion with a resolution of 333 nm, which is smaller than the optical resolution of the SH microscope.

The measured intensity distribution of the two dimensional spatial SH emission $I_{SH}(x, y)$ is transformed to a one-dimensional array $I_{SH}(s)$. The length of $I_{SH}(s)$ is then described by $x \cdot y$. This new one-dimensional SH intensity array is used to calculate the normalized intensity at the fundamental frequency I .

$$I = \frac{\sqrt{I_{SH}}}{\langle \sqrt{I_{SH}} \rangle} \quad (3.7)$$

The original dimension of the spatial distribution $I_{SH}(x, y)$ is considered in the one-dimensional array I by $L = \text{length}(I)^{1/2}$ in the case of $x = y$. The samples are assumed to be quasi two-dimensional due to the short length of the ZnO nano-needle arrays of only a few μm in the z-direction. The calculated singularity spectrum $f(\alpha)$ of the different samples is shown in figure 3.21. Strong

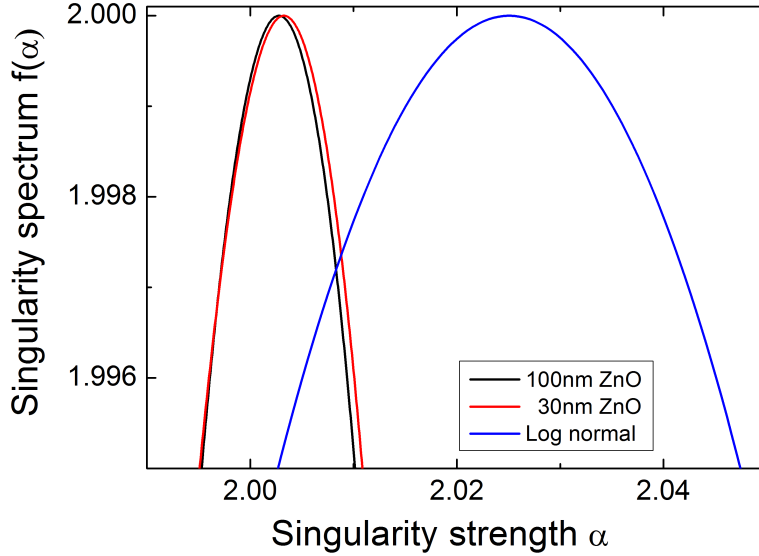


Figure 3.21: Singularity spectrum $f(\alpha)$ as a function of the singularity strength α . The calculated singularity spectrum of the thick and thin ZnO nano-needles show only a weak deviation of the maximum from $\alpha = 2$. The maxima of the theoretical log-normal distribution as well as the FDTD calculation show much stronger singularity strengths.

fluctuations in the one-dimensional array I results in the broad spectral width of $f(\alpha)$ and a shift of the maximum towards larger Hölder exponents. Delocalized photon modes have a singularity spectrum centered at $\alpha = 2$ in two dimensions anyway, as shown in section 2.2.6. The deviation from $\alpha = 2$ of the maximum of $f(\alpha)$ is therefore used to describe the localization properties.

The maximum of the singularity spectrum of the 100 nm thick ZnO nano-needle array shows only a weak deviation in its maximum to higher singularity strengths (Hölder exponent) of $\alpha_{100nm} = 2.002$. This indicates delocalized photon modes within the 100 nm thick ZnO sample supported by the classification based on the single scaling parameter g .

Interestingly, the calculated singularity spectrum of the 30 nm thin ZnO nano-needles does not show any big difference compared to the result of the thick needles. The singularity strength of the thin needles $\alpha_{30nm} = 2.003$ is only slightly stronger than α_{100nm} . This behaviour differs strongly from the results of the previous section. Within the analysis of the localization strength by using the single scaling parameter different histograms of both investigated samples were observed (figure 3.18). However, the deduced histogram in figure

3.18 indicates, that only a small fraction of the intensity values of the 30 nm thin ZnO nano-needle array can be attributed to localized photon modes, as identified by the log-normal distributed part described by $g < 1$. A deviation from $\alpha = 2$ is only expected for these values. Restricting the calculation of the singularity strength to intensity values above a certain threshold of $1.8 \cdot \langle I \rangle$ does not deliver trustworthy results. This is due to the calculation of the singularity strength, which analyses the fluctuations of the intensity. Restricting the calculation of the singularity spectrum to localized states above a certain intensity threshold I_{thres} reduces the dynamic range of the intensity fluctuations and therefore the Hölder exponent gets smaller as for analysing all intensity values. The delocalized photon modes however dominate the multifractal analysis as can be seen calculating the singularity spectrum of a theoretical log-normal distribution comparable to the localized part in the measurements. The theoretical log-normal distribution with a maximum intensity of $max(I / \langle I \rangle) \approx 6.5$ and a mean value of 1 has a broadened singularity spectrum and a maximum $\alpha_{log} = 2.024$. The shift of α_{log} to a higher singularity strength indicates localized photon modes within the theoretically assumed distribution. Furthermore, it confirms the problem of multifractal analysis concerning mixed intensity distributions.

In conclusion, the multifractal analysis is not a tool which is suitable for the classification of the localization strength for a mixed system of localized and delocalized states.

3.3 Temporal structure of the electric field

After the experimental verification of the spatial localization of photon modes within the 30 nm thin ZnO nano-needle array, the distinct modification of the temporal structure of the local electric field will experimentally be verified. Localization induced by multiple scattering must be accompanied by a distinct modification of the temporal structure of the local electric field as theoretically demonstrated by Stockman [27]. The multiple scattering results in a superposition of different modes j at the resonance frequencies ω_j . The electric field is then described by

$$\vec{E}(\vec{r}, t) = \sum_j \vec{E}_j(\vec{r}) e^{-i\omega_j t - \gamma t} \quad (3.8)$$

with the decay constant $\gamma = 1/\tau$ which is related to the lifetime τ of the mode. The lifetime of the localized photon modes will be investigated experimentally in this section. Due to the short lifetime of localized photon modes in nano-structures, a technique which provides femtosecond time resolution is necessary. Therefore, the set-up is modified to a time-resolved ultra fast SH microscope by using interferometric frequency resolved autocorrelation (IFRAC). The measured time traces are compared to calculations by optical Bloch equations to analyse the temporal structure of the localized photon modes. This technique allows to spatially resolve the lifetimes of local photon modes with femtosecond time resolution and on sub-wavelength length scales. In addition, the deduced lifetimes of localized photon modes within the ZnO needle structures are verified by theoretical time resolved FDTD calculations.

3.3.1 Experimental Set-up

In order to verify the prediction of enhanced lifetimes of localized electric fields, the SH microscope set-up has been expanded by a Mach-Zehnder interferometer, shown schematically in figure 3.22. First order IFRAC measurements based on the linear emission at the fundamental wavelength does not deliver information about the spectral phase [88]. The SH microscope in combination with the interferometer is therefore particularly well suited. By detecting the SH, the set-up provides insight to the spectral phase of the electric field [88] and therefore allows a complete characterization of the local electric field on spatial scales of 500 nm.

Within the set-up, dispersion controlled 6 fs laser pulses are split into pulse pairs using a Mach-Zehnder interferometer. It consists of two beam splitters (Femtolasers Dielectric 50% beam splitters sub 7 fs p-polarized (FO002)) and a variable delay τ with a precision of 50 as. The pulse pair is focused onto the sample by the allreflecting objective and the light emitted from the sample is then detected in reflection geometry. It is, therefore, separated from the fundamental wavelength by a cold mirror, spectrally resolved in the monochromator (Acton 2500i) and detected with the liquid- N_2 cooled CCD camera (Ropers Scientific). By using this experimental set-up, the emission from the sample is detected spectrally resolved as a function of the time delay between the pulse pair at different emission spots on the sample.

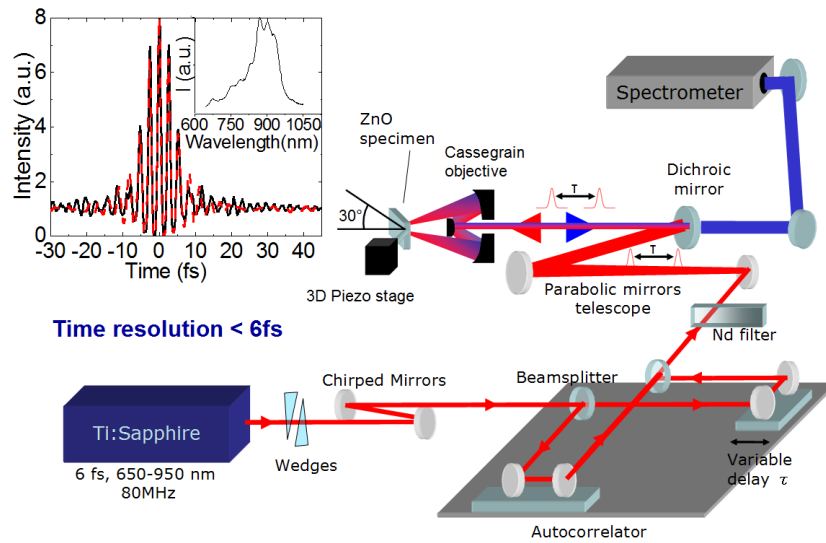


Figure 3.22: **a** Schematic illustration of the experimental set-up: Ultrashort, dispersion-controlled 6 fs laser pulses are splitted into pulse pairs in a dispersion-balanced Mach-Zehnder interferometer. They are then focused onto the sample by the allreflecting objective. The emitted light from the sample is detected in reflection geometry, separated from the fundamental light by a dichroic mirror and spectrally resolved using a monochromator in combination with a CCD-camera. The temporal resolution of the set-up is proven by the interferometric autocorrelation (IAC) trace of the focused pulses in the focal plane of the objective shown in the inset. The measured IAC trace (black solid line) is compared to a dispersion-free IAC trace (red dashed line), simulated by using the measured spectrum (inset).

3.3.2 Interferometric Frequency Resolved Autocorrelation

In order to demonstrate the enhanced lifetimes of localized photon modes at spatial hotspot positions, the interferometric frequency resolved autocorrelation (IFRAC) method at the SH frequency is used. Therefore, in a first step, the SH spectra from a beta barium borate (BBO) crystal as a function of the time delay τ between the pulse pair are recorded spectrally resolved. The BBO crystal is well-suited for the temporal characterization of ultrashort laser pulses due to its high optical nonlinearity and its very rapidly decaying induced polarization. The thickness of the BBO strongly influences its spectral acceptance. To measure ultrashort laser pulses, thin crystals are necessary [88]. Therefore, a $10\mu\text{m}$ thin BBO crystal is used to measure the electric field within the focal plane of the set-up, which serves as a reference in the following.

The recorded interferometric frequency resolved autocorrelation (IFRAC) trace $I_{IF}(\lambda, \tau)$ of the BBO is shown as a function of the wavelength λ and the time delay τ in figure 3.23a. The retrieval of the real value of the electric field

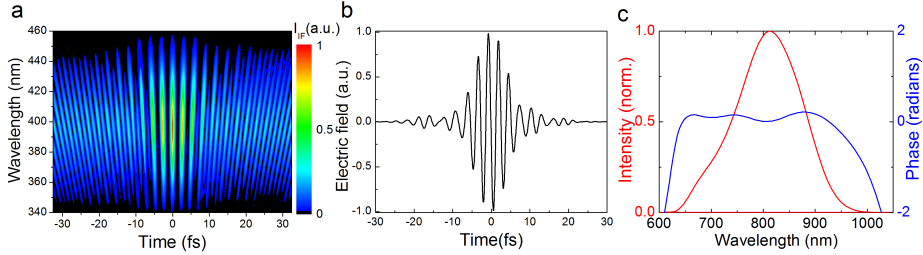


Figure 3.23: **a** IFRAC trace recorded by using a $10\mu\text{m}$ thin BBO crystal. **b** Retrieved real value of the electric field using a commercial FROG algorithm. **c** Spectral phase (blue) and intensity (red) at the fundamental wavelength.

from the IFRAC trace requires the analysis of the amplitude and the spectral phase. A direct solution to this problem does not exist. So an iterative procedure based on the minimization of the discrepancy between a simulated IFRAC trace and the measured trace by adjusting the spectral phase is used [88]. Therefore, a commercial FROG algorithm² is used. The IFRAC trace can be decomposed by a Fourier transformation to its frequency components as described in section 2.4. The spectral phase can be reconstructed from each of the spectral bands. However, the commercial algorithm retrieves the electric field based on the analysis of the DC base band. The DC base band, the signal around zero frequency in the Fourier transform, is therefore isolated by a super Gaussian filter in the Fourier transformed IFRAC trace $\tilde{I}_{IF}(\lambda, \nu) = \frac{1}{\sqrt{2\pi}} \int I_{IF}(\lambda, \tau) e^{-2\pi\nu\tau} d\tau$. By isolating the DC base band, this results in the known frequency resolved optical gating trace (FROG)[73] allowing the use of the commercial retrieval procedure.

The retrieved electric field at the fundamental wavelength is shown in figure 3.23b. A pulse duration of 6.5 fs (FWHM) is estimated from the envelope of the electric field structure. An almost flat spectral phase, shown together with the fundamental spectrum in figure 3.23c, allows the conclusion that the electric field measured for the BBO is essentially the one of the bandwidth limited laser

²FROG Version 3.2.2 Femtsoft Technologies

pulse.

In a second step the temporal evolution of the local electric field is investigated at different spatial positions on the sample of 30 nm thin ZnO nano-needles. Two positions are chosen as an example to determine the lifetime of the local electric field: a position outside and a position inside a hotspot. The resulting IFRAC traces $I_{IF}(\lambda, \tau)$ are shown with the IFRAC measurement of the BBO crystal, which acts as a reference, in figure 3.24a-c. A comparison of the measured IFRAC traces with each other along the time axis shows hardly any obvious change. However, strong changes along the spectral axis can be seen when comparing the different traces. The spectral width clearly differs for the three shown cases. For the BBO, the emission ranges from $345\text{--}450\text{ nm}$, whereas it decreases in a position outside of a hotspot to $350\text{--}440\text{ nm}$. In a position within a hotspot, it is even more decreased and ranges only from $360\text{--}425\text{ nm}$. Although the differences of the IFRAC traces along the time-axis seem to be

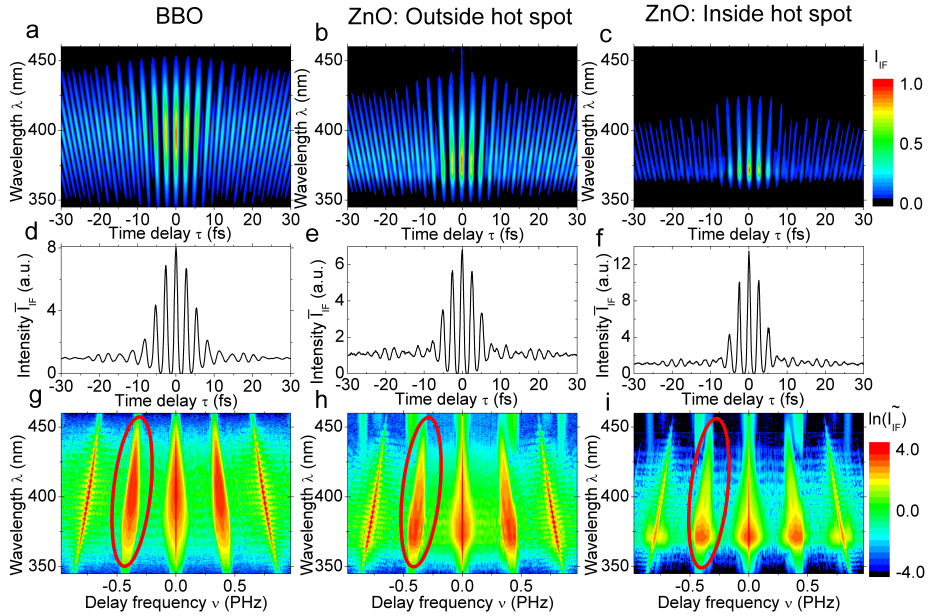


Figure 3.24: Recorded IFRAC traces $I_{IF}(\lambda, \tau)$ exciting the different samples with a 6 fs pulses focused to $1\mu\text{m}$ as a function of the time delay between the laser pulses. **a**: IFRAC trace of the $10\mu\text{m}$ thick BBO which acts as a reference. **b**: IFRAC trace at a position outside a SH hotspot. **c**: IFRAC trace at a position inside a SH hotspot. **d-f**: Interferometric autocorrelations deduced spectrally integrating the corresponding IFRAC traces. The non Gaussian spectrum of the incident laser pulse leads to slight beatings between 10 and 20 fs time delay. **g-i**: Corresponding Fourier transforms of the IFRAC traces along the time axis. The decreasing spectral width from a broad spectral emission for the BBO towards a narrow spectral emission width is marked by red ellipses. [97]

marginal, they are analysed in more detail by calculating the interferometric autocorrelation trace (IAC) $I_{IAC}(\tau) = \int I_{IF}(\lambda, \tau) d\lambda$. The resulting IAC traces are shown in figure 3.24d-f. The IAC of both ZnO measurements show slight

additional oscillations at around $\tau = 20$ fs which are more pronounced compared to the reference IAC of the BBO crystal. The enhancement of a IAC trace ζ is described by the ratio of the emitted intensity at perfect temporal overlap of the pulse pair $I(\tau = 0)$ and the intensity emitted individually of each of the two laser pulses separated by a time delay $I(\tau \rightarrow \infty)$. The enhancement is an important factor to verify the nonlinearity b of the emission process. By considering the relation $I \propto |E|^2$ of the electric field E and the influence of the nonlinearity, the enhancement is defined by

$$\zeta(b) = \frac{I(\tau = 0)^b}{I(\tau \rightarrow \infty)^b} = \frac{(2E)^{2b}}{E^{2b} + E^{2b}} = 2^{2b-1} \quad . \quad (3.9)$$

The enhancement value known from the literature based on a second harmonic process $\zeta(2) = 8$ [88] fits perfect to the deduced enhancement of the BBO IAC trace $\zeta_{BBO} = 8$. The enhancement of the IAC-trace for the position outside of the hotspot $\zeta_{out} = 7$ is slightly less compared to the BBO. However, the IAC for the hotspot position shows the largest enhancement of $\zeta_{hot} = 13$ compared to the reference. This behaviour is due to a higher nonlinearity. In addition, the IAC at a hotspot position looks shorter in time as the reference. This behaviour is owned as well by the higher nonlinearity.

In order to analyse this behaviour in more detail, the whole IFRAC trace is analysed. Therefore, the Fourier transforms along the time axis $\tilde{I}_{IF}(\lambda, \nu)$ with the delay frequency ν is calculated and plotted on a logarithmic intensity scale in figure 3.24g-i. It provides a more detailed analysis of the recorded spectra. A closer look to $\tilde{I}_{IF}(\lambda, \nu)$ shows additional incoherent emission from the ZnO samples. The incoherent emission is indicated (see section 2.4.1) by the appearing vertically aligned lines in figure 3.24h and i. They are not observed in the Fourier transform of the BBO IFRAC in g. The incoherent emission influences the retrieval of the fundamental electric field as it is in the same spectral area as the coherent SH emission. The retrieval of the electric field structures for the ZnO measurements is therefore much more complicated, since the spectral emission is accompanied by the incoherent emission from the band-gap transition and green photoluminescence. Both processes are known to occur in ZnO [71]. The incoherent influence, which changes the enhancement to $\zeta_{hot} = 13$, is sufficiently strong to make the commercial retrieval procedure vulnerable.

However, the change from a broad spectral emission from the BBO crystal towards a narrow spectral emission for the position within the hotspot can be used to deduce the lifetime of the electric field, since the spectral width is associated with the lifetime of the electric field as long as a pure coherent process is assumed. The strong reduction of the coherent spectral width of the hotspot emission is already a signature of the increased lifetime of the localized photon mode within the random array of ZnO nano-needles. Therefore a retrieval process based on the spectral width of the measured emission spectra is favoured, which will be explained in the following.

Retrieval of the local electromagnetic field by using optical Bloch equations

To describe the experimental results presented in the previous section, and in particular to retrieve the time structure of the local electric field inside the 30 nm thin ZnO nano-needle array, an optical Bloch equation model for the interaction

of the incident light field with a single localized mode is introduced. We implicitly assume that the spatial resolution of the experiment is sufficiently high such that the collected SH signal is mainly emitted from this individual mode that couples to the incident light. We will later on (section 3.3.3) verify this approach by comparing the results of the model to numerical three-dimensional FDTD simulations of the nonlinear response of such a nano-needle array. In this model, the coupling of the localized light mode to the ZnO needle is treated in a very phenomenologized picture. It is treated as an effective two level system with an energy difference corresponding to the band gap of ZnO. The retrieval of the local electric field is based on the light-matter interaction described by optical Bloch equations introduced in section 2.3. The two-level system consists of a ground $|0\rangle$ and an excited state $|1\rangle$. In order to describe the nonlinear two-photon excitation process, the Hamilton operator H_1 with a generalized Rabi frequency $\Omega = d_{01}^{(2)} E(t)^2 / \hbar$ (equation 2.63 and 2.68) is used to match the experimental results. The resonance frequency of the ground state is set to $\omega_0 = 0$. By using this simplified model based on optical Bloch equations, the lifetime of the optical mode $T1$ and the resonance frequency of the excited state ω_1 are the only free variables to match the experimental results.

A change of the resonance frequency ω_1 leads to a shift of the spectrum and changes also the coupling efficiency of the incident electromagnetic wave to the excited state. However, the depletion of the ground state is avoided by controlling the strength of the nonlinear dipole-operator $d_{01}^{(2)}$. Best spectral match to the measured emission spectrum of the BBO and ZnO samples is achieved by setting $\omega_{1_{BBO}} = 2.0 \cdot \omega_{L_0}$ and $\omega_{1_{ZnO}} = 2.2 \cdot \omega_{L_0}$ with ω_{L_0} as the central angular frequency of the incident laser spectrum shown in the inset of figure 3.22. The same spectrum is used to calculate the incident electric field which couple to the two level system. Within this calculation, the spectral phase is assumed to be flat, which results in a Fourier-limited laser pulse with a pulse duration of 6 fs. This assumption is satisfied by the IFRAC measurement of the BBO crystal with an almost flat spectral phase shown in figure 3.23. Furthermore, the light matter interaction is treated in a semi-classical way. Therefore, the incident electromagnetic field is assumed to be sufficiently strong, not to be influenced or changed by the interaction with the two level system. The lifetime $T1$ of the mode strongly influences the polarization of the excited state, which is described by the density matrix element $\rho_{01}(t)$. The electric field at the SH frequency emitted by the two-level system is calculated by using the relation

$$E_{SH} \propto \rho_{01} \quad . \quad (3.10)$$

Therefore, the lifetime of the excited state has a direct influence on the spectral width of the generated electric. The envelope of the electric field at the SH frequency

$$S(t) = \sqrt{E_{SH}(t) \cdot E_{SH}(t)^*} \quad (3.11)$$

is calculated by using the complex conjugated electric field E_{SH}^* . Together with the phase $\phi_{SH}(t)$ and the central frequency ω_{L_0} , it allows a complete characterization of the electric field at the SH frequency

$$E_{SH}(t) = S(t) \cdot \exp(-i\phi_{SH}(t) - i \cdot 2\omega_{L_0}t) \quad . \quad (3.12)$$

The retrieved complex electromagnetic field already contains all necessary in-

formation to calculate the field at fundamental frequency. The phase

$$\phi_{SH}(t) = \arctan\left(\frac{\text{Im}(E_{SH}(t))}{\text{Re}(E_{SH}(t))}\right) - 2\omega_{L_0}t \quad (3.13)$$

can be deduced by using the real and imaginary part of E_{SH} and subtracting the fast oscillating term at the central frequency of the SH. The knowledge about $S(t)$ and $\phi_{SH}(t)$ allows to calculate the electric field at the fundamental wavelength by using

$$E(t) = \sqrt{E_{SH}(t)} = \sqrt{S(t)} \cdot \exp(-i(\phi_{SH}(t)/2) - i \cdot \omega_{L_0}t) \quad (3.14)$$

The electric field at the fundamental frequency is the result, we are finally interested in. It describes the lifetime of the local photon mode. In order to compare the calculated electric fields to the measurements, the spectrum I_{SH} has to be calculated based on the time dependent field $E_{SH}(t)$. The spectrum

$$I_{SH}(\nu) = \text{FFT}(E_{SH}(t)) \cdot (\text{FFT}(E_{SH}(t)))^* \quad (3.15)$$

is obtained by the squared value of the Fast Fourier Transformed (FFT) electric field at the SH frequency $E_{SH}(t)$ and its complex conjugated. For a direct comparison with the experimental spectra, it is transformed to the wavelength domain $I_{SH}(\lambda)$.

The solution of the optical Bloch equation delivers best spectral match by setting the lifetime of the excited state to $T1_{BBO} = 1$ fs, $T1_{outside} = 3.5$ fs and $T1_{inside} = 6.5$ fs for the three different cases. This corresponds to the dephasing times of the polarization of $T2_{BBO} = 2$ fs, $T2_{outside} = 7$ fs and $T2_{inside} = 13$ fs. The corresponding real parts of the electric fields at the SH frequency $E_{SH}(t)$ for the three different retrieval calculations are shown together with the envelope $S(t)$ in figure 3.25.

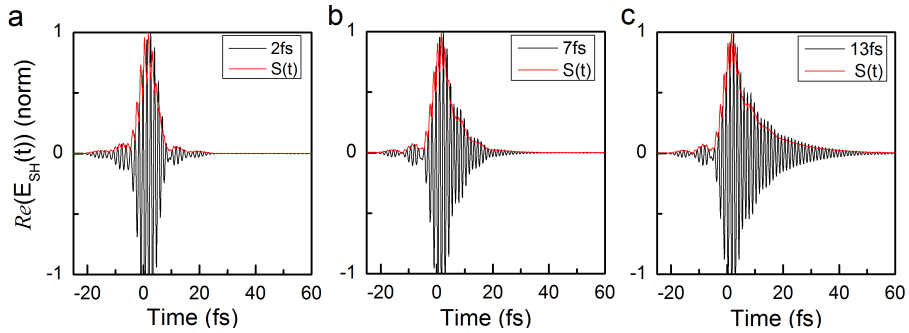


Figure 3.25: Real parts of the normalized electric fields at the SH frequency (black line) and the envelope $S(t)$ (red line) for (a) the BBO crystal with a lifetime of the photon mode of $T1 = 1$ fs, (b) a position outside of a hotspot with $T1 = 3.5$ fs and (c) for a position inside of a hotspot with $T1 = 6.5$ fs.

In a next step, the optical Bloch equations are solved for each time delay τ of the pulse pair $E_p(\tau) = E(t) + E(t + \tau)$, generated in the interferometric autocorrelator. Again the spectrum $I_{SH}(\lambda)$ is deduced at each time delay, which finally results in the IFRAC trace $I_{IF}(\lambda, \tau)$. The IFRAC trace is individually

calculated for each of the three measurements, represented by the three population lifetimes $T1$ of the excited state. The calculated traces $I_{IF}(\lambda, \tau)$ for the BBO, a position outside and a position inside of the hotspot are shown together with the Fourier-transformed IFRAC traces $\tilde{I}_{IF}(\lambda, \nu)$ and the corresponding real parts of the electric fields at the fundamental wavelength in figure 3.26. As in the experiment, the retrieved IFRAC traces $I_{IF}(\lambda, \tau)$ show a decreasing

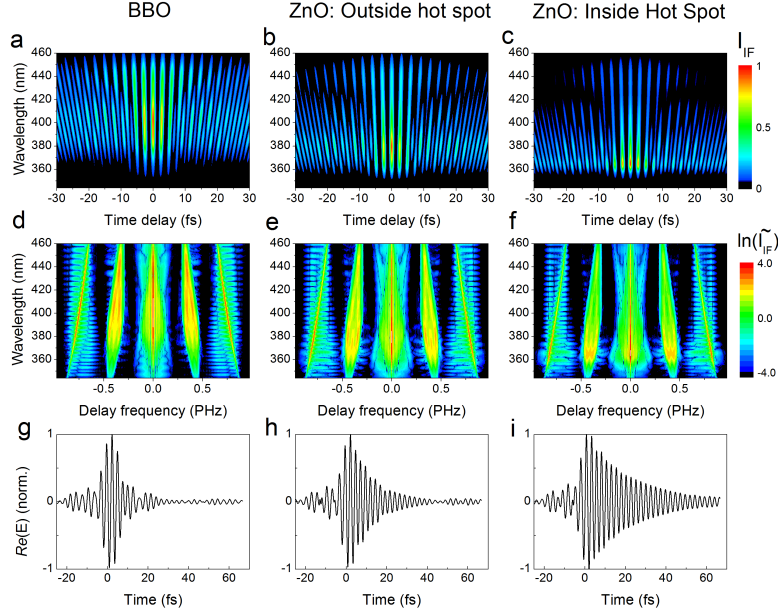


Figure 3.26: **a-c** Calculated IFRAC-traces $I_{IF}(\lambda, \tau)$ retrieved by solving a two-photon excitation of a two-level system by an ultrashort laser pulse using optical Bloch equations. The dephasing time $T2$ is adapted to match the experimental data in 3.24g-i for **(a)** the BBO crystal with a lifetime of the excited state of $T1_{BBO} = 1$ fs, **(b)** a position outside of a hotspot with a dephasing time of $T1_{outside} = 3.5$ fs and **(c)** for a position inside of a hotspot with $T1_{inside} = 6.5$ fs. **d-f** The corresponding calculated Fourier-transforms $\tilde{I}_{IF}(\lambda, \nu)$ of the IFRAC-traces $I_{IF}(\lambda, \tau)$ are plotted on a logarithmic intensity scale. The change in the emitted spectral width from a broad spectral emission for the BBO towards a narrow emission width for a position inside of a hotspot is clearly visible. **g-i** Normalized real parts of the electric fields at the fundamental frequency. For the hotspot position in **i** the electric field persists for approximately 20 fs (FWHM).

spectral width from a broad spectral shape for $T1_{BBO} = 1$ fs towards a narrow spectral emission for $T1_{inside} = 6.5$ fs, which corresponds to the hotspot position. The retrieved spectral width, as well as the central frequency matches quite good to the experimental results. In contrast to the experimental traces, the retrieved traces show only coherent SH radiation.

The retrieved electric field corresponding to the BBO measurement results in a pulse duration of approximately 6.5 fs (FWHM). This value and also the temporal structure of the deduced electric field are in good agreement with the results obtained by using the commercial FROG algorithm in figure 3.23. Both meth-

ods show the electric fields of a nearly bandwidth limited laser pulse attesting the retrieval method based on optical Bloch equations to be functional.

The retrieved electric field at fundamental frequency for the case of $T1_{outside} = 3.5$ fs already shows an increased lifetime of the photon mode in contrast to the BBO measurement. The amplitude of the envelope of the electric field shows an exponential decay on a time scale of approximately 10 fs (FWHM). This behaviour is even stronger for the case of $T1_{inside} = 6.5$ fs. In that case, representing the hotspot emission, the envelope of the electric field shows an exponential decay on much longer time scales of approximately 20 fs (FWHM).

The origin of the increased lifetime of the electric field is based on the lifetime of the excited state $T1$. $T1 = T2/2$ induces a loss of coherence which is implemented in the shape of the envelope $S(t)$. The increased lifetime of the electric field is not based on dispersion. Within the retrieval procedure, no sources of dispersion are involved. Dispersion effects of the ZnO itself however would result in an even longer lifetime of the electric field. The lifetime of the localized photon mode can be used to estimate the numbers of scattering events within the ZnO nano-needle array. By assuming elastic scattering within the sample, the increased lifetime of up to 20 fs corresponds to a random propagation within the needle array of approximately $6 \mu m$. The average distance between the scatterers of approximately 100 nm results in approximately 60 scattering events. In combination with the small needle diameter, the induced dispersion is weak and can be ruled out to be an explanation for the increased lifetime at the hotspot position.

The random alignment of the needles results in a large number of different scattering trajectories. Each of the trajectories has its individual resonance frequency, as explained in section 2.2.4, and therefore the corresponding photon modes show very different spectral shapes. This is another characteristic signature of localization. In order to verify this behaviour, the spectral shapes of the retrieved electric fields at the fundamental frequency are analysed and shown in figure 3.27. The change in the spectral intensity distributions $I(\lambda)$ for the different photon modes is obvious. For the case of the BBO, the retrieved spectrum $I_{BBO}(\lambda)$ is almost the spectrum of the incident laser pulse shown in the inset of figure 3.6. In contrast, the spectra of the retrieved fields for the ZnO sample $I_{inside}(\lambda)$ and $I_{outside}(\lambda)$ differ dramatically from the spectrum of the BBO measurement. Furthermore, $I_{inside}(\lambda)$ clearly shows the localized photon mode which mainly consists of the emission centered around $730 nm$, which corresponds to the excited state described by $2.2\omega_{L_0}$. $I_{outside}(\lambda)$. However, it shows additional spectral components due to the smaller value of $T1$. This change of the spectral emission is in a good agreement to the observed spectral shifts of the localized photon modes at the hotspot position and its close surrounding shown in figure 3.13.

Unfortunately the spectrum of the incident laser pulse with a central wavelength of $870 nm$ is weak in the spectral region of the localized photon mode observed at the hotspot position. Due to that, only a small fraction of the laser pulse can couple to the localized photon mode and is localized within the nano-needle array. However, absolute values of the coupling efficiency and the total emitted SH intensity are not considered within the discussed retrieval procedure of the photon modes lifetimes. Furthermore, the incoherent emission has no influence on the retrieved lifetime by using the optical Bloch equation model.

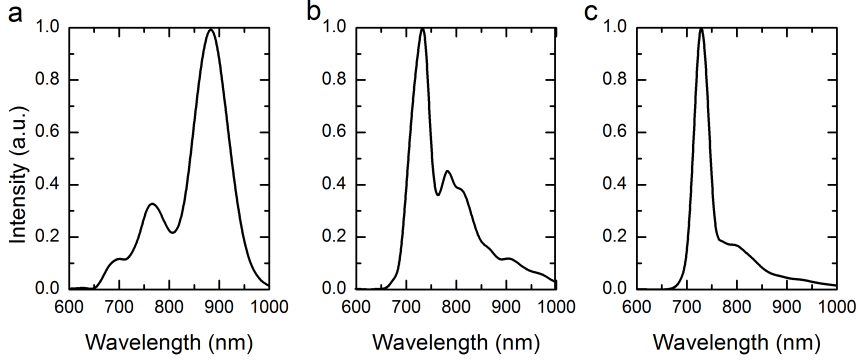


Figure 3.27: Spectral intensity distributions of the retrieved electric fields for **a** the BBO crystal with a photon mode lifetime of $T1_{BBO} = 1$ fs and a spectrum that corresponds to the Fourier-limited laser pulse, **b** the ZnO sample for a position outside of a hotspot represented by $T1_{outside} = 3.5$ fs and a red-shifted spectrum and **c** the ZnO sample for a position inside of a hotspot represented by $T1_{inside} = 6.5$ fs and a red-shifted narrowed spectrum.

This was verified by implementing a second excited state $|2\rangle$ with a spontaneous relaxation to the ground state by using simply the population of the state and a Lorentzian line shape fitting to the measured photoluminescence spectra (not shown here).

Adjacent hotspots: In order to analyse the influence of a second spatially confined emission spot within the optical resolution of the SH microscope on the measurement, the model has been expanded to a 3-level system with two excited states and a ground state. This allows simultaneous excitation of both states. Both excited states are chosen to be energetically close to each other. The resonance frequencies are set to $\omega_1 = 1.93 \cdot \omega_0$ and $\omega_2 = 2.08 \cdot \omega_0$. In order to compare the results of the simulated two adjacent modes with the measurements of the 30 nm thin ZnO nano-needle array, a lifetime of the two excited states of $T1_{beat} = 6.5$ fs is used. The resulting Fourier-transform of the IFRAC trace $\tilde{I}_{IF}(\lambda, \nu)$ is shown together with the IAC $I_{IF}(\tau)$ and the electric field $E(t)$ of the two adjacent modes in figure 3.28. The Fourier transformed IFRAC trace $\tilde{I}_{IF}(\lambda, \tau)$ shows clearly the two adjacent modes at slightly different wavelengths. The corresponding IAC slightly shows a beating at a time delay of 15 fs. Furthermore, the retrieved electric fields of the two competitive modes clearly show a beating pattern due to the constructive and destructive interference of the two modes. However, this beating pattern and the occurrence of different modes in the IFRAC traces is not observed in the experiments. Even though a hotspot is a rather rare event with a density of $0.3 \mu m^{-2}$, the case of two spatially confined localized photon modes within the optical resolution of the SH microscope, this would result in a change in the IFRAC trace and a beating pattern of the electric field due to a small shift in the Eigenfrequencies of both modes. The measured IFRAC traces only show one localized mode. This allows the conclusion, that we indeed mainly probe the emission of a single localized photon mode within the optical resolution of the SH microscope. This statement is valid as long as

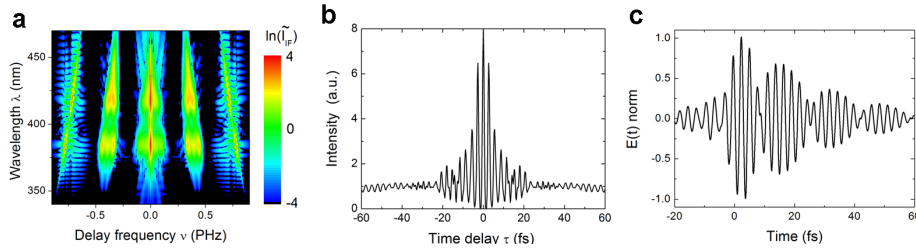


Figure 3.28: **a** Fourier transforms $\tilde{I}_{IF}(\lambda, \tau)$ of the calculated IFRAC-trace $I_{IF}(\lambda, \tau)$ on a logarithmic intensity scale calculated by using a two-photon excitation in a three-level system by an ultrashort laser pulse using optical Bloch equations. The two excited states are set to $\omega_1 = 1.93\omega_0$ and $\omega_2 = 2.08\omega_0$. **b** IAC deduced by spectral integrating the IFRAC-trace $I(\lambda, \tau)$. The IAC is showing a beating at approximately 15 fs. **c** Retrieved electric field of two adjacent modes at a dephasing time of $T2_{beat} = 13$ fs. The 2 modes are showing a clear beat in the temporal structure of the electric field due to interference.

both modes do not have identical resonance frequencies. However, this is improbable concerning the random cavities (scattering trajectories) formed within the needle array.

3.3.3 Temporal evolution of the FDTD

The temporal behaviour of the local electric field in randomly distributed cylinders was again calculated by David Leipold.

In these three-dimensional FDTD calculations, the same geometric distribution is used as for the calculation of the spatial localization. The ZnO nano-needles are represented by cylinders with varying length between 0.9 and $1\mu\text{m}$ along the z-direction in a three-dimensional distribution of the refractive index $n(\vec{r})$. The length of the cylinders is varied to avoid direct reflection of the flat caps of the cylinders. The cylinders ($n=1.96$) are embedded in vacuum ($n=1$). A section of the spatial distribution of $n(\vec{r})$ is shown in figure 3.15a. Above the cylinder array, a layer of vacuum containing the source plane of the incident laser pulse (6 fs FWHM) is added. Periodic Bloch boundary conditions in x- and y-direction (the in plane direction of the cylinder array) and strongly absorbing uniaxial perfectly matched layer (UPML) are assumed in order to avoid unwanted reflections at the boundaries [99].

Within the calculations using the FDTD method, it is possible to subtract the incident field of the laser pulse. Therefore, only the localized electric field as a function of the time can be shown. The temporal behaviour of the electric field $E(\vec{r}, t)$ can be directly taken from the FDTD calculations. Within the experiment, the SH is used to draw conclusions on the electric field at fundamental wavelength. Therefore, the experimentally deduced electric field $E_{inside}(t)$ is compared with the calculated real part of the electric field within a certain hotspot $E_{FDTD}(t)$ in figure 3.29. The temporal behaviour of the calculated electric field shows an exponential decay which fits quite well with the experimentally deduced lifetime in the hotspot of the 30 nm thin ZnO nano-needle array. However, in addition, the decay of the signal is superimposed by an oscil-

latory beating pattern. The beating pattern is known from the previous section to occur due to the constructive and destructive interference of spectrally sharp adjacent Eigenmodes. The depicted temporal structure shows an increased life-

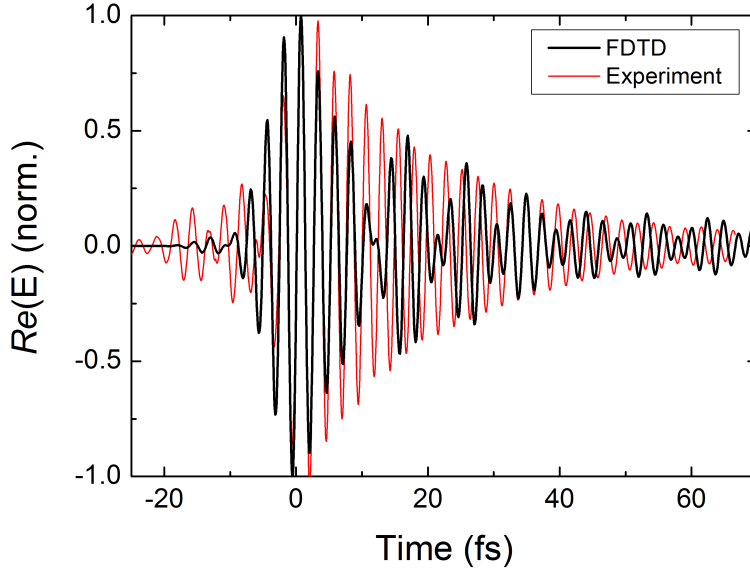


Figure 3.29: Comparison of the experimentally deduced lifetime of the real part of the electric field at a hotspot position in the 30 nm thin ZnO nano-needle array (red) with the theoretical FDTD calculation (black). The exponential decay of the electric field calculated by the FDTD fits quite good to the experimentally deduced electric field with an increased lifetime of 20 fs at FWHM. In contrast to the experiment, the FDTD calculation shows a beating pattern induced by the interference of adjacent modes.

time $E_{FDTD}(t)$ of approximately 20 fs (FWHM). Even longer lifetimes can be observed within the simulation. The strength of the pronounced beating patterns strongly depends on the spatial detection position of the electric field. To examine this behaviour in more detail, the temporal behaviour of the calculated electric field is examined for a fixed spatial position in the x- and y-direction. The temporal evolution of the electric field is now obtained for different detection positions z , i.e the direction along the vertical axis of the cylinder array. The electric field for different detection positions of $z = 0.5 \mu m$, $z = 1.0 \mu m$ and $z = 1.5 \mu m$ is shown in figure 3.30b at long times after the excitation to rule out influences of the incoming and reflected laser pulse, which is not subtracted in this case. The electric field shows strong changes as a function of the z -position above the sample. For low values of z , the beating pattern in the temporal evolution of the electric field is weak. Increasing the distance z , the beating is more pronounced as shown in figure 3.30b. The Fourier transforms along the time axis results in the spectral components which are shown as a function of the wavelength in c. For low values of z , the spectrum mainly shows a single dominant mode. When increasing the distance between the sample and

the detection point, other modes contribute to the spectrum in addition to the dominant mode. The different modes are interfering with each other resulting in the temporal beating pattern of the electric field. For a larger distance of the observation point, the number of modes increases, forming an inhomogeneous broadened ensemble of modes as indicated in figure 3.30c.

The observed beating pattern for larger distances of the detection point above the needle array is in good agreement to the calculated electric field of two adjacent modes in figure 3.28. However, such a beating pattern is not observed in the experiment. This supports the assumption, that the optical resolution is sufficient to mainly probe a single localized mode.

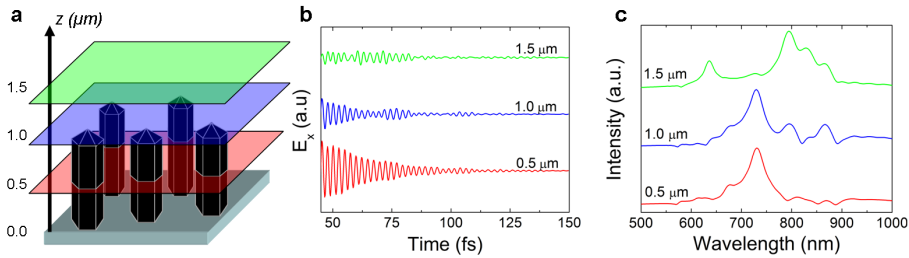


Figure 3.30: **a** The electric field from the FDTD simulation is extracted at different positions of z . **b** Temporal behaviour of the local electromagnetic field deduced by FDTD calculation showing only a weak beating pattern for low values of z and much more pronounced beating for large values of z . **c** Spectra for the different spatial distances above the sample. For low values of z one mode dominates, whereas for large values of z an ensemble of modes is observed.

3.3.4 Spatial lifetime imaging of local photon modes

A central remaining question is the connection between the local emitted SH intensity and the local electromagnetic field lifetime. Within the last section, it has been demonstrated at certain spatial positions analysing the IFRAC trace, that the lifetime of the local electromagnetic field within strongly SH active spots is increased. Furthermore, a central result of the IFRAC measurements and the retrieval procedure based on optical Bloch equations is that the local emitted SH can well be described by the dephasing time T_2 or the lifetime T_1 of the excited state in a 2-level system.

The calculated IFRAC-traces have been matched to the spectral width of the measured traces and can be used in general for the spatial imaging of local photon mode lifetimes. However, the experimental complexity of these measurements makes them rather time-consuming. Due to this, the spatial positions obtaining the local lifetime of the photon mode by using IFRAC is limited.

In order to compare the local SH emission to the local photon mode lifetime, a spatially resolved two-dimensional map of the local lifetime T_1 for a detailed statistical analysis is highly desirable. Alternatively to the measurement of an IFRAC-trace at each spatial position, the spectral emission width, which is associated to the lifetime, can be used to determine the photon mode lifetime. This requires a single localized and fully coherent photon mode. If more than two

modes are present, the temporal structure of the local electric field is strongly influenced as shown exemplary in figure 3.28.

The present experimental results and the FDTD calculations mainly indicate single localized photon modes. The experimental results (section 3.2.3) show hotspot emission confined to an area of approximately 500 nm with a contrast of two orders in magnitude. This is already an indicator of a single localized mode. Averaging over many adjacent modes would result in a spatial broadening and a more homogeneous emission map. The FDTD simulations (section 3.3.3) show a dominant mode for small distances above the needle structure. For larger distances of the detection point, pronounced beating pattern are observed due to the interference of different modes. The beating pattern is not observed within the experiment. Therefore the detected spectral width of the coherent emission is assumed to be from a single localized photon mode. In conclusion, the results of the previous sections allow to assign the emission to a single localized mode and therefore the local lifetime of the photon mode can be assigned to a spectral width.

Therefore the optical Bloch equation is solved for discrete values of the lifetime of the excited state $T1$. This results in electric fields at SH frequency $E_{SH}(t, T1)$. By using equation 3.15, the spectrum $I(\lambda, T1)$ is calculated for each electric field $E_{SH}(t, T1)$. The spectral width Δ_λ at FWHM is deduced from $I(\lambda, T1)$. This results in a clear assignment of the spectral width to the lifetime $T1(\Delta_\lambda)$. The relation $T1(\Delta_\lambda)$ for a single mode is shown in figure 3.31. This relation $T1(\Delta_\lambda)$ directly allows the determination of the local lifetime of the excited state from the emitted SH spectrum and therefore a connection to the lifetime of the local photon mode. Unfortunately the emission from the

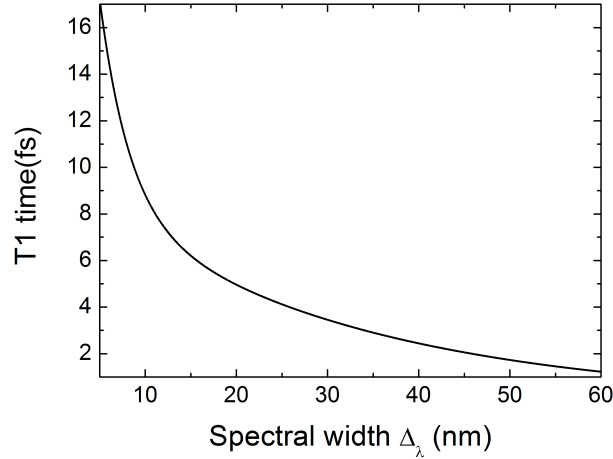


Figure 3.31: Connection between a distinct spectral width Δ_λ at FWHM and the lifetime of the photon mode $T1$ deduced by calculating optical Bloch equations for different values of $T1$.

ZnO nano-needle array is not fully coherent. The emission is influenced by two-photon induced photoluminescence from the band-gap transition in ZnO around 375 nm and some weak green photoluminescence. A solution of this problem is

explained in detail in section 2.4.1. Instead of measuring at each spatial position an IFRAC trace, the measurement was performed using a fixed time delay of approximately 240 fs between the phase-locked pulse pair. This technique allows to distinguish clearly between coherent SH emission and incoherent emission from the sample. The coherent emission shows interference fringes depending on the delay between the pulse pair whereas the incoherent emission does not show, due to its random phase, such a behaviour. This is shown in the representative local emission spectrum in figure 3.32. The pure coherent emission

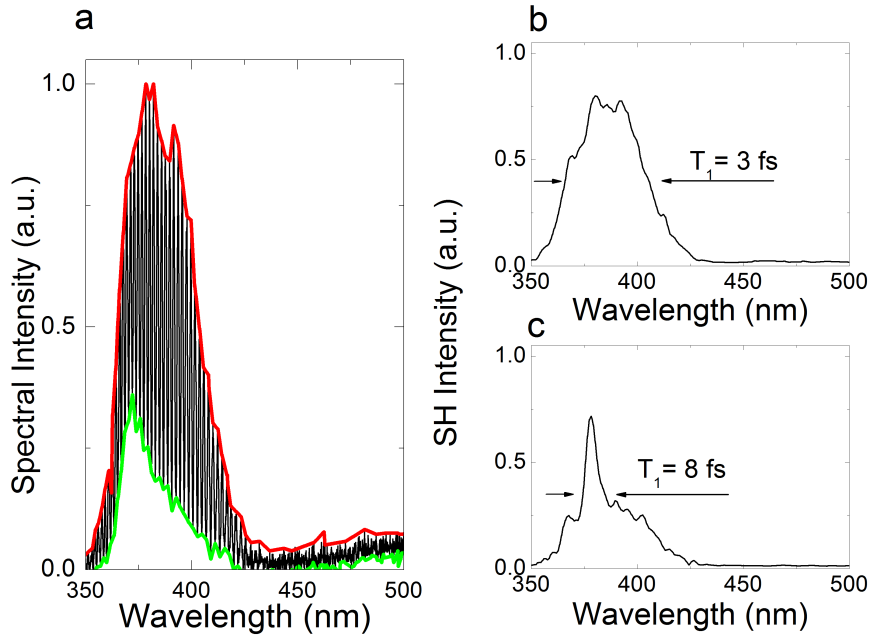


Figure 3.32: **a** Emission spectrum of ZnO illuminated by phase-locked pulse pairs at a time delay of approximately 240 fs. The coherent emission shows interference fringes whereas the incoherent emission (green line) does not show such a behaviour. **b-c** Representative coherent SH emission spectra deduced from two different sample positions by spectrally filtering the incoherent emission from the total emission. The spectral width is afterwards used to deduce the lifetime of the local photon mode. [97]

can be deduced by simply subtracting the incoherent emission (green line) by spectral filtering from the total emission of the sample (red line) as explained in 2.4.1. The resulting spectra only contains fully coherent emission and the spectral width can therefore be used to deduce the lifetime of the local photon mode neglecting dispersion. However, the dispersion is assumed to be weak due to the small number of scattering events within the photon mode lifetime and needle diameters in the sub- μm region. By raster-scanning the thin ZnO nano-needle array with a fixed time delay, maps of the emitted coherent spectral width are recorded. By considering the relation $T_1(\Delta_\lambda)$ illustrated in figure 3.31 the lifetimes of the local photon modes were deduced from the measurement.

The deduced lifetime map of $T_1(x, y)$ in combination with the local SH intensity $I_{SH}(x, y)$ is shown in figure 3.33. The deduced lifetime of the localized

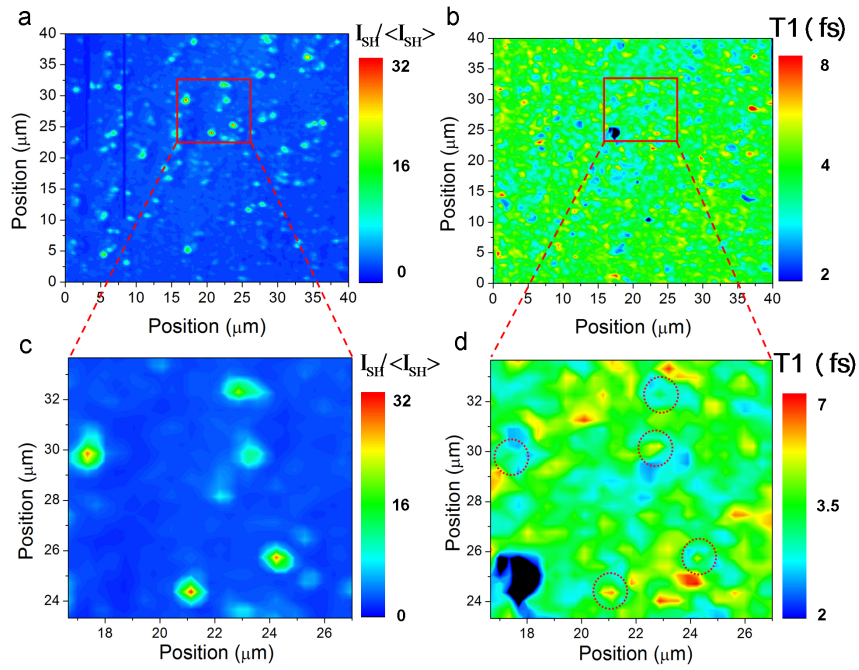


Figure 3.33: **a**Map of the spectrally integrated SH intensity I_{SH} normalized to the mean SH emission $\langle I_{SH} \rangle$ and **b** the corresponding map of lifetimes $T1$ of the local photon mode. The map of the photon mode lifetime shows fluctuations between 2 – 8 fs. The correlation between the intensity of the local SH and the lifetime is hardly visible, even in the magnified image with the red dashed circles illustrating the hotspot positions, shown in **c** and **d**, respectively.

photon modes $T1(x, y)$ shows fluctuations between 2 – 8 fs. These fluctuations also occur on spatial scales of 500 nm determined by the optical resolution of the SH microscope.

The spectrally integrated map of the SH intensity can now be compared to the lifetime of the local photon modes. Looking in more detail to the spatial intensity distribution and photon mode lifetimes in the magnified image in figure 3.33c and d, the hotspot position, indicated by the red dashed circles, does not show the largest photon mode lifetimes. Enhanced lifetimes of the photon modes can be identified at hotspot positions of up to $T1(21\ \mu\text{m}, 24.5\ \mu\text{m}) = 6.5\ \text{fs}$. However, the largest photon mode lifetimes of up to $T1(37\ \mu\text{m}, 29\ \mu\text{m}) = 8\ \text{fs}$ are deduced at a spatial position which does not show any strong SH emission. Due to the multiply scattered waves and the constructive interference, the local photon mode lifetime is expected to show an increased lifetime at the hotspot position. In most of the spatial regions, the SH intensity seems to be uncorrelated to the local photon mode lifetime. This weak connection between the strongly localized photon modes within the hotspots and the lifetimes is somehow unexpected. To further analyse this behaviour, the linear correlation coefficient of two data sets, also called Pearson's value r , is calculated [96]. The Pearson value r is calculated as follows

$$r = \frac{\sum (x_i - \bar{x})(y_i - \bar{y})}{\sqrt{\sum (x_i - \bar{x})^2} \sqrt{\sum (y_i - \bar{y})^2}} \quad (3.16)$$

and describes the correlation between x and y with \bar{x} , \bar{y} the accordant mean values. Pearson's r takes values between -1 and 1. If x and y are both increasing, the Pearson value becomes for a perfect correlation $r = 1$ (positive correlation). If x decreases as y increases, it takes a minimum value of $r = -1$ and x and y are anti-correlated. For Pearson values around zero, x and y are uncorrelated.

By calculating the correlation between the spectrally integrated SH emission and the local photon mode lifetimes, the received Pearson correlation coefficient is only $r = 0.11$. This supports the impression of the unexpectedly weak correlation between SH intensities and lifetimes. However it can be understood by taking a closer look at the measured intensity distribution of the 30 nm thin ZnO nano-needle array shown in the histogram in figure 3.18. The histogram shows two different components. One component is the Gaussian distribution centered around $I / \langle I \rangle = 1$. It describes the delocalized states, most of the intensity values belong to. The second component resembles a log-normal distribution for larger values of $I / \langle I \rangle$. This has been assigned to the localized photon modes. Therefore it is not remarkable that the correlation is weak. A correlation between strong SH intensities and enhanced lifetimes is just expected for the localized photon modes.

By restricting the calculation of the correlation coefficient to the localized photon modes that exceed a certain intensity threshold I_{th} , the correlation drastically increases. At approximately $I_{th} = 3 \cdot \langle I \rangle$ the correlation coefficient reaches a plateau as indicated by table 3.1 and figure 3.34.

The restriction of the calculation of the Pearson value to intensity values above a intensity threshold clearly shows a correlation between the local spectrally integrated SH intensity and the local photon mode lifetimes. The maximum correlation value of $r = 0.65$ at approximately $4 \cdot \langle I \rangle$ confirms the

I_{th}	residual Datapoints	Pearson value r
2· $\langle I \rangle$	465 /14641	0.31
3· $\langle I \rangle$	174 /14641	0.57
4· $\langle I \rangle$	80 /14641	0.64
5· $\langle I \rangle$	38 /14641	0.63

Table 3.1: Correlation coefficient r as a function of the threshold intensity I_{th} with the number of residual data points.

strong correlation of SH intensities and photon mode lifetimes. At 4· $\langle I \rangle$ still sufficient datapoints are left allowing this kind of statistical analysis.

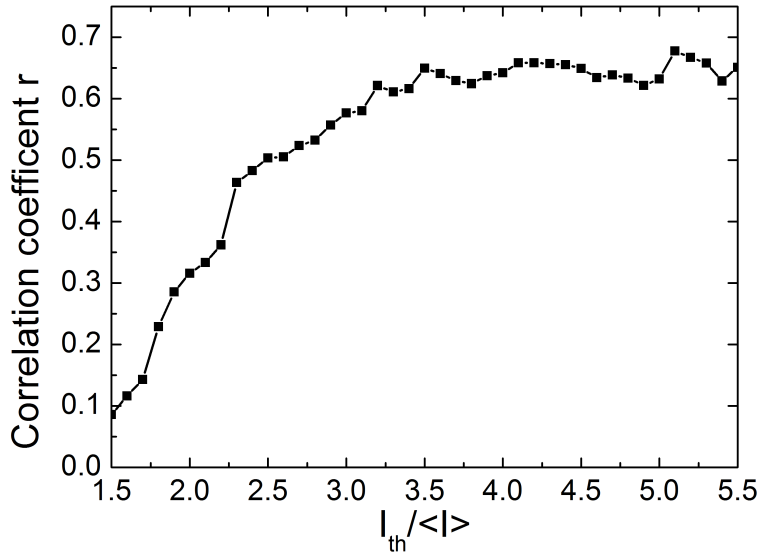


Figure 3.34: Correlation coefficient r (Pearson value) between the SH intensity and the local photon mode lifetime as a function of the SH threshold intensity I_{th} . For low threshold values the correlation is weak. The correlation drastically increases when increasing the threshold and reaches a plateau of approximately $r = 0.65$.

The physical explanation of this behaviour can not unambiguously be answered. One assumption is based on the sample characteristics. The sample is produced by MOVPE using a two temperature growth technique. This results in a bottom layer of 100 nm thick needles with the small needles on top. Localized photon modes are not observed within the array which consists only of the thick nano-needles. Localized modes have only been observed in the sample with additional 30 nm thin ZnO nano-needles on top. The investigation of the bottom layer showed only delocalized photon modes. Therefore the strong background influencing the correlation of SH intensities and photon mode lifetimes might originate in the delocalized modes from the bottom layer of thick needles.

Chapter 4

Influence of the geometric sample properties on the localization behaviour

In this chapter, the influence of the structural properties of ZnO nano-needles, i.e. the needle size and its density, on the localization of light is investigated in detail. For obvious reasons, both parameters have a major impact on the ability of the sample to store electromagnetic waves.

In the first step, we therefore studied different samples by using scanning electron microscopy (SEM). The characteristic sample properties are presented in section 4.1.

In a second step, ultra-broadband coherent SH microscopy is used to investigate the localization in the different samples. The fluctuations of the SH emission are then taken as a quantitative signature to classify the localization strength. Therefore, the statistical study of these fluctuations is compared to results based on a single parameter scaling theory. In addition, spatial correlation functions of the SH emission from the disordered ZnO nano-needle arrays are analysed (section 4.2). The experimental results are afterwards validated by a theoretical calculation based on a "dipole-dipole interaction" model (section 4.3). Finally, the experimental results are compared to FDTD simulations of the local three-dimensional electric field intensity inside the sample (section 4.4).

4.1 Sample characterization by SEM

The size of a nano-object strongly influences the optical properties [100]. In this chapter, we are especially interested in the correlation between the size of randomly arranged ZnO nano-needles and the intensity of the locally emitted SH.

In order to analyse these correlations, samples with different needle diameters and needle densities have been studied. They are characterized in terms of the geometric sample properties by using a SEM. In figure 4.1 SEM images of the investigated samples are shown. The geometric properties of such samples are deduced from the SEM images and presented in the tabular overview 4.1.

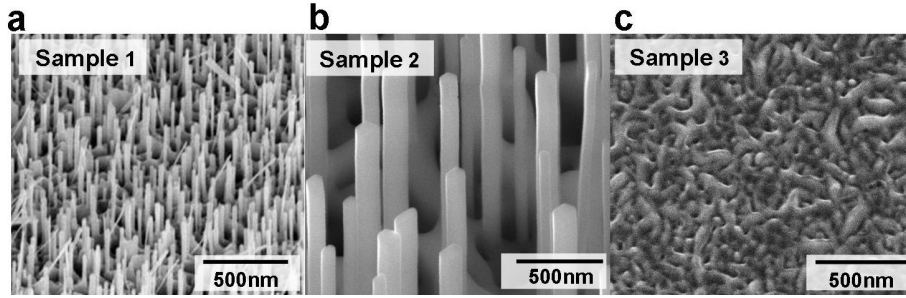


Figure 4.1: SEM images of different ZnO nano-structures taken at an angle of incidence of 52° . **a** ZnO nano-needles with an average diameter of $d_1 = 45 \text{ nm}$, a length of approximately $l_1 = 500 \text{ nm}$ and an average distance of approximately $D_1 = 100 \text{ nm}$ produced by a two-temperature MOVPE method (referred to as Sample 1). **b** ZnO nano-needles with a diameter of $d_2 = 200 \text{ nm}$, a length of approximately $l_2 = 2 \mu\text{m}$ and an average distance between the needles of about $D_2 = 1100 \text{ nm}$ produced by PVD (referred to as Sample 2). **c** Random distribution of cones. The cones are slightly overlapping. This results in average diameters and distances in the 100 nm range (referred to as Sample 3).

	diameter d	distance D	length l	density ρ
Sample 1	45 nm	100 nm	500 nm	$60 \mu\text{m}^{-2}$
Sample 2	200 nm	1100 nm	2000 nm	$1.8 \mu\text{m}^{-2}$
Sample 3	100 nm	100 nm	500 nm	$60 \mu\text{m}^{-2}$

Table 4.1: Tabular overview of the geometrical properties of the investigated samples deduced by SEM.

Sample 1, shown in figure 4.1a, is produced by using the two-temperature MOVPE growth technique [86] with a needle density of $\varrho_1 = 60\mu m^{-2}$.

The second sample in **b** shows much larger and longer needles compared to Sample 1. It has been fabricated by using a physical vapour deposition (PVD) process and consists of a homogenous distribution of ZnO needles [101]. The density has been determined to $\varrho_2 = 1.8\mu m^{-2}$.

Sample 3 is also produced by the MOVPE growth technique. However, in comparison to Sample 1, only a single temperature is used. The geometric shape of the needles is very different from that of the other samples. Therefore, the determination of the geometric properties is difficult. The structure does not consist of individual needles and can be described best by an ensemble of partially overlapping, randomly distributed cones with a diameter at the bottom of approximately 100 nm and a density of $\varrho_3 = 60\mu m^{-2}$.

4.2 Experimental results

In order to classify the localization, the following experiments are performed with the same experimental set-up (see figure 3.6) as in the previous chapter. Therefore the SH spectrum is measured as a function of the excitation position of the ultra-broadband few-cycle light pulses. The laser pulses are linearly p-polarized with an angle of incidence of 60° degree with respect to the sample normal. This ensures that a sufficiently large component of the incident electric field is polarized along the long needle axis. The SH microscope is used in combination with the interferometric autocorrelator (IA) in order to concentrate on the coherent emission from the samples as explained in detail in section 2.4.1. By keeping the time delay of the phase locked pulse pair at a fixed time delay of 120 fs , the coherent SH light from the sample shows characteristic oscillations, which are spectrally related to the time delay. At each position, the coherent emission is extracted and the complete background free signal is spectrally integrated. This results in a map of the local SH intensities. The spatial SH intensity distributions of the three investigated samples are shown in figure 4.2. The applied pulse energy of the laser was kept at only 20 pJ for all the measurements, which is well below the damage threshold.

The intensity scale for all three images was chosen to be normalized to the average SH intensity $\langle I_{SH} \rangle$. The mean SH emission $\langle I_{SH} \rangle$ from the thin ZnO nano-needles of Sample 1 is slightly weaker compared to the mean emission from Sample 2 and 3. Sample 2 and 3 show comparable emission intensities. To quantify the intensity fluctuations, the enhancement factor κ , defined by equation 3.4, is analysed for all samples. This factor is taken as a measure for the intensity fluctuations of the SH emission. The smallest value of $\kappa_3 = 3$ is determined for the ensemble of cones in Sample 3. In addition, the emission spots in this sample are extended over areas with diameters of approximately $3.5\mu m$ (FWHM). In contrast to that, the emission from Sample 2 is spatially more confined. The typical spot sizes are only 500 nm (FWHM) in diameter limited by the optical resolution of our microscope. Furthermore, the enhancement of $\kappa_2 = 5$ is bigger compared to Sample 3. However, the largest value of the enhancement $\kappa_1 = 33$ is observed for Sample 1, with emission spots spatially

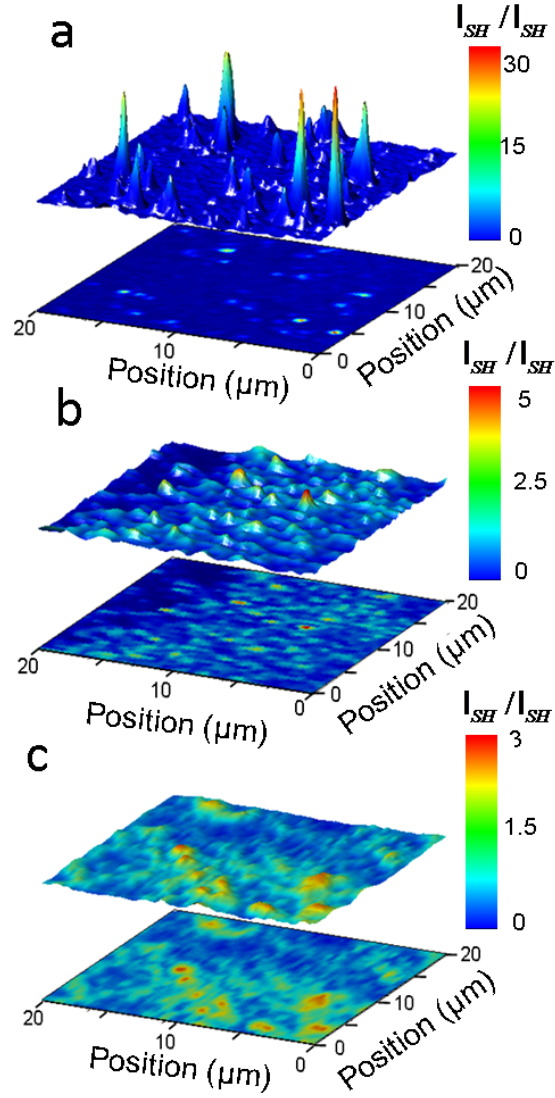


Figure 4.2: Local SH intensity map $I_{SH}(x, y)$ measured by using SH microscopy. The upper image of each sub-figure shows the color coded three-dimensional distribution of the SH, while the lower image shows the corresponding two-dimensional pattern. The height of the maxima within all images represent the overall SH intensity normalized to the individual average SH emission. However, the color code for each measurement was chosen independently. **a** Sample 1 shows the highest fluctuations of the SH intensity which results in the largest enhancement value of $\kappa = I_{SH_{max}} / \langle I_{SH} \rangle = 33$. Sample 2 and 3 show much weaker fluctuations resulting in **b** $\kappa_2 = 5$ and **c** $\kappa_3 = 3$. Sample 1 and 2 show very small emission spots with an extension of 500 nm. This spot size is limited by the microscope resolution. In Sample 3, considerably larger emission spots are observed, with an average extension of about $3.5 \mu m$.

confined to 500 nm in diameter (FWHM).

In a further step, the spatial emission characteristics are analysed by calculating the spatial autocorrelation C_S as introduced in section 3.2.3. In order to calculate C_S , a two dimensional zero-padding is applied to the spatial SH intensity maps. This allows to apply the formalism described by equation 3.5 to calculate C_S for a spatial shift along the x-axis Δx and the y-axis Δy for each of the three samples. The deduced autocorrelations C_S are shown in figure 4.3 for all samples. Each of the samples show almost the same characteristics in the

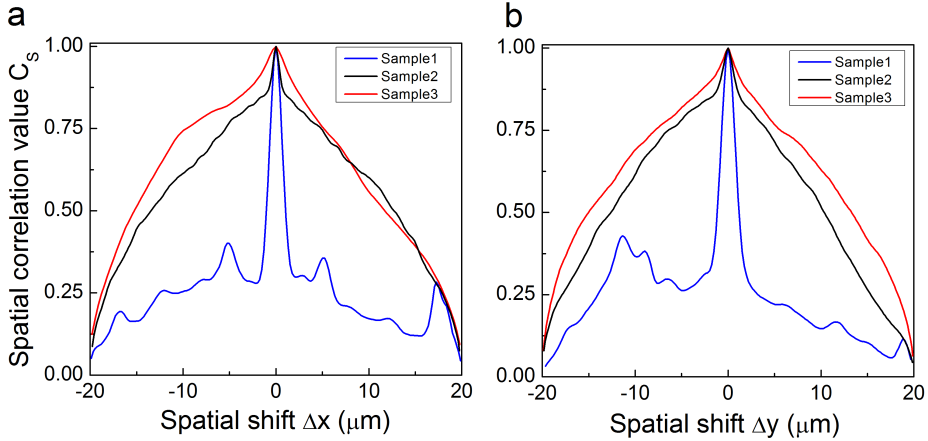


Figure 4.3: Spatial autocorrelation function C_S of the three samples as a function of the spatial shift along the x-axis in **a** and along the y-axis in **b** of the two-dimensional intensity distribution.

cases of a shift along the x- and the y-axis. Therefore the analysis of the spatial autocorrelation is reduced to the x-axis in the following. The autocorrelation function of Sample 1 clearly shows a peak at around $\Delta x = 0$ with a FWHM of $\Delta C_{S1} = 1.6 \mu\text{m}$, i.e. slightly more than twice the spatial resolution of our microscope. This behaviour indicates, that not all emission spots on the sample are confined to 500 nm. This results in a spread of C_S . There are only weak indications for longer range correlations among the emission signals indicated by the rapid decrease of C_S . From these autocorrelation plot it appears that the emission in Sample 1 stems mainly from spatially isolated hotspots with an emission size essentially given by the spatial resolution of the SH microscope.

Also Sample 2 shows a clearly resolved emission peak giving rise to a spike with a resolution-limited width in the autocorrelation function around $\Delta x = 0$. For this sample, however, the peak is superimposed on a much broader spatial autocorrelation peak with a width of about $\Delta C_{S2} \approx 25 \mu\text{m}$. This indicates that a clear isolation of the emission from a single hotspot is difficult for Sample 2. The background in the autocorrelation trace can have two different physical origins: the spatial resolution of our microscope is either not sufficient to spatially resolve the emission from isolated hotspots or the light scattering in Sample 2 results in localized modes with a typical spatial extent that is larger than the microscope resolution.

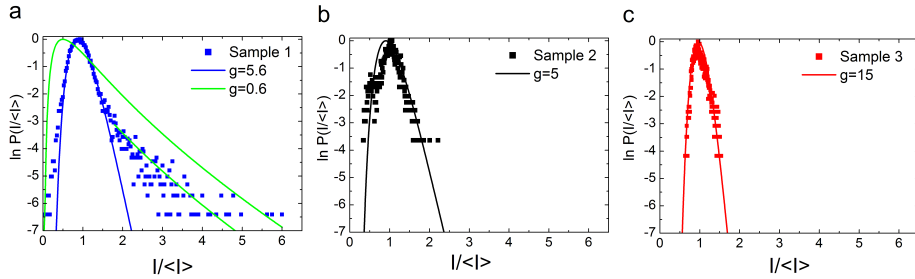


Figure 4.4: Histograms of the two-dimensional intensity distributions at fundamental frequency in combination with the distribution of the corresponding single scaling parameter g that were derived from the theory in section 2.2.5. For the reason of comparison, all three probability distributions are presented on logarithmic scale and on the same scale of $I/\langle I \rangle$. **a** Probability distribution of Sample 1. It consists of an Gaussian-distributed part described by $g = 5.6$ and a log-normal distributed part. The slope of the log-normal distributed part fits best to $g_1 = 0.6$. **b** The probability distribution of Sample 2 fits best to $g_2 = 5$. **c** The ensemble of cones in Sample 3 shows the weakest intensity fluctuations, which results in an almost Gaussian distribution and a high single scaling parameter of $g_3 = 15$.

Although, the hotspot emission in Sample 1 and 2 is confined on spatial scales of 500 nm in diameter, the shape of the spatial autocorrelation function is much broader for Sample 2. This reflects the much weaker enhancement of κ_2 compared to κ_1 . In Sample 1, the enhancement is sufficiently strong to dominate the background emission.

Finally, in Sample 3, the spatial autocorrelation maxima around $\Delta x = 0$ is essentially completely suppressed and the autocorrelation function just shows a broad background. Evidently, hotspot emission is essentially absent and mode localization due to multiple scattering is weak.

In order to gain insight into the localization properties, the experimentally determined SH fluctuations are compared to a statistical model introduced by Nieuwenhuizen et al. [63], which is described in section 2.2.5. The model is based on a single parameter scaling theory and discusses the correlation between the statistical distribution of the local field intensities in a disordered medium and the scaling parameter g . Values of $g < 1$ indicate localized photon modes, whereas $g > 1$ describes delocalized photon modes as discussed in detail in section 2.2.5. The probability distribution for a certain value of g is calculated by using equation 2.40 and the generation of an incident Gaussian wave described by equation 2.42.

The histograms at the fundamental frequency are now calculated from the two-dimensional SH intensity distributions and are shown in figure 4.4 together with the calculated distributions for the single scaling parameters g . The histograms measured for Sample 2 and 3 are quite well reproduced by the Nieuwenhuizen model when taking values of the scaling parameter of $g_2 = 5$ and $g_3 = 15$, respectively. This indicates that both samples are clearly in the weak localization regime.

The histogram measured for sample 1 is distinctly different. As already

discussed in detail in section 3.2.5, it cannot be modeled within the Nieuwenhuizen model by taking a single value for the scaling parameter. Rather, the histogram consists of a quite broad Gaussian distribution and a well pronounced exponential tail extending to an enhancement at the fundamental intensity of $I_{max}/\langle I \rangle \approx 6$. The Gaussian part of the histogram is well described by assuming a distribution with a scaling parameter of $g = 5.6$ whereas a value of $g = 0.6$ is needed to reproduce the slope of the pronounced intensity fluctuations in the exponential part of the histogram. Essentially, this indicates that the bimodal distribution provides evidence that at least some of the localized photon modes in this sample are in the strong localization regime. Their intensity fluctuations are only understood by assuming a scaling parameter that is close or below the transition from weak to strong localization. The additional Gaussian distribution indicates that not all the photon modes are strongly localized. Some contribution stems from modes that are only weakly localized, as described by the value of $g = 5.6$ needed to match the histogram.

The contribution of these weakly localized modes to the SH emission is comparatively small. Since the field intensities of the weakly localized modes at the fundamental laser wavelength are at least a factor of 3 smaller than those of the most strongly localized, their SH emission intensity is more than an order of magnitude below that of the strongly localized modes. Effectively, the weakly localized modes in Sample 1 give rise to a weak background in the SH image of Sample 1 in figure 4.2a. Clearly the SH image is dominated by the strongly localized modes.

The measurements shown above clearly indicate, that the needles with diameters of only 45 nm and an average distance of only 100 nm in Sample 1 showed the strongest evidence for light localization. The 200 nm thick nano-needles with an average distance of approximately 1100 nm in Sample 2 also showed evidence for mode localization. However, the localization strength is significantly lower. The photon modes within sample 3 are extended over several μm with a high value of g . Therefore the ensemble of cones does not give rise to pronounced mode localization.

In the following, a model is introduced in order to explain the different localization behaviour within Sample 1 and 2. This model is based on dipole-dipole interaction after excitation by a constant electric field. Sample 3 is not considered due to the deviating shape.

4.3 Dipole-dipole interaction model

The experimental results of the previous section show strongly localized photon modes within Sample 1, 45 nm thin ZnO nano-needles with an average distance of 100 nm , whereas Sample 2, 200 nm thick needles with an average distance of 1100 nm , show only weakly localized photon modes.

In order to verify these experimental observation, a simple model related to the approach of Novotny and Hecht [102] is presented, which is referred in the following as "dipole-dipole interaction" model (DDI model).

The idea of this model is the following: We assume that a single nano-needle essentially acts as a dipolar light scatterer. Its scattering efficiency is given by that of a dielectric cylinder with corresponding diameter d and length l . This scattering efficiency for a incident plane wave, described by its field amplitude

E_0 and intensity $I = \frac{1}{2}c\epsilon_0 E_0^2$ can be calculated using Mie theory. Herein, E_0 is the incident electric field. The results of this calculation then allow us to replace the cylinder by a fictitious point dipole emitter with an induced dipole moment $\vec{p}_i = \alpha_i \cdot E_0$. Here, α_i is the effective polarizability of the needle. The dipole \vec{p} acts as a source of an electric field \vec{E}_i .

When assuming N cylinders/dipoles, the dipoles do not only interact with the incident field E_0 but also with the total electric field

$$E_i^{tot}(\vec{r}_i) = E_0 + \sum_{j \neq i}^N E_j(\vec{r}_i) \quad (4.1)$$

that can be written as a sum of the incident field E_0 and the scattered electric fields from the j -th cylinder. Thus the dipolar coupling between the needles modifies the light scattering.

Effectively, this model corresponds to a discrete dipole approximation for the scattering problem [104]. Here, however, the emphasis lies on analyzing the effect of the average needle diameter and the distance. For this we focus on a discussion of the most simple case of a pair of nano-needles. In this way, the needles can be represented by dipolar scatterers with a polarizability α_1 and α_2 located at the positions \vec{r}_1 and \vec{r}_2 .

A schematic illustration of the DDI model is shown in figure 4.5. The two

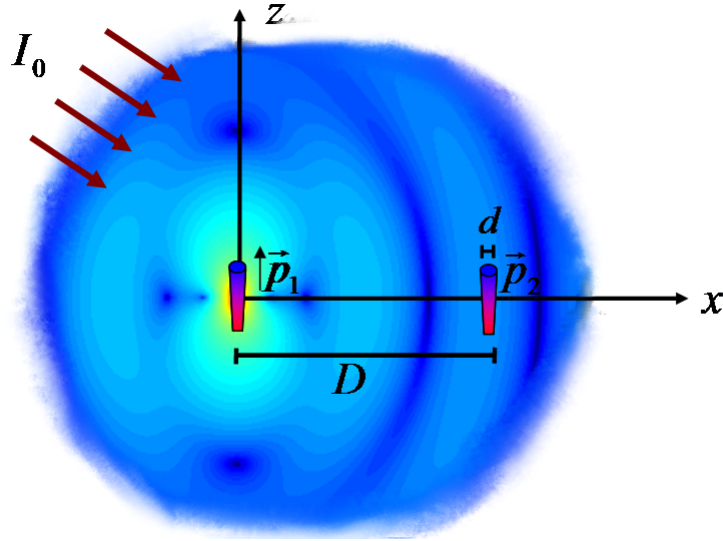


Figure 4.5: Schematic illustration of the used "dipole-dipole interaction" model of two identical cylinders. An incident electric field, described by its intensity I_0 , is scattered at the cylinders placed at \vec{r}_1 and \vec{r}_2 . The scattered incident light induces a dipole moment \vec{p}_1 and \vec{p}_2 . Therefore each cylinder acts as the source of radiation and emits an electric field E_i with a characteristic dipole pattern illustrated by the colored background of the image for \vec{E}_1 . The emitted light from the first cylinder couples to the second cylinder at a distance D . In the same way the emission of cylinder 2 can be described.

important variables are the distance D between the two cylinders and their

diameter d . The length l of the cylinders is kept constant for all different diameters and distances for the reason of simplicity. The scattering cross section C_{sca} is depending on the cylinder diameter, whereas the distance between the cylinders influences the electric field strength at the spatial position of the second cylinder.

The calculation of the scattering cross section for a cylinder is following the approach of Bohren and Huffman [108] and of van de Hulst [107], which is discussed in detail in the appendix A. The scattering cross section

$$C_{sca} = Q_{sca} \cdot G \quad (4.2)$$

is the product of the geometrical cross section G , i.e, the surface area of the scattering object perpendicular to the incident light, and the scattering efficiency factor Q_{sca} . For a cylinder, the geometrical cross section is given by $G_{cyl} = d \cdot l$. The scattering efficiency factor for a polarization along the cylinder axis can be written as [108]

$$Q_{sca} \parallel = \frac{2}{x} \left[|b_0|^2 + 2 \sum_{n=1}^{\infty} (|a_n|^2 + |b_n|^2) \right] \quad (4.3)$$

The scattering coefficients a_n and b_n are described by Bessel functions of the first J_n or second kind Y_n (also called Neumann function N_n) and the Hankel function H_n . The Hankel functions however can be written as a linear combination of Bessel functions $H_n^{(1)} = J_n + i Y_n$. The coefficients of order n

$$a_n = \frac{\left(\frac{D_n(mx)}{m} + \frac{n}{x} \right) J_n(x) - J_{n-1}(x)}{\left(\frac{D_n(mx)}{m} + \frac{n}{x} \right) H_n^{(1)}(x) - H_{n-1}^{(1)}(x)} \quad (4.4)$$

$$b_n = \frac{(D_n(mx)m + \frac{n}{x}) J_n(x) - J_{n-1}(x)}{(D_n(mx)m + \frac{n}{x}) H_n^{(1)}(x) - H_{n-1}^{(1)}(x)} \quad (4.5)$$

are calculated by using the logarithmic derivative and the recurrence relation as described in the appendix A. Herein, the value $x = k \cdot \frac{d}{2} = \frac{2\pi}{\lambda} \cdot \frac{d}{2}$ denotes the dimensionless size parameter and m the complex refractive index of the material. The refractive index of ZnO is given by $m = 1.95 + i0.0043$. The imaginary part describes the absorption and has an influence on the calculated scattering cross section.

The calculated distribution of $\frac{C_{sca}(d)}{vol}$ using cylinders of unit length l normalized to the volume $vol = \left(\frac{d}{2}\right)^2 \cdot \pi \cdot l$ is shown in figure 4.6 for a polarization along the cylinder axis. The wavelength was chosen similar to the central wavelength of the experiment to $\lambda = 870 \text{ nm}$. The calculated scattering cross section shows oscillations, which depend on the diameter of the scattering object and therefore also on the used wavelength and the refractive index. These oscillations are known as geometric resonances [108]. The values taken for the thin and thick cylinders corresponding to the experimentally deduced sample parameters and are marked by the red circle (Sample 1) and blue square (Sample 2). In case of Sample 2, a first geometric resonance slightly influences the C_{sca} value. However, the value of $\frac{C_{sca}}{vol}$ for the thick needles is at least one magnitude

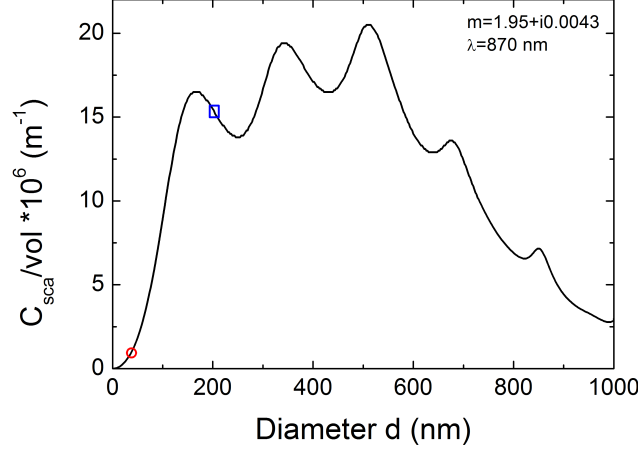


Figure 4.6: Calculated scattering cross section C_{sca} for a polarization along the cylinder axis normalized to the volume vol of a cylinder of unit length. For the calculation, a wavelength of $\lambda = 870 \text{ nm}$ and a refractive index of $m = 1.95 + i0.0043$ was chosen. The values of C_{sca} that correspond to the thin needles (Sample 1) are marked by the red circle and by the blue square for the thick needles (Sample 2).

larger compared to the value of the thin needles. Unfortunately, the asymptotic behaviour of the scattering cross section

$$\frac{C_{sca}}{vol} \sim \frac{4}{\pi \frac{d}{2}} \quad (4.6)$$

described by Bohren delivers a discrepancy by a factor of two. Nevertheless, the shape of C_{sca} is in good agreement with the literature.

In the DDI model, an incident electric field with the intensity I_0 and electric field strength E_0 is scattered by the nano-cylinders. Therefore the scattered power

$$P_d(d) = I_0 \cdot C_{sca}(d) \quad (4.7)$$

can be calculated. The radiated power P_d of a classical dipole with the scalar dipole moment p is given as

$$P_d(p) = \frac{\omega_0^4 p^2}{12\pi\epsilon_0 c^3} \quad \Rightarrow \quad p(P_d) = \sqrt{\frac{12\pi\epsilon_0 c^3 \cdot P_d}{\omega_0^4}} \quad (4.8)$$

with ω_0 being the resonance frequency of the dipole[105].

In general, the induced polarization depends on the total electric field described by equation 4.1. Assuming only two cylinders within this approach, the electric field from the second dipole at the spatial position of the first is orders of magnitude smaller than the incident electric field, i.e. $E_2(\vec{r}_1) \ll E_0$. Therefore the calculation of the induced polarization is restricted to the incident electric field

neglecting the influence of the adjacent dipole. In combination with equation 4.7, the induced dipole moment p_1 of the first cylinder is calculated as

$$p_1 = \sqrt{\frac{12\pi\epsilon_0 c^3 \cdot I_0 \cdot C_{sca1}(d)}{\omega_0^4}} \quad (4.9)$$

with a polarizability of

$$\alpha_1 = \sqrt{\frac{6\pi\epsilon_0^2 c^4 \cdot C_{sca1}(d)}{\omega_0^4}} \quad . \quad (4.10)$$

The induced dipole moment of the second cylinder is described by

$$p_2 = \sqrt{\frac{12\pi\epsilon_0 c^3 \cdot I_0 \cdot C_{sca2}(d)}{\omega_0^4}} \quad (4.11)$$

with a polarizability of

$$\alpha_2 = \sqrt{\frac{6\pi\epsilon_0^2 c^4 \cdot C_{sca2}(d)}{\omega_0^4}} \quad . \quad (4.12)$$

First, we concentrate on the description of the first cylinder. Due to the induced dipole moment $p_1 = p_{10} \cdot \delta(r_1)$ at position r_1 , the first cylinder itself acts as a dipole and therefore as a source of electromagnetic radiation.

The emitted electric field of a radiating single dipole, located at a spatial position \vec{r}_i , is described by [106]

$$\begin{aligned} \vec{E}_i(\vec{r}_i, \vec{r}_j) &= \frac{1}{4\pi\epsilon_0} \left(\left[\frac{\omega^2}{|\vec{r}_j|^2} (\vec{n} \times \vec{p}_i) \times \vec{n} \right. \right. \\ &\quad \left. \left. + [3\vec{n}(\vec{n}\vec{p}_i) - \vec{p}_i] \left(\frac{1}{|\vec{r}_j|^3} - \frac{i\omega_0}{c|\vec{r}_j|^2} \right) \right] e^{ik|\vec{r}_j|} \right) e^{i\omega_0|\vec{r}_j|/c} \quad (4.13) \\ &= g(\vec{r}_i, \vec{r}_j) \cdot \vec{p}_i \end{aligned}$$

with $\vec{n} = \frac{\vec{r}_j}{|\vec{r}_j|}$. It can be expressed by the product of the dipole moment $\vec{p}_i = \vec{p}_{i,0} \cdot \delta(\vec{r} - \vec{r}_i)$ and the transfer function $g(\vec{r}_i, \vec{r}_j)$ to any spatial observation point \vec{r}_j .

Depending on the distance from the observation point \vec{r}_j to the emitting dipole, the different contributions can be distinguished in (i) the long range far field emission described by the first part of equation 4.13, which depends on $\frac{1}{r}$, (ii) a near field contribution described by the second term, which depends on $(\frac{1}{r^3})$ and (iii) the radiation described by the term $\frac{ik}{r^2}$ which is called the intermediate field.

Within this model, the induced dipole moment at the first cylinder is assumed to be oriented along the z-axis, $\vec{p}_1 = p \cdot \vec{e}_z$. The second cylinder is placed on the x-axis at distance D , aligned as well along the z-axis. Therefore, the distance between both is described by $\vec{r} = D \cdot \vec{e}_x$. The strength of the electric field emitted from the first cylinder depends on the dipole moment p_1 and the spatial position, i.e. on the distance and angle. The chosen geometry allows

to represent the time-independent electric field $E_1 \vec{e}_z$ in the following in scalar representation. This results in

$$E_1(r_1, D) = \frac{1}{4\pi\epsilon_0} \left[\frac{k^2 p_1}{D} - 3p_1 \cdot \left(\frac{1}{D^3} - \frac{ik}{D^2} \right) \right] e^{ikD} \quad (4.14)$$

at the spatial position of the second cylinder.

To first approximation [103], the strength of the dipole coupling δ_{ij} between the two needles is then given by

$$\delta_{12} = \frac{p_2 \cdot E_1(r_1, r_2)}{\hbar} \quad (4.15)$$

and by

$$\delta_{21} = \frac{p_1 \cdot E_2(r_2, r_1)}{\hbar} \quad (4.16)$$

In the following we concentrate on δ_{12} . In the same way, the calculation can be performed by using δ_{21} . This coupling strength evidently depends on the product of the polarizabilities of the two dipole emitters and on the distance D between them.

The resulting two-dimensional distribution of the dipole coupling strength, here taken as the absolute value of δ_{12} , is shown as a function of the distance D and the cylinder-diameter d in figure 4.7.

Not all combinations of distances between the needles and their diameter are possible. Therefore the black area of δ_{12} indicates the parameter space, that is geometrically forbidden. The absolute values of δ_{12} that correspond to the different experimental conditions are marked by the red circle for Sample 1 and by the red square for Sample 2. For sufficiently small distances, the contribution of the near field dramatically dominates the electric field described by equation 4.14.

In contrast, at larger distances, the near field coupling rapidly decreases with $1/D^3$ and the electric field is dominated by the long-ranging far field that depends on $1/D$. The transition from near field to far field coupling, illustrated in figure 4.7b is also effected by the needle diameter. In a first approximation it occurs at $D > d$. The values of δ_{12} that correspond to the different experimental conditions are again marked by the red circle for Sample 1 and by the red square for Sample 2. It clearly shows that the coupling in Sample 1 is mainly achieved by near field coupling. In contrast, the average distance between adjacent cylinders in Sample 2 is too large for near field interactions. Therefore the coupling between the cylinders in Sample 2 is based on far field coupling.

In order to quantify the difference in the coupling strength, the coupling strength ratio Π_{model} is defined by

$$\Pi_{model} = \frac{|\delta_{12sample1}|}{|\delta_{12sample2}|} = 0.4 \quad (4.17)$$

Since this value is smaller than unity, the coupling between the thin cylinders is slightly weaker than for the thick cylinders. However, the values are in a comparable range which is really surprising due to the much larger scattering cross section of the thick cylinders. This result is not influenced by the deviation of the calculated scattering cross section from the its asymptotic behaviour, since

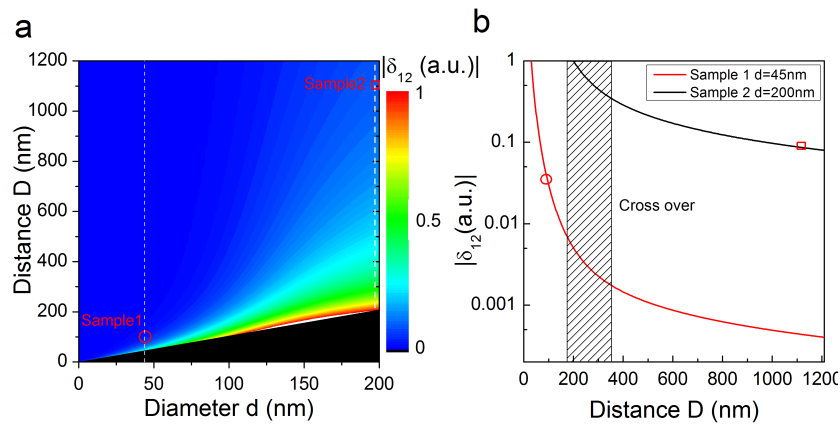


Figure 4.7: **a** Absolute value of the coupling strength δ_{12} of two adjacent cylinders calculated by using the "dipole-dipole interaction" model. The coupling strength is calculated as a function of the cylinder diameter d and the average distance D between the cylinders. The excitation wavelength was chosen to be $\lambda = 870 \text{ nm}$ and the complex refractive index $m = 1.95 + i0.0043$ was used to model the ZnO material. The corresponding coupling strength are drawn in the plot based on the geometric parameters of the samples. Therefore the red circle describes the coupling strength for Sample 1 and by the red square for Sample 2. The black area indicates the parameter space, that is geometrically forbidden. **b** Cross sections along the white dashed lines of **a** for Sample 1 (red line) and for Sample 2 (black line). The distribution of the coupling strength δ_{12} shows the transition from near-field to far-field coupling illustrated by the shaded area. The corresponding distances are marked by the red circle for Sample 1 and by the red square for Sample 2.

both values of $\delta_{12sample}$ are influenced by a factor of two.

Now the results from this easy model will be compared to the experimental findings from section 4.2. The ratio of the experimental second harmonic enhancement values κ_i of the measured intensities for thin and thick ZnO nano-needles was determined to:

$$\Pi_{exp}^{(SH)} = \frac{\kappa_1}{\kappa_2} = \frac{33}{6} = 5.5 \quad (4.18)$$

This suggests that despite their much smaller scattering cross section, the near-field coupling between the small cylinders in Sample 1 is sufficiently large to result in a comparable or even larger dipolar coupling than between the large cylinders in Sample 2.

However, for a direct comparison with the experiment, the dependence of the nonlinearity of the SH measurement $I_{SH} \propto E^4$ on the fundamental electric field E needs to be considered. This results in a ratio of

$$\Pi_{exp} = \sqrt[4]{\frac{\kappa_1}{\kappa_2}} = 1.5 \quad (4.19)$$

which is already a quite good agreement between Π_{model} and Π_{exp} , although using this simplified model of only two scattering events.

Nevertheless, multiple interaction, not only considering two cylinders, as in the DDI model, should be considered. Therefore a different approach using FDTD simulations is used in the following to verify the experimental results.

4.4 FDTD calculation

In order to analyse the coupling and the overlap of the spatial modes, a three-dimensional FDTD calculation is performed. This allows to examine the localization behaviour due to multiple scattering for Sample 1 and 2 in detail. The simulation has been performed by our collaboration partner David Leipold. Within this calculation, the ZnO nano-needles are modeled by cylinders with the refractive index $n = 1.96$ at 800 nm . The calculations are performed for two different sample structures that correspond to Sample 1 and Sample 2. The thin needles of Sample 1 are replaced by 45 nm thick cylinders with an average distance between the cylinders of 100 nm . In addition, the thick needles are modeled by cylinders with a diameter of 200 nm and a average distance of 1100 nm . For both samples, a simulation area of $5 \times 5\ \mu\text{m}$ is used.

The two-dimensional intensity distribution at the fundamental frequency are calculated by exciting the samples with ultra-short laser pulses with a pulse duration of 6 fs and a central wavelength of $\lambda = 800\text{ nm}$. A section of the calculated two-dimensional distributions $\frac{I_F}{\langle I_F \rangle}$ normalized to the average intensity $\langle I_F \rangle$ for the small and thick cylinders is shown in figure 4.8.

Due to the influence of surrounding cylinders, the spatial intensity profile is not symmetric. Obviously the thick single cylinder scatters light more strongly than the thin cylinder, as indicated by the different colour code in figure 4.8b. This behaviour is in a good agreement with the calculated scattering cross sections in the previous section. As can be further seen from the cross sections in figure 4.8c and d along the white dashed lines in the spatial intensity distributions. In the case of the thick cylinders, the intensity decrease on a spatial

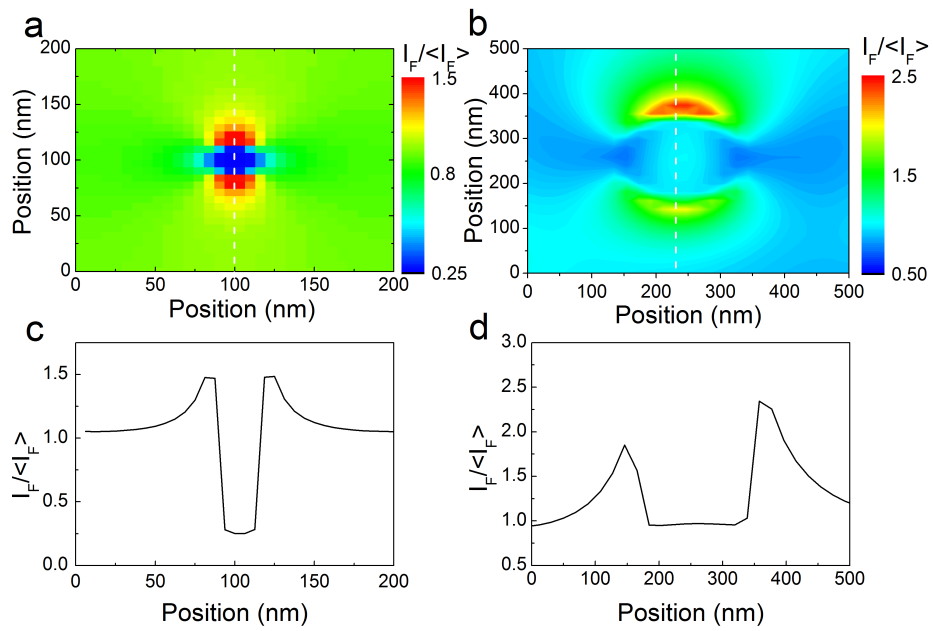


Figure 4.8: FDTD calculation of the spatial intensity distribution at the fundamental frequency $I_F / \langle I_F \rangle$ of cylinders with the refractive index of $n = 1.96$. They are excited by 6 fs laser pulse at 800 nm central wavelength. In order to match the experimental conditions, the cylinder diameters are chosen to be 45 nm in **a** and 200 nm in **b**. The cross sections along the white dashed lines in the spatial intensity distribution are shown for the 45 nm thin cylinders in **c** and for the 200 nm thick cylinders in **d**.

scale of approximately 200 nm , which is much smaller than the average distance between two adjacent cylinders. In the case of the thin cylinders, the intensity drastically decreases on a spatial scale which is comparable to the average distance of an adjacent cylinder for Sample 1. Therefore a sufficient amount of intensity is left at the spatial position of an adjacent cylinder. The average distance of 100 nm between the thin cylinders is therefore sufficient small to allow near-field coupling between adjacent cylinders.

When calculating the scattering of an ensemble of cylinders, this results in a three-dimensional intensity distribution, which is shown in figure 4.9. Here, intensity values above a threshold of $0.8 \cdot \frac{I_F}{\langle I_F \rangle}$ are shown in red. The shown intensity distribution corresponds to a time of 300 fs after the excitation with the laser pulse to ensure that the excitation pulse has left the investigation area and only localized photon modes are left within the sample. The small distance

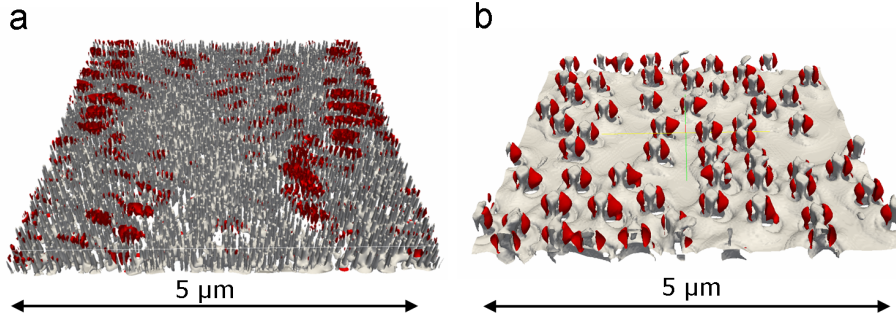


Figure 4.9: FDTD calculation at the fundamental intensity of randomly distributed cylinder arrays with the refractive index of $n = 1.96$ excited by 6 fs laser pulses at 800 nm central wavelength on an area of $5 \times 5\mu\text{m}^2$. High intensity values above a threshold of $0.8 \cdot \frac{I_F}{\langle I_F \rangle}$ are shown in red, the underlying needle structure is depicted in grey. The system parameters are chosen to match the experimental conditions. In **a** cylinders with a diameter of 45 nm and a density of $4.7\mu\text{m}^{-2}$ are calculated. For **b**, cylinders with diameters of 200 nm and a density of $1.8\mu\text{m}^{-2}$ are used.

between the thin needles allows the coupling of the local electric field to an adjacent cylinder. This behaviour forms connected local modes that involve several cylinders. The spatial mode overlap allows the wave function to propagate through the sample, which results in the interference of different scattering trajectories within the sample. At spatial positions with constructive interference of the different scattered wave functions, the local electric field is enhanced as illustrated in figure 4.9a, which results in localized photon modes. Therefore the spatial mode overlap acts as a measure of the ability to localize electromagnetic fields in terms of multiple scattered waves and interference.

In contrast, the large distance between the thick needles in combination with the strong spatial decay of the local electric field does not allow sufficient coupling to the local electric fields of adjacent cylinders. Therefore they act as single emission sources, as can be seen in figure 4.9b. High emission intensities (red) are confined to single cylinders.

The three-dimensional intensity distribution is integrated along the z -direction resulting in a two-dimensional intensity distribution at the fundamental wave-

length. In order to compare the calculated results to those obtained from the measurements, the simulated probability distribution at the fundamental intensity is shown in a histogram for the 200 nm thick and 45 nm thin cylinders (black circles) in figure 4.10. In addition, the experimental results are shown as red squares. Again the localization strength is classified by using the single scaling

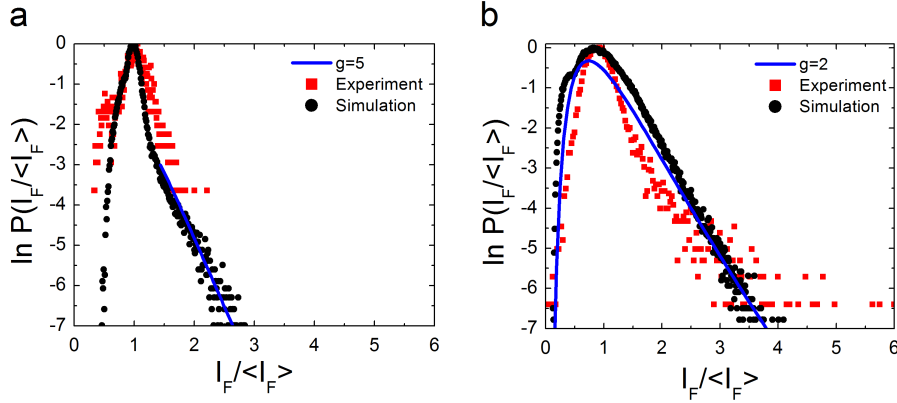


Figure 4.10: Probability distribution at the fundamental intensity of **a** the 200 nm thick cylinders (black) and ZnO nano-needles (red) and **b** for the 45 nm thin cylinders (black) and ZnO nano-needles (red). The distribution of the single scaling parameter values that fit best to the slope of the calculated simulations are shown as blue lines with $g_{200nm} = 5$ and $g_{45nm} = 2$.

parameter g . Best fitting values of g to the slope of the calculated intensity distribution results in $g_{200nm} = 5$ for the 200 nm thick cylinders. Compared to the experimental results, the simulation is slightly stronger localized as the experiment, however the shape of the histogram fits well to the experimental data. The localization strength of the 45 nm thin cylinders is classified by $g_{45nm} = 2$, which is close to the deduced localization strength of the experiment. However, the experimental intensity distribution shows a larger spread of the localized tail in the histogram.

In summary, these FDTD calculations show that the large-diameter needles in Sample 2 are mainly coupled via their far fields, whereas near-field coupling dominates in Sample 1. This enhanced near-field coupling apparently overcompensates the reduction in the scattering cross section with decreasing needle diameter and results in stronger light localization in the closely packed needle array of sample 1. This is an interesting result that suggests that highly disordered nanocrystalline materials can be very efficient in multiple light scattering and localization provided that they are sufficiently closely packed to couple via their near-fields. The results of these FDTD simulation therefore provide a convincing microscopic explanation for the surprisingly strong localization phenomena that are observed in this thesis for such small diameter dielectric nanoparticles.

Chapter 5

Electron emission from ZnO nano-needles investigated by Photo-Emission Electron Microscopy

The investigation of the spatial localization is limited by the optical resolution of the used SH microscope to approximately 500 nm . However, the numerical simulations performed by using the FDTD method show the localization to occur on spatial scales confinement to 30 nm , i.e more than one order of magnitude smaller than the optical resolution. In order to analyse this discrepancy, the localization within the thin ZnO nano-needle array is investigated by using of a photo-emission electron microscope (PEEM).

The PEEM allows to measure spatially resolved dynamics of photo-excited electrons with a resolution that firstly depends on the applied extractor voltage between the sample and the detector and secondly depends on the mode of the electric lens system guiding the electrons. However, it provides at least spatial resolutions of 40 nm [115]. This is almost the same order of magnitude as predicted by the FDTD calculations. This high spatial resolution is achieved by improved electron optics [116, 117].

Another advantage of the PEEM, in contrast to the raster scanning method of the SH microscope, is that it allows two-dimensional spatial electron emission imaging of the complete investigation area instantaneously. In combination with ultrashort laser pulse excitation, it has the potential to visualize variations of lifetimes of the local electric fields in nano-structures [113].

The following PEEM measurements concerning the electron emission from gold covered ZnO nano-needles are performed in a collaboration with the group of Prof. Dr. Aeschlimann from the TU Kaiserslautern together with Pascal Melchior.

Within the experiments, the needles act as field enhanced electron emitters, like sharp metallic tips. This technique of electron generation is currently under strong investigations, but still at an early stage of development [110]. Illu-

minated with fs-laser pulses polarized along the tip axis of the sharp gold tips, the emission is strongly confined to spatial regions of a few tens of nanometers at the end of the tip. Now, the electron emission depends on the applied laser intensity and allows multi-photon ionization (MPI) [109] and above threshold ionization (ATI) at even higher intensities [111, 112]. In the case of the gold coated ZnO nano-needles, the sample shows optical as well as plasmonic behaviour, as observed for PEEM measurements on gold coated nanostructures on indium tin oxide [114].

5.1 Gold-covered ZnO nano-needles

The uncovered ZnO nano-needles used in the previous chapters show only a very weak electron emission when illuminated directly by fs-laser pulses. Due to this behaviour, the investigated thin ZnO nano-needle array is coated with an approximately 10 nm thin film of gold¹. The investigated samples of bare thin ZnO nano-needles and the gold-coated ZnO nano-needles are characterized by scanning electron microscopy and shown in figure 5.1. The needles of the

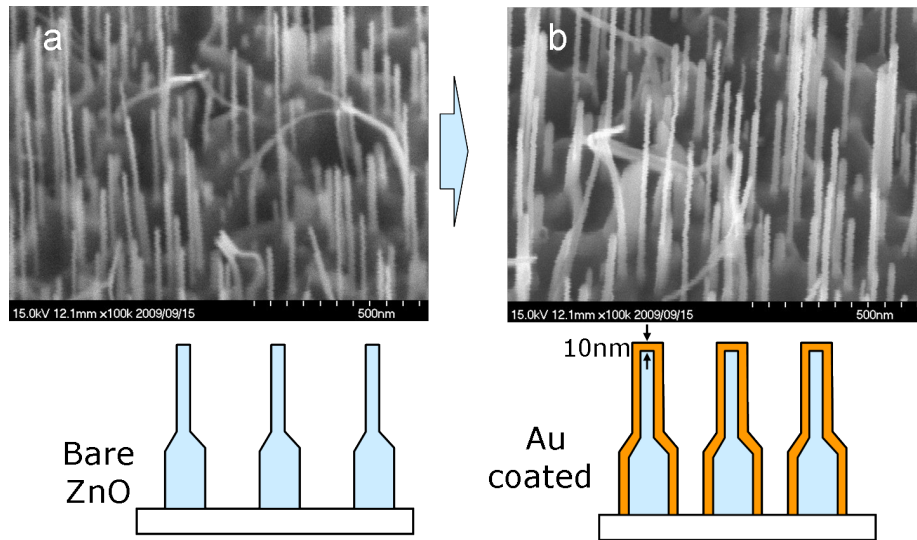


Figure 5.1: SEM images of the investigated ZnO nano-needle sample. **a** Bare ZnO nano-needle array with 20 nm thin needles. **b** ZnO nano-needles covered with a few atomic layers thin film of gold. The diameter of the needles remains even after coating in the sub 30 nm range.

uncoated sample have a diameter of approximately 20 nm. The diameter of the needles is not strongly influenced by covering them with a thin film of gold. Even after coating, the needle diameter is still in the sub-30 nm region and can therefore act as a point-like scatterer for fs-laser pulses in the infrared spectral region. The thin film of only a few atomic layers of gold still provides the sample to be almost transparent. Therefore we expect optical, as well as

¹The samples are coated by our collaboration partners at the University of Tokyo

plasmonic behaviour from the sample, i.e. multiply scattered light and localized photon modes, as well as the excitation of surface plasmon polaritons.

5.2 Experimental Set-up

The experimental set-up to measure the spatial confined emission of electrons induced by optical excitation of gold coated ZnO nano-needles is shown schematically in figure 5.2. In order to investigate the electron emission from the sample,

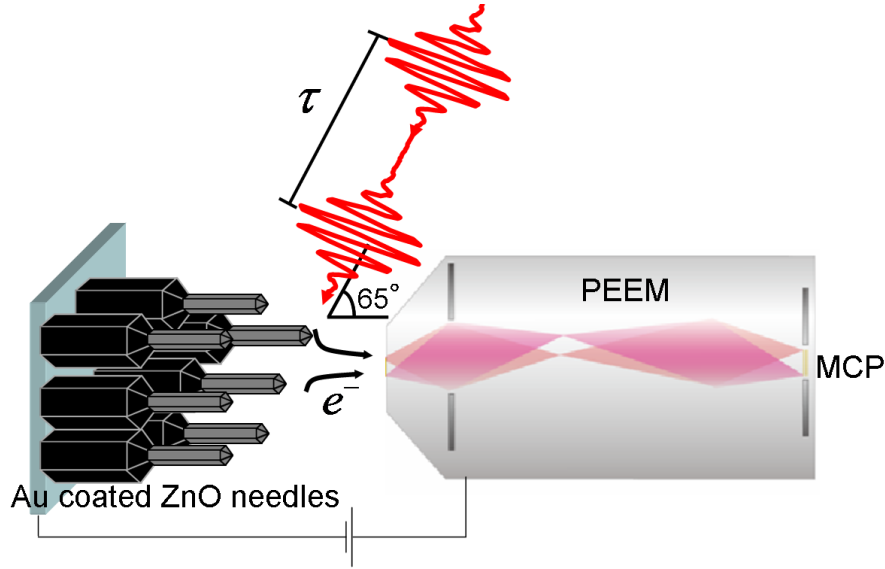


Figure 5.2: Schematic illustration of the PEEM set-up. Laser pulses with a variable delay τ are weakly focused to the investigation area of approximately $100\ \mu\text{m}$ in diameter onto the sample of ZnO nano-needles with an angle of incidence of 65° to the sample normal. The sample is placed in front of the electric lens system of the PEEM. The weak focus allows to illuminate the complete investigated area without moving the sample. Electrons emitted from the sample are collected by the strong bias voltage between the sample and the lens system and are guided towards a micro channel plate (MCP). In combination with a phosphor screen and a CCD camera the spatial electron emission is imaged.

a Ti:Sapphire oscillator (Tsunami Spectra Physics) with a pulse duration of approximately 25 fs (FWHM) and pulse energies of $5\ \text{nJ}$ working at a repetition rate of 80MHz is used to excite the sample. The spectrum of the laser is shown in figure 5.3a together with the Fourier-limited electric field structure of the pulse in b. Due to the propagation of electrons and the high operating voltage of the PEEM, the set-up is placed in a UHV vacuum chamber which is working at a pressure of approximately $10^{-10}\ \text{mbar}$. This low pressure avoids electron collisions with residual gas molecules and electric flashovers. Such a low pressure allows voltages up to $10\ \text{kV}$ with only a small gap between sample and electric lens system of the PEEM. For high voltages, it provides a spatial resolution of less than $40\ \text{nm}$ [115].

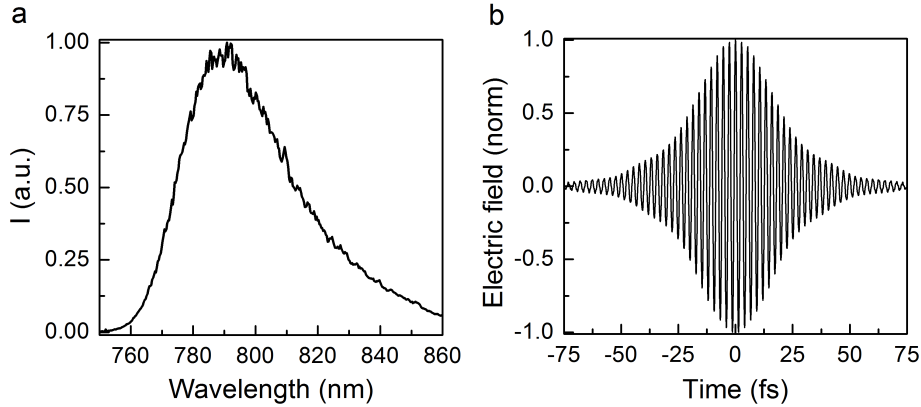


Figure 5.3: **a** Spectrum of the laser pulses from the Tsunami laser oscillator. **b** Fourier-limited electric field of the laser pulse calculated from the spectrum. The pulse duration is approximately 25 fs at FWHM.

Time-resolved measurements are possible by using the pulse pair generated in a Mach-Zehnder interferometer, stabilized by a HeNe laser [118]. By using a stabilized interferometer small fluctuations in the time delay between the laser pulses are compensated. Hence, fluctuations of the incident electric field are strongly suppressed. This is important during long accumulation times of the electron emission at a certain time delay τ .

The laser pulses are focused by a lens with a focal length of $f = 500 \text{ mm}$ onto the sample in the vacuum chamber at an angle of incidence of 65° to the normal of the sample. Therewith, the focus diameter has a diameter of approximately $100 \mu\text{m}$, providing an illumination of the complete investigation area. This allows simultaneously the excitation of different modes and a direct comparison of different spatial emission spots within the investigated area.

The electrons emitted from the sample are accelerated by the strong electric field between the sample and the outer electrode of the objective lens. Depending on the spatial emission spot, the electrons are guided by a series of electrostatic lenses that magnify the spatial emission image as illustrated in figure 5.2. At the end of the lens system, the electrons hit a micro channel plate (MCP) which consists out of thousands of μm -thick channels. An incident electron is amplified by a cascade effect within the MCP. The amplified electron signal leaves the MCP, is converted by a phosphor screen and spatially imaged by a CCD camera.

Operating the PEEM at a voltage of 8 kV , it allows spatial imaging with a resolution of less than 40 nm which is in general sufficient to measure the electron emission localized to a single needle. During the examination of the gold coated ZnO nano-needles, a smaller operating voltage was used. Therefore the resolution within the experiment is limited to approximately 50 nm .

5.3 Spatially localized electron emission

The spatial emission from the two different ZnO nano-needle arrays (bare and gold coated ZnO) is characterized in the following. Therefore, the samples are excited by 25 fs p-polarized laser pulses with a pulse energy of 0.5 nJ . In order to verify the spatial localization properties independently from the temporal behaviour, the time delay of the pulse pair is set to $\tau = 0$, i.e. both pulses are overlapping in time. Since the electron emission of the bare ZnO needles is very weak, the results of the spatial emission are only shown for the gold coated sample in the following.

The resulting two-dimensional intensity map of the local electron emission from the gold coated sample is shown in figure 5.4a. Although the size of the excited area exceeds the area observed by the PEEM, the two-dimensional intensity map shows localized hotspots of electron emission surrounded by comparatively large areas of weak emission. The cross section in figure 5.4b along the white dashed line in a shows strong spatially confined hotspots of electron emission. The deduced diameters of the hotspots are determined to approximately 300 nm (FWHM). Despite the much better resolution of the PEEM, the spatial confinement of the electron emission is almost of the same size compared to the optical experiments presented in section 3.2.3. Furthermore, compared to the prediction of the FDTD calculation in section 3.2.4, the confinement of the electron emission is one magnitude larger.

This supports, that the electron emission of a hotspot is not localized to a single needle, instead it involves many needles.

Although the gold film is only a few atomic layers, the discrepancy in the prediction of the spatial localization between FDTD calculations and the PEEM measurements raise the question if there is an influence of the gold layer on top of the needles. The spatial FDTD calculations in section 3.2.4 were performed by assuming the refractive index of bare ZnO cylinders when neglecting the gold layer on top or the bottom layer of thick needles below the thin needles. Therefore a direct comparison might be difficult.

Now the concern is focused on the local field enhancement. The enhancement of the electron emission is determined to $\eta_{e^-} = I_{e^-}^{\text{max}} / I_{e^-}^{\text{min}} \approx 580$. Since for the electron emission a four-photon process is required ($b = 4$) the fundamental field enhancement factor can be obtained by using equation 3.3 to $f_{e^-} = (E_{\text{loc}}/E_0)^{1/8} = 2.2$. However, this value is lower compared to the fundamental field enhancement deduced by the SH emission from the bare ZnO needles ($f_{SH} = 3$).

The mean enhancement is given by $\kappa_{e^-} = \frac{\text{max}(I_{e^-})}{\langle I_{e^-} \rangle} \approx 62$. When considering the high nonlinearity of the emission process, this is an unexpected low value, since the corresponding values at the fundamental of $\kappa_{e^-}^f = 2.7$ are even less compared to the value deduced for the SH measurements on the bare thin ZnO nano-needle array $\kappa_{SH}^f = 5.9$. One of the possible explanations for this behaviour is the limited 12-bit resolution of the used camera attached to the MCP in combination with the high nonlinearity of the emission process.

Furthermore, the spatial electron emission is analysed by calculating the spatial autocorrelation function C_S . In order to apply the formalism described

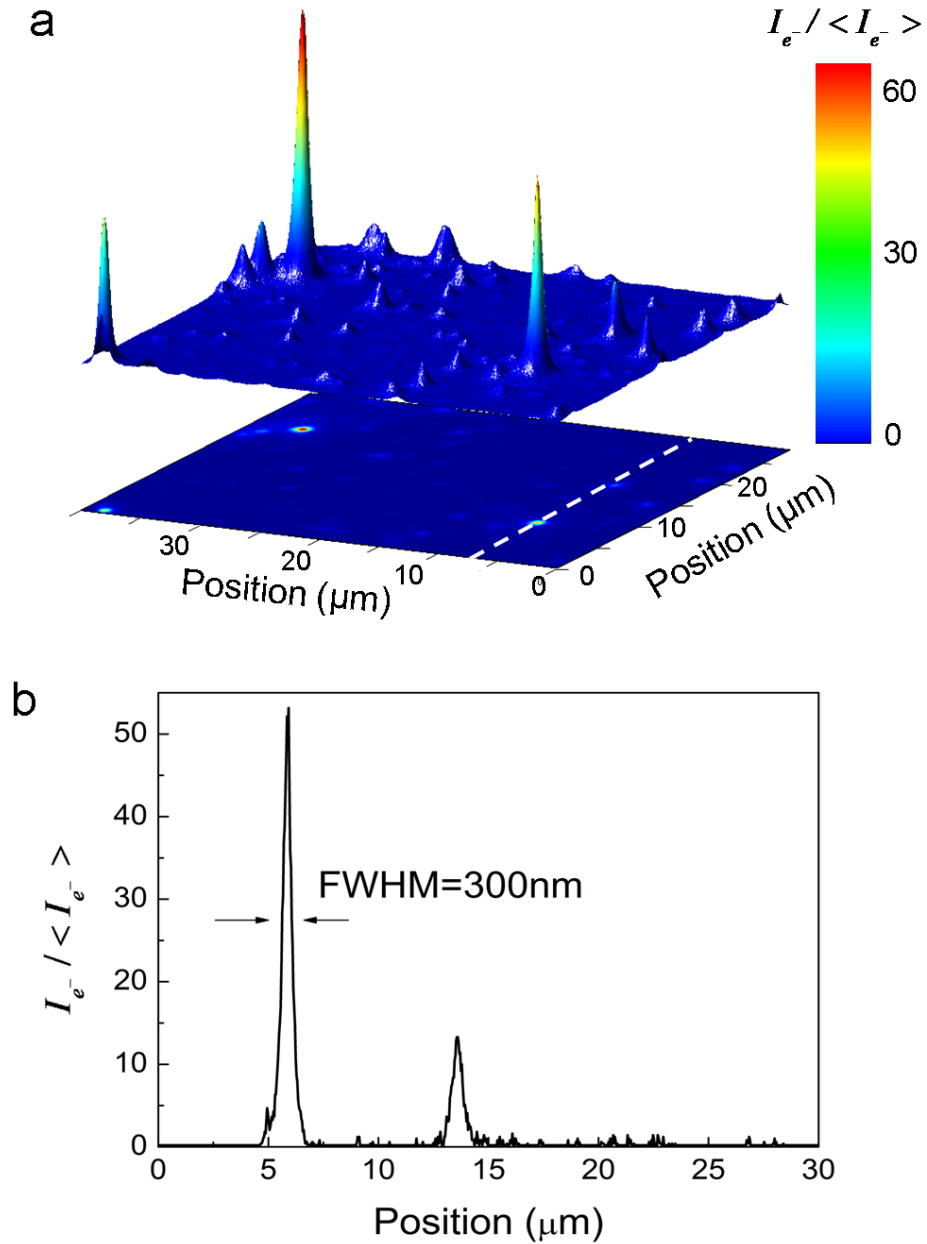


Figure 5.4: **a** Two-dimensional map of the electron emission from the gold covered ZnO nano-needle array excited with p-polarized 25 fs laser pulses with pulse energies of 0.5 nJ . The intensity of the electron emission I_{e^-} is normalized to the mean intensity $\langle I_{e^-} \rangle$. **b** Cross section of the electron emission along the white dashed line in **a** showing a hotspot diameter of approximately 300 nm (FWHM).

by equation 3.5, a two dimensional zero-padding is applied to the spatial electron emission map. The spatial autocorrelation C_S is calculated for a spatial shift along the x-axis Δx and along the y-axis Δy . The resulting spatial autocorrelation traces are shown in figure 5.5. It displays a clear maximum centered

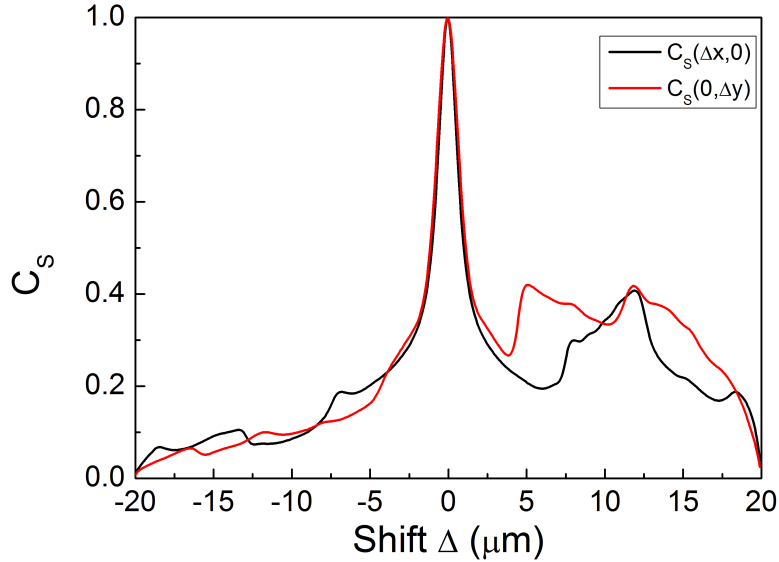


Figure 5.5: Spatial autocorrelation C_S as a function of the spatial shift along the x-axis Δx and along the y-axis Δy .

around $\Delta x = 0$ and $\Delta y = 0$. For both cases, the width of the autocorrelation peak is in the order of $\Delta C_S = 2.1 \mu m$. This value is much larger than twice the resolution of the PEEM and also much larger than twice the diameter of the hotspot deduced in figure 5.4b. This behaviour indicates, that most of the emission spots are extended over larger areas, which results in the spread of C_S . This indication is supported by the background in the autocorrelation trace. The scattered electric fields within the gold coated needle array results in localized modes with a typical spatial extent that is much larger than the resolution of the PEEM.

5.4 Single scaling parameter of the electron emission

In order to classify the localization strength of the electric field that results to the localized electron emission, the single scaling parameter g will be analysed in this section. Based on the theory derived from Nieuwenhuizen and van Rossum [63], presented in section 2.2.5, here the fundamental intensity has to be considered. The electron emission process in the gold coated ZnO nano-needle array for p-polarized incident laser light is based on a nonlinearity of $b \approx 4$. This has been proven by measuring the electron emission as a function of the excitation

power (not shown here) and is in a good agreement to values from the literature for the emission from gold tips [109, 110]. By considering the relation $I_f \propto I_{e^-}^{1/b}$, it is possible to calculate the fundamental intensity I_f from the electron emission I_{e^-} .

The histogram of the spatial localization measurements at the fundamental intensity $I_f / \langle I_f \rangle$ is calculated and shown in figure 5.6. Herein areas of low

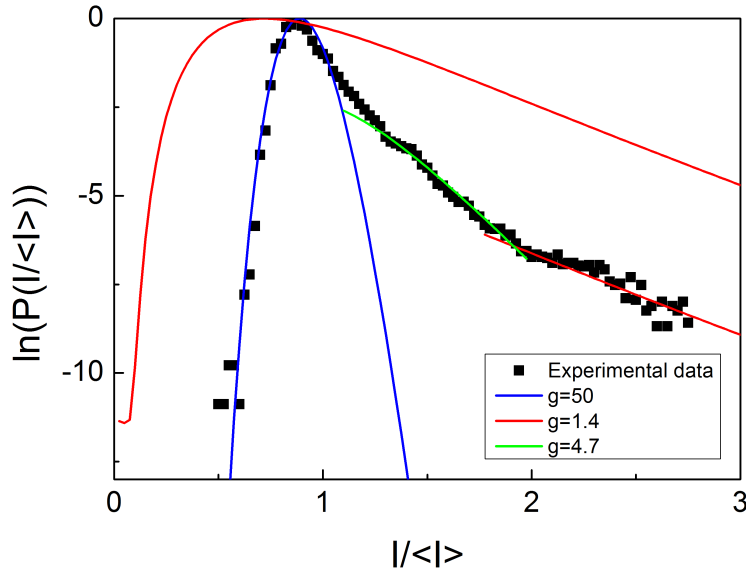


Figure 5.6: Logarithmic probability distribution of the measured electron intensity map I_f calculated from I_{e^-} of the gold covered ZnO needles. The distribution is divided into three regimes. A Gaussian distribution that describes the delocalized states below $1.2 \cdot \langle I_f \rangle$, a log-normal distribution above $1.8 \cdot \langle I_f \rangle$ for the localized states and in addition a third component is visible in the range of $1.2 \cdot \langle I_f \rangle$ and $1.8 \cdot \langle I_f \rangle$, which was not observed in all experiments on bare ZnO.

intensity are described by a distribution centered around $1 \cdot \langle I_f \rangle$. This results in a dominant Gaussian distribution as already has been observed for the optical measurements in section 3.2.3. The hotspots of strong electron emission are represented by large values of $I_f / \langle I_f \rangle$. Therefore the hotspot emission results in a deviation from the Gaussian distribution towards a log-normal distribution at values above $1.8 \cdot \langle I_f \rangle$. In between these distributions, a third distribution becomes visible. This additional component in the histogram of the gold covered ZnO needles was not observed for all optical experiments on the bare ZnO needles (figure 3.18). It can be identified by the deviation from the Gaussian distribution at approximately $1.2 \cdot \langle I_f \rangle$, as well as from the log-normal distributed part at $1.8 \cdot \langle I_f \rangle$. Therefore the few atomic layers of gold on top of the needles strongly influence the histogram and therefore as well the localization properties.

In order to classify the localization strength, the single scaling parameter g is again calculated by using an independent scaling value for each of the three different components in the histogram. The values of g that fitted best to the distribution are deduced by the least-square-method described by equation 3.6. The single scaling parameter that fitted best to the Gaussian distribution corresponds to $g \approx 50$. Therefore most of the intensity values can be addressed to the electron emission induced by delocalized electric fields.

The log-normal distribution for values above $1.8 \cdot \langle I_f \rangle$ is represented best by a single scaling parameter of $g = 1.4$. This value is close to the transition from weak to strong localization and allows the conclusion that the electric fields responsible for the hotspot emission are localized.

Finally, the distribution in between $1.2 \cdot \langle I_f \rangle$ and $1.8 \cdot \langle I_f \rangle$ is described by $g = 4.6$. This only indicates weakly localized electric fields.

A direct comparison of the localization strengths deduced by the optical SH-microscope measurements on the bare ZnO nano-needles and the electron emission from the gold covered ZnO sample shows a slightly higher localization strength for the case of the uncoated ZnO. Several influences in addition to the gold coating might be responsible for this deviation, by example the different detection using the PEEM set-up or the longer pulse duration of the excitation.

The complexity of the sample and the detection process makes an interpretation of the additional component in the histogram rather challenging. The almost transparent gold sample allows the propagation and the scattering of light waves as well as in the bare ZnO needle structure. In addition, the thin layer of gold allows plasmonic excitation leading to electron emission as recently demonstrated for gold tips [110]. Here, the authors launch electrons by optically excited surface plasmon polaritons (SPP) which localize at the end of a sharp gold tip with approximately 20 nm tip radius. Due to the high field enhancement at the end of these tips, which is also present for the gold covered ZnO nano-needle array, the SPP is able to launch an electron which might be the explanation of the third component in the histogram.

In conclusion, the determination of the single scaling parameter is a powerful tool to investigate the localization strength. Even for intensity distributions of the gold coated ZnO needles, which is a superposition of localized and delocalized electric fields, this method delivers significant results when restricting the analysis to intensity values above a certain intensity threshold.

Furthermore, this procedure is very robust due to the strong signal generated by highly spatially confined and enhanced electric fields. The alternative approach to classify the localization strength [36] by applying a multi fractal analysis to the data does not deliver trustworthy results. As described in section 3.2.6, the multifractal analysis is not suited to analyse mixed intensity distributions of localized and delocalized states.

5.5 Interferometric autocorrelation of the electron emission

In the following, we analyse the time structure of the local electric fields within the gold coated ZnO nano-needles by measuring the emitted electrons as a function of the delay time τ between the laser pulses. Since the spot size of the laser is much larger than the field of view of the PEEM, the incident electric field is assumed to be identical at each spatial position within the investigation area. Therefore each of the observed hotspots is affected identically by changes or fluctuations in the exciting electric field. A direct comparison of the recorded time traces of the emitted electrons from different spatial positions is therefore much more traceable.

Now, the electron emission at the spatial position of two hotspots is accumulated as a function of the time delay. This results in the interferometric autocorrelation (IAC) traces shown in figure 5.7.

The enhancement ζ of an IAC trace, defined by equation 3.9, strongly depends

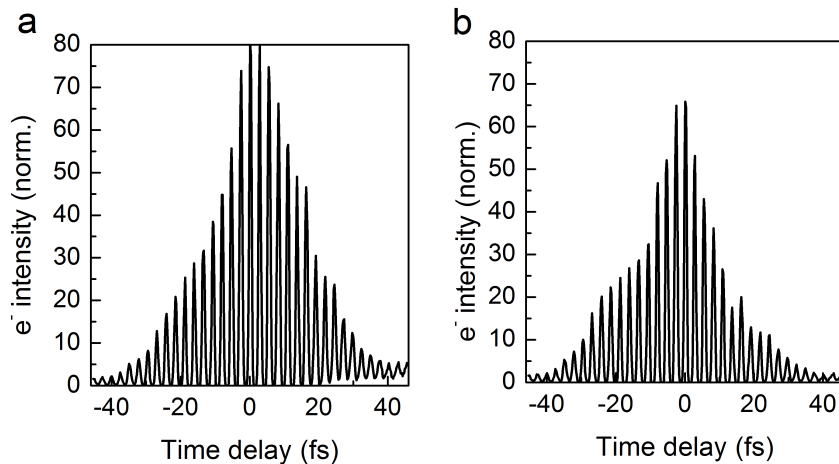


Figure 5.7: Interferometric autocorrelation traces from two different electron emission hotspots after excitation by laser pulse pairs with a pulse duration of 25 fs. Although excited by the same electric field and detected simultaneously, the IAC traces vary in shape and enhancement. This is a strong hint for different time structures of the local electric field.

on the nonlinearity b of the emission process. For the four-photon process of the electron emission, this results in a theoretical enhancement of the IAC of $\zeta = 128$. However, slight changes in the nonlinearity can lead to strong changes in the enhancement of the IAC. The minimum nonlinearity deduced from a power dependance of the electron emission from a hotspot on the gold coated ZnO nano-needle array was determined to $b = 3.5$ (not shown here). This small deviation from a four-photon process already decreases the theoretical enhancement of the IAC to $\zeta(b = 3.5) = 64$. The enhancement ζ of the recorded IAC traces with $\zeta_1 \approx 72$ and $\zeta_2 \approx 80$ is within the predicted range. Additional reasons of this deviation from the theoretical value of $\zeta = 128$ might be:

i) The influence of dispersion changes the enhancement. Due to the limited

delay time of the IACs, strong dispersion can not clearly be attributed. The expected changes due to dispersion of the 25 fs laser pulses are observable at much longer delay times compared to the measurement.

ii) The shape of the IAC traces is not symmetric which is also influencing the enhancement.

An adequate conclusion about the individual lifetime of each of these hotspots is challenging. The retrieval of the electric field from the autocorrelation requires symmetric IAC traces. Unfortunately, the non-symmetric shape of the IAC traces, prevents a direct retrieval of the local electric field within a hotspot. Nevertheless clear differences in the shape of the asymmetric IAC traces, although the excitation is identical, indicates fluctuations in the lifetime of the local electric fields within the gold covered ZnO nano-needle array. A more detailed and precise analysis recommends a laser with sub 10 fs pulse duration and a symmetric IAC trace.

Chapter 6

Random Lasing in ZnO nano-structures

In the following chapter, the localization properties of the uncoated, thin ZnO nano-needle array are investigated for higher excitation energies. This is necessary to exclude random lasing (RL) effects for the localization measurements performed in chapter 3.

In general, lasing occurs as soon as the gain within a laser resonator exceeds the losses. It is interesting to note, that one not necessarily needs a resonator for lasing. Therefore, random lasing can occur providing only coherent feedback from strong scattering [122, 123]. The scattering loop therefore acts as a random resonator. This kind of laser is called a random laser.

Localization of light in amplifying media occurs in semiconductor powders due to strong scattering and a short mean free path length. This allows sufficient coherent feedback for random lasing. Cao et al [14] reported about the observation of lasing modes above the lasing threshold in powders of zinc oxide nanoparticles. The scattering loop determines the occurring discrete laser modes. Due to the random alignment of scatterers, there is a countless number of scattering loops with different lasing modes.

Fallert et al. reported about the observation of random lasing from localized as well as from extended modes. However, the localized modes have a lower loss rate than the extended modes [28]. Especially nanostructures based on ZnO are highly suited due to their property to combine strong scattering and gain. Therefore they behave as a prototypical random lasing source as shown for ZnO nano-powders by Cao et al [14] or Fallert et al [28].

Here, random lasing within an individual needle is not possible because the size of the ZnO nano-needles is simply too small to act as a resonator itself. This is only observed for particles of dimensions larger than the wavelength [124, 125].

6.1 Power dependence at low fluence excitation

The experimental investigation of the random lasing properties is realized by measuring the optical SH emission from the thin ZnO nano-needles as a function of the input excitation fluence [J/cm^2]. Here we use again the SH microscope set-up introduced in section 3.2.1. The bare ZnO nano-needles with diameters

between 20 to 50 nm are illuminated by 6 fs laser pulses from the Ti:Sapphire oscillator. The laser pulses are focused to the diffraction limit of approximately $1\mu\text{m}$ and the SH-emission from a hotspot on the sample is spectrally resolved as a function of the applied laser fluence. The fluence is varied from $1.5\text{mJ}/\text{cm}^2$ to $7\text{mJ}/\text{cm}^2$ by means of a neutral density filter. The resulting spectral emission as a function of the applied fluence is shown on a semi-logarithmic scale in figure 6.1 between 320 and 510 nm. The spectral emission rises for different excitation

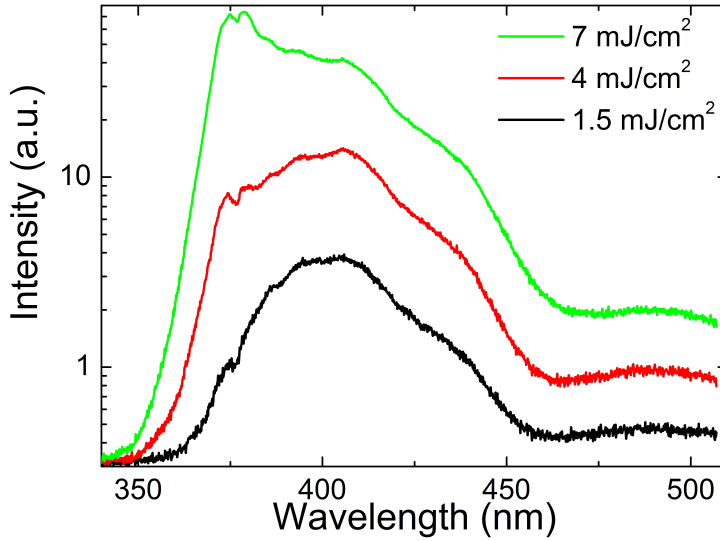


Figure 6.1: Emission spectrum for different excitation fluences on a semi-logarithmic scale. The spectrum consists of the band gap emission around 375 nm and the SH around 400 nm.

fluences and changes as well in the shape of the emission spectrum. For low excitation fluences, the SH around 400 nm is the dominant emission process. The influence of the band gap transition (BGT) around 375 nm gets dominant with increasing fluence. Integration of a small spectral region of 400–410 nm for the SH and of 370–380 nm for the BGT results in the output power dependences which is shown for both processes as a function of the fluence in figure 6.2. The deduced nonlinearity b , fitted to the respective output fluences, show very different values for the SH and BGT. The nonlinearity of the SH is estimated to be $b_{SH} = 2.1$. This fulfils the expectation of a two-photon process. The emission from the BGT however shows a much higher nonlinearity of $b_{BG} = 3.6$. By considering the laser spectrum (figure 3.6c inset), a three or even two-photon process would have been sufficient. In conclusion, the highly nonlinear emission process excites the electrons to energetically much higher states in the conduction band. By radiation-less relaxation of the electrons they reach the lowest level in the conduction band. The recombination with the hole in the valence band emits incoherent light, which corresponds to the BGT. Here, the coherence gets lost during the radiation-less relaxation process.

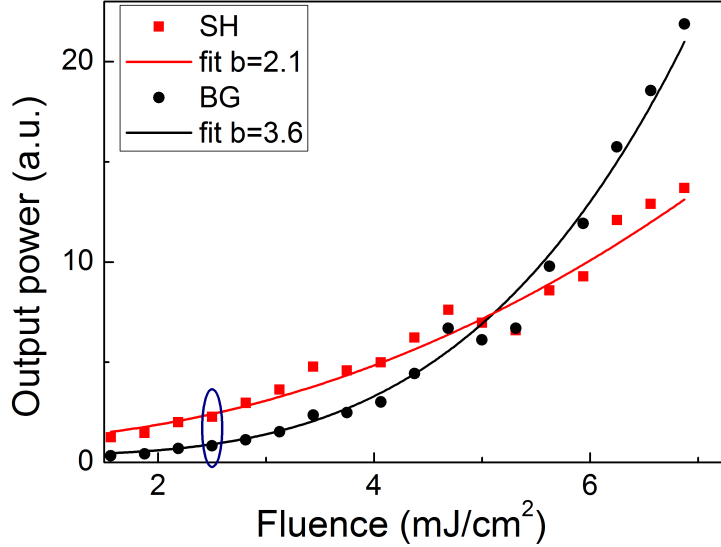


Figure 6.2: Spectrally integrated emission intensities of the SH and the BGT as a function of the input fluence. The fluence used in the localization experiment is marked by the blue ellipse.

The observed behaviour of the output power over the investigated fluence range shows only a nonlinear behavior for the SH emission, as well as for the BGT. However, no strong deviation from this behaviour is observed which would be the expectation for the random lasing threshold.

The measurements of the localization of light were performed at a fluence of approximately $F = 2.5 \text{ mJ/cm}^2$. At this fluence (blue ellipse in figure 6.2) the investigated hotspot does not show any random lasing at all.

However, even at fluences above 7 mJ/cm^2 the thin ZnO nano-needle array does not show any random lasing signatures. More than that, destruction of the filigree thin ZnO needle array occurs, which is confirmed by SEM imaging. The high repetition rate of the laser oscillator heat up the sample in a step by step process. The 12.5 ns pulse separation is not sufficient to avoid the heating process. This leads to melting of the thin ZnO needles that destroy the sample and the scattering properties.

6.2 Power dependence for high fluences: Random lasing

The verification of the random lasing process, which is known to occur in ZnO nano-structures [14, 28], is achieved by investigating the thin ZnO nano-needle array with higher fluences by using a chirped pulse amplification (CPA) system with a pulse duration of 120 fs at a repetition rate of 5 kHz (Spitfire Pro from Spectra Physics). Therewith, the applied energy is low enough to avoid ther-

mal damages of the ZnO structure due to the large pulse to pulse separation of $200\ \mu s$.

Since material dispersion is negligible for the 120 fs laser pulses, a lens with a focal length of $f = 50\text{mm}$ is used instead of the reflecting objective to illuminate an area on the sample with a diameter of approximately $300\ \mu m$. By this, we excite many scattering loops simultaneously. The spectral emission from the sample is detected as a function of the applied fluence and is shown in the inset of figure 6.3 for certain values of the fluence. In agreement with the previous measurement, the SH emission dominates at low fluences, whereas the emission from the BGT increases faster because of its higher nonlinearity. At high fluences, the emission from the BGT dominates the spectrum. For low fluences,

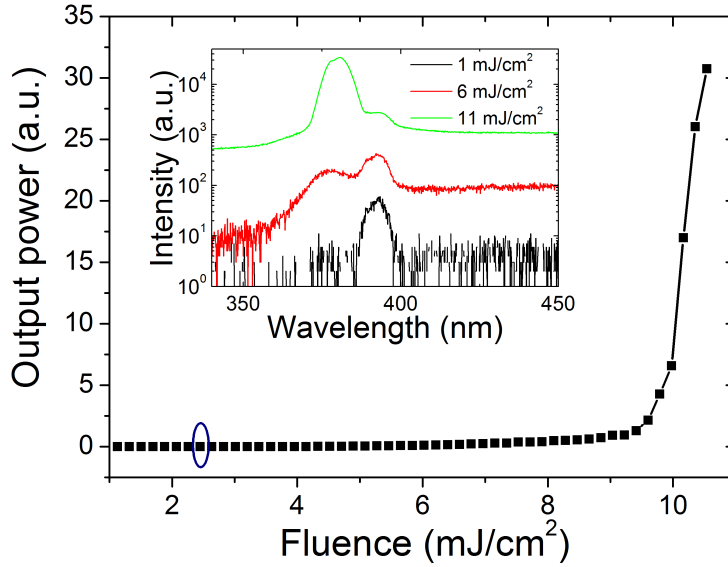


Figure 6.3: Output power of the emission integrated above the BGT at around 375 nm . The output power shows a clear deviation of the deduced nonlinearity at around 9.5 mJ/cm^2 which is a clear hint for the lasing threshold. The experiments concerning the localization behaviour are performed at a much lower fluence of 2.5 mJ/cm^2 marked by the blue ellipse. **Inset:** Emission spectra deduced from the ZnO sample at different excitation fluences plotted on a semi-logarithmic scale.

the from the previous section known nonlinear behaviour is observed for the emission of the SH and the BGT.

By increasing the fluence, the spectrally integrated emission in the range of the BGT shows a clear deviation from the nonlinear behaviour, which easily can be seen in figure 6.3. At a fluence of approximately 9.5 mJ/cm^2 the emission from the BGT dramatically increases. This deviation is known from literature and is a clear signature of the lasing threshold [126]. The experiments concerning the localization behaviour of light within the thin ZnO nano-needle array are performed at a much lower fluence of 2.5 mJ/cm^2 marked by the blue ellipse.

The random scattering trajectories (closed loops) are acting as a kind of resonator. As soon as the light propagating in the scattering loop reaches the laser threshold, the light gets amplified in the ZnO needles by stimulated emission. Therefore the ZnO needles act as scattering source and as gain medium simultaneously.

In contrast to other random lasing measurements, the observed spectral emission does not show very sharp peaks in the spectrum as observed for resonant random lasing by Cao [14]. The resonant random lasing shows sharp resonances by coupling the incident light to closed random loop cavities, which changes dramatically as a function of the excitation position, simply due to coupling to different random cavities. However, the non resonant RL shows spectrally broad lasing modes [126]. This corresponds to the measured broad lasing emission from the BGT deduced for the thin ZnO nano-needle array as can be seen from the spectra shown in the inset of figure 6.3.

In conclusion, the fluence allows the comparison of the excitation even when the pulse duration and the illumination area are totally different. The random lasing occurs at a fluence which is much larger than applied in the localization experiment. This allows to exclude the occurrence of random lasing within the spatial localization measurements in chapter 3.2.

Chapter 7

Conclusion and Outlook

Within this thesis a new approach to study the spatio-temporal dynamics of localized light in randomly arranged dielectric nanostructures is presented. This technique is based on an ultra fast second-harmonic microscope in combination with an interferometric autocorrelator. The nonlinear detection process of the SH microscope makes this technique highly sensitive to changes in local electric fields. Therefore, it is an ideal tool for investigating the localization of light at the fundamental frequency. Furthermore, the spatial resolution of the microscope is enhanced by a factor of two compared to the diffraction limit at the fundamental frequency. This allows a spatial resolution of approximately 500 nm and therefore enables the precise examination of localized photon modes. Localization of photon modes in terms of the Anderson localization requires sufficiently strong scattering. Zinc oxide is a strong scattering source due to its large refractive index of almost 2 at 800 nm . In addition, it is almost transparent over the entire visible spectrum and especially at the wavelength of the used Ti:Sapphire laser. Furthermore, the second harmonic generation is strong due to a high second order susceptibility. Therefore, the chosen samples of ZnO nano-needles are ideal candidates for multiple scattering experiments and the investigation of localization.

As it is shown within this work, the localization properties depend dramatically on the geometric properties of the sample. By using 6 fs laser pulses with a central frequency of 870 nm to excite the sample, the 100 nm thick needles did not show localized hotspots and also the spatial confinement of the increased SH regions was much larger ($3.5\text{ }\mu\text{m}$) than the optical resolution of the SH-microscope. In contrast, when illuminating a similar ZnO structure with additional 30 nm thin needles on top of the thick needles, the localization properties have been dramatically changed. This resulted in spatially confined hotspots with a diameter of 500 nm (FWHM) with intense emission at the SH frequency. The strong confinement of the emission was supported by spatial autocorrelation. The strong enhanced emission within a hotspot results in a field enhancement of the locally averaged electric field of $\eta \approx 3$. In addition to the measurements, a three-dimensional FDTD simulation has shown that the localization occurs on spatial scales of 30 nm , which is at least one order of magnitude smaller than the measured localization of the hotspots in the thin ZnO nano-needle array. The calculated enhancement is quite strong. Surprisingly, the enhancement deduced from the measurements is even larger

than the FDTD calculation when considering the different spatial resolution. Based on the SH fluctuations, the localization strength was determined by using the single scaling theory to analyse the histogram of the SH intensities. In the case of the thick ZnO nano-needle array, no localized hotspots were observed. Therefore, the determined value of the single scaling parameter g indicates that the photon modes within this sample were delocalized. In contrast, the histogram of the thin ZnO nano-needle array (30 nm thin ZnO nano-needle on top of a bottom layer of 100 nm thick needles) is a composition of a dominant Gaussian distribution and a log-normal distribution. The determined values of the single scaling parameter g indicated, that most of the photon modes were delocalized. These delocalized photon modes act as a background and could be attributed to the bottom layer of thick needles. However, the localization strength, at the spatial position of the hotspots, was determined by the single scaling theory to be at least at the transition from weak to strong localization. Although the background of the bottom layer only slightly influenced the estimated single scaling parameter, it had a dramatic influence on the classification of the localization strength by using multifractal analysis. This influence impedes the analysis of the localization strength and did not deliver trustworthy results. Therefore, multifractal analysis is not suited to determine the localization strength for mixed systems of localized and delocalized photon modes.

In addition to the spatial localization, the temporal aspects of light localization by using interferometric frequency-resolved autocorrelation were examined. This technique allows in combination with the SH microscope to deduce the photon mode lifetimes from sub- μm^2 areas with femtosecond-time resolution. To my knowledge, the presented measurements were the first attempts to investigate the temporal dynamics of localized photon modes in dielectric media.

The recorded IFRAC traces from the ZnO nano-needles at the SH were influenced by the spectral overlap with the incoherent emission from the band gap transmission and the green photoluminescence. Therefore, a direct retrieval of the local electric field from the IFRAC traces was rather challenging. However, the emission from the thin ZnO nano-needles within the IFRAC measurements clearly showed a narrowed spectral width compared to a reference measurement from a BBO crystal. The spectral width is even more decreased for a position within a hotspot.

Nevertheless, in order to deduce the local photon mode lifetime, a model based on optical Bloch equations was used. The corresponding equations for a two-level system were solved by assuming a two-photon excitation. The resonance frequency and the dephasing time of the system had been the only free parameters that matched the experimental results. The retrieval of the local electric field at the fundamental frequency for the BBO measurement, which was used as a reference, showed an almost bandwidth-limited laser pulse of 6.5 fs (FWHM). In contrast, the retrieved electromagnetic field of the ZnO nano-needle array showed an increased lifetime which persists within a hotspot for approximately 20 fs (FWHM).

Instead of measuring an IFRAC trace at each spatial position to receive a map of local electric field lifetimes, the spectral width of the SH was used as an indicator for the photon mode lifetime. The spectral width was calculated by the use of the optical Bloch equations as a function of the lifetime of the ex-

cited state, i.e. $T1$. This allowed to assign the experimentally deduced coherent spectral width to the lifetime of the excited state, i.e. to the photon mode lifetime. Therefore, the coherent part of the emission from the ZnO sample had to be extracted. The IFRAC set-up allowed the distinction between coherent and incoherent emission from the sample by using two, temporally separated, laser pulses at a fixed time delay. Finally, this resulted in pure coherent emission, which allowed to deduce a two-dimensional map of the lifetime of the local electric field. The results indicated a weak correlation between the two-dimensional map of local electric field lifetimes and the two-dimensional map of the intensity at the SH. The correlation between these two distributions increased dramatically by restricting the correlation to localized states above a certain intensity threshold.

Additional calculations by FDTD simulations of the lifetime of the local photon mode showed excellent agreement with the experimental results. However, there was a beating of two adjacent photon modes which depends strongly on the distance of the observation point within the simulation. The beating vanished for small distances and one dominant photon mode could be observed. This beating of two adjacent modes would clearly be visible in the IFRAC-trace but was not observed within the experimental results. Therefore, the resolution of the SH microscope was sufficient to mainly probe a single localized photon mode.

In the next step, the influence of the geometric sample properties, i.e. the diameter of the needles and the average distance between adjacent needles, on the localization was investigated. To achieve this 45 nm thin ZnO nano-needles with an average distance of 100 nm were compared in terms of localization strength, based on the single scaling theory, with 200 nm thick needles that have an average distance of 1100 nm. In both cases, the localized hotspots were spatially confined to areas limited by the optical resolution. Surprisingly, the thin needles showed the strongest localized photon modes.

The experimental results were compared to the calculation based on a "dipole-dipole interaction" model. This model considers the influence of the scattering at cylinders as a function of the diameter and the decrease of the electric field as a function of the propagation distance to a second, identical cylinder. It indicated a comparable coupling strength for both cases. This result is rather surprising due to the much stronger light scattering at the thick needles. However, the stronger scattering is nearly compensated by the occurring near-field coupling between the thin needles. In contrast, the large distance between the thick needles and the strong spatially decreasing electric field only allows far-field coupling. Hence, the thick needles act as single emission sources which is also supported by the FDTD calculations. The small distance between the thin needles in the FDTD simulation also supports near-field coupling between the local electric fields of adjacent needles, forming overlapping local modes over spatial regions involving several needles. This again results in enhanced local electric fields.

Measurements with increased spatial resolution of approximately 50 nm were performed on gold coated ZnO nano-needles by using a photo-emission electron microscope (PEEM). The gold coated needles were illuminated by 25 fs laser pulses with a central wavelength of 800 nm. This resulted in localized hotspots of electron emission. These hotspots had a diameter of 300 nm (FWHM), which

was less than deduced optically by the SH microscope (500 nm) on the bare ZnO needles, but much larger than the FDTD calculations (30 nm). Therefore, the electron emission was not confined to a single needle.

The localization strength of the light at the fundamental frequency was not as strong within the gold covered ZnO nano-needles as in the bare ZnO needles. One explanation for this difference might be an observed additional component in the histogram between the localized and delocalized modes. This additional component was not observed for the uncoated ZnO needle array and might be attributed to the plasmonic behaviour induced by the thin film of gold on top of the ZnO needles.

The lifetime measurements of the local electric fields from different hotspots clearly showed different interferometric autocorrelation (IAC) traces. Unfortunately they were not symmetric making the retrieval of the time structure challenging and not trustworthy. Nevertheless, the IAC traces already indicated different lifetimes of the local electric fields.

Finally, the random lasing properties of the thin ZnO nano-needles were investigated. In the case of 6 fs laser pulses from a Ti:Sapphire oscillator with a repetition rate of 80 MHz, random lasing was not observed within a hotspot up to a fluence of 7 mJ/cm^2 . Rather destruction of the sophisticated sample occurred at these fluence values. The use of a chirped pulse amplification (CPA) system with 120 fs laser pulses at a repetition rate of only 5 kHz allowed much higher fluences. Random lasing from the band gap transition in ZnO occurred at around 9 mJ/cm^2 identified by the typical lasing threshold behaviour. However, the localization measurements were performed on a much lower fluence of approximately 2 mJ/cm^2 . This ruled out the influence of random lasing in the localization measurement.

Outlook

The successful use of ultra-broadband SH microscopy in combination with femto-second time resolution to investigate localization in two-dimensional dielectric media opens a wide range of further applications. One of the most promising applications for this method is the investigation of localization in three-dimensional samples or bulk materials [127].

Another possible application is the structured surface of solar cells. The ZnO material is transparent and multiple scattering within the needle array increases the lifetime of the electric field within the structure. The coupling efficiency of the solar cell could be enhanced if the light persisted longer in the array to generate electric current [32].

Bibliography

- [1] P.W. Anderson: *Absence of Diffusion in Certain Random Lattices*. Phys Rev. 109, 1492 , (1958)
- [2] A. Lagendijk, B. van Tiggelen and D.S. Wiersma: *50 years of Anderson localization*. Physics Today 62(8), 24-29, (2009)
- [3] D. Belitz and T.R. Kirkpatrick: *The Anderson-Mott transition*. Rev. Mod. Phys. 66, 261 - 380, (1994)
- [4] I. Amanatidis, I. Kleftogiannis, F. Falceto and V.A. Gopar: *Conductance of one-dimensional quantum wires with anomalous electron wavefunction localization*. Phys. Rev. B. 85, 235450, (2012)
- [5] D. S. Wiersma, P. Bartolini, A. Lagendijk and R. Righin: *Localization of light in a disordered medium*. Nature 390, 671-673, (1997)
- [6] J.H. Lambert: *Photometry, or, On the measure and gradations of light, colors, and shade*. ("Augusta Vindelicorum") Eberhardt Klett ,p. 391, (1760)
- [7] A. Ioffe and A.R. Regel: *Non-crysataline, amorphous, and liquid electronic semiconductors*. Prog. Semicond. 4 237, (1960)
- [8] S. John: *Electromagnetic Absorption in a Disordered Medium near a Photon Mobility Edge*. Phys. Rev. Lett. 53, 2169-2172 (1984)
- [9] P.W. Anderson: *The question of classical localization: A theory of white paint?*. Philos Mag B Vol 52, No 3, 505-509 (1985)
- [10] H. Hu, A. Strybulevych, J.H. Page, S.E. Skipetrov and B.A. van Tiggelen: *Localization of ultrasound in a tree-dimensional network*. Nature physics, Vol 4 945-948, (2008)
- [11] S. Grillon, L. Aigouy, A. C. Boccara, J. C. Rivoal, X. Quelin, C. Desmarest, P. Gadenne, V. A. Shubin, A. K. Sarychev and V. M. Shalaev: *Experimental Observation of Localized Optical Excitations in Random Metal-Dielectric Films*. Phys. Rev. Lett. 82, 4520-4523 (1999).
- [12] L. Sapienza, H. Thyrestrup, S. Stobbe, P.D. Garcia, S.Smolka and P. Lodah : *Cavity Quantum Electrodynamics with Anderson-Localized Modes*. Science 327, 1352-1355 (2010)

- [13] T. Schwartz, G. Bartal, S. Fishman and M. Segev: *Transport and Anderson localization in disordered two-dimensional photonic lattices*. Nature 446, 52-55 (2007)
- [14] H. Cao, Y. G. Zhao, S.T. Ho, E.W. Seelig, Q.H. Wang and R.P.H. Chang: *Random Laser Action in Semiconductor Powder*. Phys. Rev. Lett. 82, 2278 (1999)
- [15] J. Wang and A.Z. Genack: *Transport through modes in random media*. Nature 471, 345- 348 (2011)
- [16] P. F. Moulton: *Spectroscopic and laser characteristics of Ti : Al₂O₃*. JOSA B, Vol. 3, Issue 1, pp. 125-133 (1986)
- [17] N.F. Mott: *Electrons in disordered structures*. Adv. Phys. 16, 49 (1967)
- [18] M. van Albada and A. Lagendijk: *Observation of Weak Localization of Light in a Random Medium*. Phys. Rev. Lett. 55, 2692-2695, (1985)
- [19] G. Maret and P. Wolf: *Weak Localization and Coherent Backscattering of Photons in Disordered Media*. Phys. Rev. Lett. 55, 2696-2699, (1985)
- [20] S. John: *Strong localization of photons in certain disordered dielectric superlattices*. Phys. Rev. Lett. 58, 2486-2489 (1987).
- [21] C. Conti and A. Fratalocchi: *Dynamic light diffusion, three-dimensional Anderson localization and lasing in inverted opals*. Nat Phys 4, 794-798 (2008).
- [22] C. Caer, X. Le Roux, and E. Cassan: *Enhanced localization of light in slow wave slot photonic crystal waveguides*. Opt. Lett. 37, 3660-3662 (2012).
- [23] M.I. Stockman, D.J. Bergman, C. Anceau, S. Brasselet and J. Zyss: *Enhanced Second-Harmonic Generation by Metal Surfaces with Nanoscale Roughness Nanoscale Dephasing, Depolarization, and Correlations*. Phys. Rev. Lett. 92, 057402 (2004).
- [24] S.I. Bozhevolnyi, J. Beermann, and V. Coello: *Direct Observation of Localized Second-Harmonic Enhancement in Random Metal Nanostructures*. Phys. Rev. Lett. 90, 197403 (2003).
- [25] C. Anceau, S. Brasselet, J. Zyss, and P. Gadenne: *Local second-harmonic generation enhancement on gold nanostructures probed by two-photon microscopy*. Opt. Lett. 28, 713-715 (2003).
- [26] H. Cao, J.Y. Xu, D.Z. Zhang, S.-H. Chang, S.T. Ho, E.W. Seelig, X. Liu, and R.P.H. Chang : *Spatial Confinement of Laser Light in Active Random Media*. Phys. Rev. Lett. 84, 55845587, (2000)
- [27] M. Stockman: *Femtosecond Optical Responses of Disordered Clusters, Composites, and Rough Surfaces: The Ninth Wave Effect*. Phys. Rev. Lett. 84, 1011 (2000)

- [28] J. Fallert, R. J. B. Dietz, J. Sartor, D. Schneider, C. Klingshirn, and H. Kalt: *Coexistence of strongly and weakly localized random laser modes* Nature Phot. 3, 279 (2009)
- [29] S. Nie and S. R. Emory: *Probing Single Molecules and Single Nanoparticles by Surface-Enhanced Raman Scattering* Science 275, 1102 (1997)
- [30] J. Steidtner and B. Pettinger: *Tip-Enhanced Raman Spectroscopy and Microscopy on Single Dye Molecules with 15 nm Resolution*. Phys. Rev. Lett. 100, 236101 (2008)
- [31] C. Rockstuhl, F. Lederer, K. Bittkau, T. Beckers, and R. Carius: *The impact of intermediate reflectors on light absorption in tandem solar cells with randomly textured surfaces*. Appl. Phys. Lett. 94, 211101-211103 (2009).
- [32] C. Rockstuhl, F. Lederer, K. Bittkau and R. Carius: *Light localization at randomly textured surfaces for solar-cell applications*. Appl. Phys. Lett. 91, 171104 (2007)
- [33] D. S. Wiersma: *Disordered photonics*. Nature Photonics 7, 188196 (2013)
- [34] P. Carpena, P. Bernaola-Galvan, P.C. Ivanov and H.E. Stanley: *Metal-insulator transition in chains with correlated disorder*. Nature 418, 955-959 (2002)
- [35] J. Billy, V. Josse, Z. Zuo, A. Bernard, B. Hambrecht, P. Lugan, D. Clément, L. Sanchez-Palencia, P. Bouyer and A. Aspect: *Direct observation of Anderson localization of matter waves in a controlled disorder*. Nature 453, 891-894 (2008)
- [36] Anthony Richardella, Pedram Roushan, Shawn Mack, Brian Zhou, David A. Huse, David D. Awschalom, Ali Yazdani: *Visualizing Critical Correlations near the Metal-Insulator Transition in $Ga_{1-x}Mn_xAs$* . Science Vol. 327, 665 (2010)
- [37] H.F. Hess, E. Betzig, T.D. Harris, L.N. Pfeiffer, K.W. West: *Near-Field Spectroscopy of the Quantum Constituents of a Luminescent System*. Science Vol. 264 no. 5166 pp. 1740-1745 (1994)
- [38] F. Intonti, V. Emiliani, C. Lienau, T. Elsaesser, V. Savona, E. Runge, R. Zimmermann, R. Ntzel and K.H. Ploog: *Quantum Mechanical Repulsion of Exciton Levels in a Disordered Quantum Well*. Phys. Rev. Lett. 87, 076801 (2001)
- [39] K. Takayanagi, Y. Kondo, H. Ohnishi: *Suspended gold nanowires: ballistic transport of electrons*. JSAP international - jsap.or.jp, (2001)
- [40] D. Vollhard and P. Wölfle : *Self-consistent Theory of Anderson Localization*. Elsevier Science Publishers B.V (1992)
- [41] C. Stellbach: *Anderson-Lokalisierung und Hochfrequenzinduzierte Polarisation von ultrakalten Neutronen*. Inaugural Dissertation Ruprecht-Karls-Universitt (1998)

- [42] U. Tritthart: *Wasserstoffdotierte WO_3 -Filme. Elektrische Transporteigenschaften-Metall Isolator Übergang.* Dissertation TU Caolo-Wilhelmina zu Braunschweig (1999)
- [43] H. Schomerus: *Transmission delay times of localized waves.* Phys. Rev. E, Vol 64, 026606 (2001)
- [44] P. Sheng: *Introduction to Wave Scattering, Localization and Mesoscopic Phenomena.* Springer, 2nd edition (2006)
- [45] D. Vollhardt: *Der Metall-Isolator bergang in Ungeordneten Systemen.* Unordnungsphnomene in Festkrpern 16. Ferienkurs der KFA Jlich, page. 261 (1985),
- [46] R. P. Feynman and A. R. Hibbs: *Quantum mechanics and path integrals.* International series in pure and applied physics, McGraw-Hill, New York, (1965)
- [47] N.F. Mott: *Metal-insulator transitions.* London: Taylor and Francis (1990)
- [48] D.E. Logan, Y.H. Szezech and M.A. Tusch: *Mott-Hubbard-Anderson models. In Metal-insulator transitions revisited (ed. P. P. Edwards and C. N. R. Rao).* page 343-394. London: Taylor and Francis (1995)
- [49] P. P. Edwards, R. L. Johnston, C.N.R. Rao, D. P. Tunstall and F. Hense: *The metal-insulator transition: a perspective.* Phil. Trans. R. Soc. Lond. A, 356, 5-22 (1998)
- [50] J.M. Ziman: *Models of Disorder.* Cambridge University Press, (1979)
- [51] H. Ibach and H. Lüth: *Festkrperphysik. Einfhruung in die Grundlagen.* Springer-Verlag Berlin Heidelberg, 3. Auflage (1990)
- [52] Sophocles J. Orfanidis: *Electromagnetic Waves and Antennas.* Piscataway (2013)
- [53] C. Cohen Tannoudji, B. Diu, F. Laloe: *Quantenmechanik.* Gruyter-Verlag, 2. Auflage (1999)
- [54] M. Störzer, P. Gross, C.M. Aegerter and G. Maret: *Observation of the Critical Regime Near Anderson Localization of Light.* Phys. Rev. Lett. 96, 063904 (2006)
- [55] M. Segev, Y. Silberberg and D.N. Christodoulides: *Anderson localization of light.* Nature Photonics 7, 197204 (2013)
- [56] R. Lenke and G. Maret: *Multiple Scattering of Light: Coherent Backscattering and Transmission.* Gordon and Breach, Amsterdam and Konstanzer Online-Publikations-System (KOPS) (2000)
- [57] M. Strötzer: *Anderson Localization of Light.* Dissertation Universitt Konstanz (2006)

- [58] D.S. Wiersma, M.P. van Albada and A. Lagendijk: *Coherent Backscattering of Light from Amplifying Random Media*. Phys. Rev. Lett. 75, 1739-1742 (1995).
- [59] D.J. Thouless: *Electrons in disordered systems and the theory of localization*. Phys. Rep., Vol. 13, Issue 93 (1974),
- [60] D.J. Thouless: *Maximum Metallic Resistance in Thin Wires* Phys. Rev. Lett. 82, 40144017, (1999)
- [61] F. Riboli, P. Barthelemy, S. Vignolini, F. Intonti, A. De Rossi, S. Combric, and D. S. Wiersma: *Anderson localization of near-visible light in two dimensions*. Optics Letters, Vol. 36, Issue 2, pp. 127-129 (2011)
- [62] J. Wang A.Z. Genack: *Transport through modes in random media*. Nature 471, 345-348 (2011).
- [63] Th.M.Nieuwenhuizen , M.C.W van Rossum: *Intensity Distributions of Waves Transmitted through a Multiple Scattering Medium*. Phys. Rev. Lett. Vol 74, 2674 (1989)
- [64] A. Chhabra, R. V. Jensen: *Direct Determination of the $f(\alpha)$ Singularity Spectrum*. Phys. Rev. Letters Vol 62, 1327 (1989)
- [65] L.J. Vasquez, A. Rodriguez, R.A. Rmer: *Multifraktal analysis of the metal-insulator transition in the three-dimensional Anderson model. Symmetry relation under typical averaging*. Phys. Rev. B Vol 78, 195106 (2008)
- [66] M. O. Scully and M. S. Zubairy: *Quantum Optics*. Cambridge University Press (2001)
- [67] M.J. Duer: *Introduction to Solid-State NMR Spectroscopy*. Blackwell Publishing (2004)
- [68] Yehuda B. Band: *Light and Matter: Electromagnetism, Optics, Spectroscopy and Lasers*. John Wiley and Sons, (2006)
- [69] G. Stibenz: *Neue Methoden der Charakterisierung und Kompression intensiver ultrakurzer optischer Impulse*. Dissertation, Humboldt-Universitt zu Berlin, Mathematisch-Naturwissenschaftliche Fakultt I (2008)
- [70] S. Schmidt, M. Mascheck, M. Silies, T. Yatsui, K. Kitamura, M. Ohtsu and C. Lienau: *Distinguishing between ultrafast optical harmonic generation and multi-photon-induced luminescence from ZnO thin films by frequency-resolved interferometric autocorrelation microscopy*. Opt. Express 18, 25016-25028, (2010)
- [71] K. Vanheusden, W. L. Warren, C. H. Seager, D. R. Tallant, J. A. Voigt, B. E Gnade: *Mechanisms behind green photoluminescence in ZnO phosphor powders*. Journal of Applied Physics, Vol 79 Issue 10, 7983 - 7990 (1996)

- [72] E. Abrahams, P.W. Anderson, D.C. Licciardello, T.V. Ramakrishnan: *Scaling Theory of Localisation: Absence of Quantum Diffusion in Two Dimensions*. Phys. Rev. Letters Vol 42, 673 (1979)
- [73] G. Stibenz, G. Steinmeyer: *Interferometric frequency-resolved optical gating*. Opt. Express 13, 2617 (2005)
- [74] Yun-Ju Lee *, D. S. Ruby , D. W. Peters , B. B. McKenzie and J. W. P. Hsu: *ZnO Nanostructures as Efficient Antireflection Layers in Solar Cells*. Nano Lett. 8 (5), pp 15011505, DOI: 10.1021/nl080659j (2008)
- [75] A. Dal Corso, M. Posternak, R. Resta and A. Baldereschi: *Ab initio study of piezoelectricity and spontaneous polarization in ZnO*. Phys. Rev. B 50 , 10715-10721 (1994).
- [76] C.F. Klingshirn, B.K. Meyer, A. Waag, A. Hoffmann and J. Geurts: *Zinc Oxide. From Fundamental Properties Towards Novel Applications*. Springer Heidelberg Dodrecht London New York, (2010)
- [77] A. Janotti and C.G Van de Walle: *Fundamentals of zinc oxide as a semiconductor*. Rep. Prog. Phys. 72 , 126501 (2009)
- [78] R.J.D. Tilley: *Understanding Solids: The Science of Materials*. John Wiley and Sons (2004)
- [79] A.B. DjurisiC and Y.H. Leung: *Optical properties of ZnO nanostructures.*, Small 2, 944961 (2006)
- [80] U. Özgür , Y.I. Alivov, C. Liu, A. Teke, M.A. Reshchikov, S. Dogan, V.Avrutin S.-J. Cho and H. Morkoc: *A comprehensive review of ZnO materials and devices*. Journal of Applied Physics 98, 041301 (2005).
- [81] J.P. Richters: *Optische Eigenschaften von ZnO-Nanodrühten: Einfluss von Oberflächenbehandlungen und hohen Anregungsdichten*. Dissertation , Bremen (2010).
- [82] Srikant and Clarke: *On the optical excitation of zinc oxide*. Journal of Applied Physics, Vol 83 Nr 10, (1998)
- [83] <http://refractiveindex.info/?group=CRYSTALS&material=ZnO>
- [84] U. Griebner, R.A. Kaindl, T. Elsaesser and W. Seeber: *Frequency doubling and autocorrelation studies of 20-fs pulses using polycrystalline zinc oxide thin films*. Applied Physics B, Volume 67, Issue 6, 757-760 (1998)
- [85] U. Neumann, R. Grunwald, U. Griebner, G. Steinmeyer: *Second harmonic efficiency of ZnO nanolayers*. Appl. Phys. Lett. 84, 170-172 (2004)
- [86] K. Kitamura et al: *Fabrication of vertically aligned ultrafine ZnO nanorods using metal-organic vapor phase epitaxy with a two-temperature growth method*. Nanotechnology 19, 175305 (2008)
- [87] B. Piglosiewicz, D. Sadiq, M. Mascheck, S. Schmidt, M. Silies, P. Vasa, and C. Lienau: *Ultra small bullets of light*. Optics Express, Vol. 19, Issue 15, pp. 14451-14463 (2011)

- [88] R. Trebino: *Frequency-Resolved Optical Gating: The Measurement of Ultrashort Laser Pulses*. Springer Netherlands (2009)
- [89] A.P. Mosk, A. Lagendijk, G. Lerosey and M. Fink: *Controlling waves in space and time for imaging and focusing in complex media*. Nature Photonics 6, 283292, (2012)
- [90] V. Emiliani, F. Intonti, M. Cazayous, D. S. Wiersma, M. Colocci, F. Aliev and A. Lagendijk: *Near-field short range correlation in optical waves transmitted through random media*. Phys. Rev. Lett. 90, 250801 (2003)
- [91] U. Neuberth, L. Walter, G. von Freymann, Th. Schimmel, M. Wegener, G. Khitrova and H. M. Gibbs: *Spatial autocorrelation analysis of nanophotoluminescence images of single GaAs quantum wells*. Appl. Phys. Lett. 81, 1881 (2002)
- [92] L. Novotny, R.X. Bian and X.S. Xie: *Theory of Nanometric Optical Tweezers*. Phys. Rev. Lett. 79, 645648 (1997)
- [93] E.J. Sanchez, L. Novotny and X.S. Xie: *Near-Field Fluorescence Microscopy Based on Two-Photon Excitation with Metal Tips*. Phys. Rev. Lett. 82, 40144017 (1999)
- [94] A. Hartschuh, N. Anderson, L. Novotny: *Near-field Raman spectroscopy using a sharp metal tip*. Journal of Microscopy, Vol. 210, Pt 3 June 2003, pp. 234240 (2002)
- [95] A. F. Oskooi, D. Roundy, M. Ibanescu, P. Bermel, J. D. Joannopoulos, and S. G. Johnson: *MEEP: A exible free-software package for electromagnetic simulations by the FDTD method*. Computer Physics Communications 181, 687702 (2010).
- [96] W. H. Press, S.A. Teukolsky, W.T. Vetterling and B.P. Flannery: *Numerical Recipes 3rd Edition: The Art of Scientific Computing*. Cambridge University Press, Auflage 3 (2007)
- [97] M. Mascheck, S. Schmidt, M. Silies, T. Yatsui, K. Kitamura, M. Ohtsu, D. Leipold, E. Runge, and C. Lienau: *Observing the localization of light in space and time by ultrafast second-harmonic microscopy*. Nature Photonics 6, 293-298 (2012)
- [98] A. Taflove and M. E. Brodwin: *Numerical solution of steady-state electromagnetic scattering problems using the time-dependent Maxwell's equations*. IEEE Transactions on Microwave Theory and Techniques 23 (8): 623630 (1975)
- [99] D.S. Katz, E.T Thiele and A. Taflove: *Validation and ectension to 3 dimensios of the Berenger PML Absorbing boundary-conditions for FDTD Meshes.*, IEEE Microwave and guided wave Letters ,Vol 4 Issue 8, 268-270 (1994)
- [100] O.L. Stroyuk, V.M. Dzhanan, V.V. Shvalagin and S.Ya Kuchmiy: *Size Dependent Optical Properties of Colloidal ZnO Nanoparticles Charged by Photoexcitation*. J.Phys. Chem. C , 114 pp. 220-225 (2010)

- [101] J. Sartor, F. Maier-Flaig, J. Conradt, J. Fallert, H. Kalt, D. Weissenberger, and D. Gerthsen: *Modifying growth conditions of ZnO nanorods for solar cell applications*. *physica status solidi (c)* 7, 1583-1585 (2010)
- [102] L. Novotny and B. Hecht: *Principles of Nano-Optics*. Cambridge University Press, Auflage 2 (2012)
- [103] C. Hettich, C. Schmitt, J. Zitzmann, S. Khn, I. Gerhardt, V. Sandoghdar: *Nanometer resolution and coherent optical dipole coupling of two individual molecules*. *Science* 298, 385 (2002)
- [104] B.T. Draine and P.J. Flatau: *Discrete-dipole approximation for scattering calculations*. *JOSA A*, Vol. 11, Issue 4, pp. 1491-1499 (1994)
- [105] Dermtröder: *Experimentalphysik2 - Elektrizität und Optik*. Springer, 4.Auflage (2006)
- [106] Jackson: *Klassische Elektrodynamik*. Walter de Gruyter, 4. Auflage (2006)
- [107] H.C. van de Hulst: *Light Scattering by Small Particles*. page 316-317, Dover Publications, Inc. New York (1981)
- [108] C.F. Bohren and D.R. Huffman: *Absorption and scattering of light by small particles*. Wiley Science Paperback Series, New York (1998)
- [109] C. Ropers, D. R. Solli, C. P. Schulz, C. Lienau, and T. Elsaesser: *Localized multiphoton emission of femtosecond electron pulses from metal nanotips*. *Phys. Rev. Lett.* 98, 043907 (2007)
- [110] D.J. Park, B. Piglosiewicz, S. Schmidt, H. Kollmann, M. Mascheck and C. Lienau: *Strong Field Acceleration and Steering of Ultrafast Electron Pulses from a Sharp Metallic Nanotip*. *Phys. Rev. Letters* 109, 244803 (2012)
- [111] P. Hommelhoff, Y. Sortais, A. Aghajani-Talesh and M. A. Kasevich: *Field Emission Tip as a Nanometer Source of Free Electron Femtosecond Pulses*. *Phys. Rev. Lett.* 96, 077401 (2006)
- [112] P. Hommelhoff, C. Kealhofer, and M. A. Kasevich: *Ultrafast Electron Pulses from a Tungsten Tip Triggered by Low-Power Femtosecond Laser Pulses*. *Phys. Rev. Lett.* 97, 247402 (2006)
- [113] O. Schmidt, M. Bauer, C. Wiemann, R. Porath, M. Scharte, O. Andreyev, G. Schonhense and M. Aeschlimann: *Time-resolved two photon photoemission electron microscopy*. *Appl. Phys. B* 74, 223227 (2002)
- [114] L. Douillard, F. Charra, C. Fiorini, P.M. Adam, R. Bachelot, S. Kostchev, G. Lerondel, M.L. de la Chapelle and P. Royer: *Optical properties of metal nanoparticles as probed by photoemission electron microscopy*. *JOURNAL OF APPLIED PHYSICS* 101, 8 083518 (2007)

- [115] D. Bayer, C. Wiemann, O. Gaier, M. Bauer and M. Aeschlimann: *Time-Resolved 2PPE and Time-Resolved PEEM as a Probe of LSP's in Silver Nanoparticles*. Journal of Nanomaterials, Vol 2008 , 249514, (2008)
- [116] E. Bauer: *The resolution of the low energy electron reflection microscope*. Ultramicroscopy Volume 17, Issue 1, p51-56 (1985)
- [117] W. Telieps, E. Bauer: *An analytical reflection and emission UHV surface electron microscope*. Ultramicroscopy Volume 17, Issue 1, p5765, (1985)
- [118] M. U. Wehner, M. H. Ulm, and M. Wegener: *Scanning interferometer stabilized by use of Pancharatnam's phase*. Optics Letters Voll. 22, No 19, (1997)
- [119] C. Hrelescu, T.K. Sau, A.L. Rogach, F. Jackel, G. Laurent, L. Douillard and F. Charra: *Selective Excitation of Individual Plasmonic Hotspots at the Tips of Single Gold Nanostars*. Nano Lett. 11 (2), pp 402407 (2011)
- [120] S.W. Chan, R. Barille, J.M. Nunzi, K.H. Tam, Y.H. Leung, W.K. Chan and C. Djurisi: *Second harmonic generation in zinc oxide nanorods*. Applied Physics B 84, 351355 (2006)
- [121] J. Sator: *Random Lasing in nanokristallinen ZnO-Pulvern*. Dissertation KIT-Bibliothek (2012)
- [122] D. S. Wiersma, A. Lagendijk: *Light diffusion with gain and random lasers*. Phys. Rev. E 54, 42564265 (1996)
- [123] D. S. Wiersma: *The physics and applications of random lasers*. Nature Physics 4, 359-367 (2008)
- [124] V. M. Markushev, V. F. Zolin and Ch. M. Briskina: *Luminescence and stimulated emission of neodymium in sodium lanthanum molybdate powders*. Sov. J. Quantum Electron. 16 , 281 (1986)
- [125] N. . Ter-Gabrilyan, V. M. Markushev, V. R. Belan, Ch. M. Briskina and V. F. Zolin: *Stimulated emission spectra of powders of double sodium and lanthanum tetramolybdate*. Sov. J. Quantum Electron. 21 , 32 (1991)
- [126] H. Cao, J.Y. Xu, S.-H. Chang and S. T. Ho: *Transition from amplified spontaneous emission to laser action in strongly scattering media*. Phys. Rev. E 61, 19851989 (2000)
- [127] D. S. Wiersma: *Disordered photonics.*, Nature Photonics 7, 188196 (2013)

Appendix A

Scattering cross section

The calculation of the scattering cross section C_s of a single nano-object is following the approach of van de Hulst [107] and of Bohren [108]. In general, it is based on solving the wave equation for the electric field \vec{E} and the magnetic field \vec{H} .

$$\nabla^2 \vec{E} + k^2 \vec{E} = 0 \quad \nabla^2 \vec{H} + k^2 \vec{H} = 0 \quad (\text{A.1})$$

with $k^2 = \omega^2 \cdot \varepsilon(\vec{r})\mu(\vec{r})$ and ω the angular frequency of the field. The scattering object is described by a spatial dependent permittivity $\varepsilon(\vec{r}) = \varepsilon_0 \varepsilon_r(\vec{r})$ and permeability $\mu(\vec{r}) = \mu_0 \mu_r(\vec{r})$. In the absence of free charges, i.e. $\rho = 0$ and $\vec{j} = 0$, the electric field as well as the magnetic field

$$\nabla \cdot \vec{E} = 0 \quad \nabla \cdot \vec{H} = 0 \quad (\text{A.2})$$

are divergence free. The wave vector function $\vec{\Psi}$ is assumed to solve the equations in A.1. In order to simplify this calculation, a solution based on a scalar wave function ψ is desired. Therefore the vector functions \vec{M} and \vec{N} are constructed by

$$\vec{M} = \nabla \times \vec{c}\psi \quad \nabla \times \vec{N} = k\vec{M} \quad (\text{A.3})$$

to solve the vector wave equation A.1. This criterion is fulfilled, if the scalar generating function ψ together with the guiding vector \vec{c} is a solution of the scalar wave equation

$$\nabla^2 \psi + k^2 \psi = 0 \quad . \quad (\text{A.4})$$

We concentrate on the electric field which can than be expressed in terms of

$$\vec{E} = E_0 \sum_{i=1}^{\infty} i^n \frac{2n+1}{n(n+1)} (\vec{M}_{o,n} - \vec{N}_{e,n}) \quad (\text{A.5})$$

with indices e and o describing even and odd solutions.

For a spherical scattering object, it makes sense to formulate the wave equation A.4 in spherical coordinates.

$$\frac{1}{r^2} \frac{\partial}{\partial r} \left(r^2 \frac{\partial \psi}{\partial r} \right) + \frac{1}{r^2 \sin \theta} \frac{\partial}{\partial \theta} \left(\sin \theta \frac{\partial \psi}{\partial \theta} \right) + \frac{1}{r^2 \sin \theta} \frac{\partial^2 \psi}{\partial \phi^2} + k^2 \psi = 0 \quad (\text{A.6})$$

For a spherical object, the guiding vector is described by $\vec{c} = \vec{r}$. In order to solve equation A.6, a separation ansatz is used.

$$\psi(r, \theta, \phi) = R(r) \cdot \Theta(\theta) \cdot \Phi(\phi) \quad (\text{A.7})$$

This results in three independent equations for Φ , Θ and R .

$$\frac{\partial^2 \Phi}{\partial \phi^2} + m^2 \Phi = 0 \quad (\text{A.8})$$

$$\frac{1}{\sin \theta} \frac{\partial}{\partial \theta} \sin \theta \frac{\partial \Theta}{\partial \theta} + \left(n(n+1) - \frac{m^2}{\sin^2 \theta} \right) \Theta = 0 \quad (\text{A.9})$$

$$\frac{\partial}{\partial r} \left(r^2 \frac{\partial R}{\partial r} \right) + (k^2 r^2 - n(n+1)) R = 0 \quad (\text{A.10})$$

Solutions of equation A.8 are given by $\Phi_e = \cos(m\phi)$ for the even and $\Phi_e = \sin(m\phi)$ for the odd solutions. Equation A.9 is solved by the Legendre functions $P_{m_d}^n(\cos \theta)$ of degree m_d and order n . The use of a dimensionless size parameter $x = kr$ changes equation A.10 to

$$x \frac{\partial}{\partial x} \left(x \frac{\partial Z}{\partial x} \right) + (x^2 - n(n+1)^2) Z = 0 \quad (\text{A.11})$$

with Z describing the Bessel function. Different kinds of Bessel functions fulfil equation A.11. First kind of Bessel function J and the second kind Y (also called Neumann function and sometimes named by N) can be used. For spherical scattering objects, it is meaningful to use the spherical Bessel functions which are described by

$$j_n(x) = \sqrt{\frac{\pi}{2x}} J_{n+\frac{1}{2}}(x) \quad y_n(x) = \sqrt{\frac{\pi}{2x}} Y_{n+\frac{1}{2}}(x) \quad . \quad (\text{A.12})$$

Different orders n of the Bessel functions can be obtained by using the recurrence relations

$$Z_{n-1}(x) + Z_{n+1}(x) = \frac{2n+1}{x} Z_n(x) \quad (\text{A.13})$$

$$\frac{\partial}{\partial p} Z_n(x) = \frac{n}{2n+1} Z_{n-1}(x) - \frac{n+1}{2n+1} Z_{n+1}(x) \quad . \quad (\text{A.14})$$

Also every linear combination of $j_n(x)$ and $y_n(x)$ solves equation A.10. These combinations are called spherical Hankel functions $h_n^{(1)}$ and $h_n^{(2)}$.

$$h_n^{(1)} = j_n(x) + iy_n(x) \quad h_n^{(2)} = j_n(x) - iy_n(x) \quad (\text{A.15})$$

By using the first two orders

$$j_0(x) = \frac{\sin x}{x} \quad y_0(x) = -\frac{\cos x}{x} \quad (\text{A.16})$$

$$j_1(x) = \frac{\sin x}{x^2} - \frac{\cos x}{x} \quad y_1(x) = -\frac{\cos x}{x^2} - \frac{\sin x}{x} \quad (\text{A.17})$$

any other order of the spherical Bessel functions can be calculated using the recurrence relation A.14.

With this knowledge, the generating function ψ that satisfies the scalar wave equation can be written down to

$$\psi_{e,m,n}(x, \theta, \phi) = \cos(m\phi) \cdot P_m^n(\cos \theta) \cdot Z_n(x) \quad (\text{A.18})$$

for the even and

$$\psi_{e,m,n}(x, \theta, \phi) = \sin(m\phi) \cdot P_m^n(\cos \theta) \cdot Z_n(x) \quad (\text{A.19})$$

for the odd solutions of the wave function.

The scattering of an electromagnetic wave at a sphere can fully be characterized by an incident wave, a scattered wave and the wave inside the sphere. The incident plane wave can be written in terms of a linear combination of spherical waves with the scalar generating function

$$u_1 = e^{i\omega t} \cos(\phi) \sum_{n=1}^{\infty} (-i)^n \frac{2n+1}{n(n+1)} \cdot P_1^n(\cos \theta) \cdot j_n(x) \quad (\text{A.20})$$

$$v_1 = e^{i\omega t} \sin(\phi) \sum_{n=1}^{\infty} (-i)^n \frac{2n+1}{n(n+1)} \cdot P_1^n(\cos \theta) \cdot j_n(x) \quad (\text{A.21})$$

The wave scattered at the spherical particle is described by:

$$u_2 = e^{i\omega t} \cos(\phi) \sum_{n=1}^{\infty} (-i)^n (-a_n) \frac{2n+1}{n(n+1)} \cdot P_1^n(\cos \theta) \cdot h_n^{(2)}(x) \quad (\text{A.22})$$

$$v_2 = e^{i\omega t} \sin(\phi) \sum_{n=1}^{\infty} (-i)^n (-b_n) \frac{2n+1}{n(n+1)} \cdot P_1^n(\cos \theta) \cdot h_n^{(2)}(x) \quad (\text{A.23})$$

The wave inside of the scattering object is described by

$$u_3 = e^{i\omega t} \cos(\phi) \sum_{n=1}^{\infty} (-i)^n (c_n) \frac{2n+1}{n(n+1)} \cdot P_1^n(\cos \theta) \cdot j_n(y) \quad (\text{A.24})$$

$$v_3 = e^{i\omega t} \sin(\phi) \sum_{n=1}^{\infty} (-i)^n (d_n) \frac{2n+1}{n(n+1)} \cdot P_1^n(\cos \theta) \cdot j_n(y) \quad (\text{A.25})$$

with $y = kmr$ and m the complex refractive index.

By using the continuity condition at the interface of the object for the wave function and its first derivative, the scattering coefficients a_n and b_n can be determined. For a spherical scattering object they are given by

$$a_n = \frac{\psi'_n(y)\psi_n(x) - m\psi_n(y)\psi'_n(x)}{\psi'_n(y)\xi_n(x) - m\psi_n(y)\xi'_n(x)} \quad (\text{A.26})$$

$$b_n = \frac{m\psi'_n(y)\psi_n(x) - \psi_n(y)\psi'_n(x)}{m\psi'_n(y)\xi_n(x) - \psi_n(y)\xi'_n(x)} \quad (\text{A.27})$$

substituting $\psi_n(x) = x \cdot j_n(x) = \sqrt{\frac{\pi x}{2}} J_{n+1/2}(x)$ and $\xi_n(x) = x \cdot h_n^{(2)}(x) = \sqrt{\frac{\pi x}{2}} h_{n+1/2}^{(2)}(x)$. This allows to calculate the generating function ψ and hence by using equation A.3 also the local electric and magnetic field.

The scattering efficiency factor Q_{sca} can be determined by

$$Q_{sca} = \frac{2}{x^2} \sum_{n=1}^{\infty} (2n+1) \left(|a_n|^2 + |b_n|^2 \right) \quad (\text{A.28})$$

The scattering cross section C_{sca} is defined by

$$C_{sca} = Q_{sca} \cdot G \quad (\text{A.29})$$

with the geometrical cross section G . For a sphere, the geometrical cross section is given by $G_{sp} = \pi a^2$ with a the radius. More details and the calculated scattering cross section can be found in [108].

Cylinders: In order to calculate the scattering cross section of a cylinder, the derivation changes slightly¹. In this case, the scattering coefficients are described by

$$a_n = \frac{\left(\frac{D_n(mx)}{m} + \frac{n}{x}\right) J_n(x) - J_{n-1}(x)}{\left(\frac{D_n(mx)}{m} + \frac{n}{x}\right) H_n^{(1)}(x) - H_{n-1}^{(1)}(x)} \quad (\text{A.30})$$

and

$$b_n = \frac{(D_n(mx)m + \frac{n}{x}) J_n(x) - J_{n-1}(x)}{(D_n(mx)m + \frac{n}{x}) H_n^{(1)}(x) - H_{n-1}^{(1)}(x)} \quad (\text{A.31})$$

The logarithmic derivative and the recurrence relation

$$D_n(mx) = \frac{J'_n(mx)}{J_n(mx)} \quad J'_n(mx) = J_{n-1}(mx) - \frac{n}{mx} J_n(mx) \quad (\text{A.32})$$

allows to deduce any order for all kinds of Bessel and Hankel functions and to calculate the wave function ψ and the resulting electric and magnetic fields.

In the case of the cylinder geometry, the guiding vector is expressed as $\vec{c} = \vec{e}_z$ if the cylinder-axis is aligned along the z-direction. The expression of the efficiency factor Q for the scattering and extinction changes in the case of an incident electric field with a wave vector perpendicular to the cylinder and a polarization along the cylinder axis \parallel . It is given as

$$Q_{sca} \parallel = \frac{2}{x} \left[|b_0|^2 + 2 \sum_{n=1}^{\infty} (|a_n|^2 + |b_n|^2) \right] \quad (\text{A.33})$$

$$Q_{ext} \parallel = \frac{2}{x} \Re \left[b_0^2 + 2 \sum_{n=1}^{\infty} b_n \right] \quad (\text{A.34})$$

and for a polarization perpendicular \perp to the cylinder axis by

$$Q_{sca} \perp = \frac{2}{x} \left[|a_0|^2 + 2 \sum_{n=1}^{\infty} (|a_n|^2 + |b_n|^2) \right] \quad (\text{A.35})$$

$$Q_{ext} \perp = \frac{2}{x} \Re \left[a_0^2 + 2 \sum_{n=1}^{\infty} a_n \right] \quad (\text{A.36})$$

The scattering cross section C_{sca} is determined by equation A.29 with the geometrical cross section $G_{cyl} = d \cdot l$. Here, d is the diameter and l is the length of the cylinder. The resulting scattering cross sections are shown for the two different polarizations of the incident electric field in figure A.1. Unfortunately,

¹The details are described in [108] *Potpourri of particles*

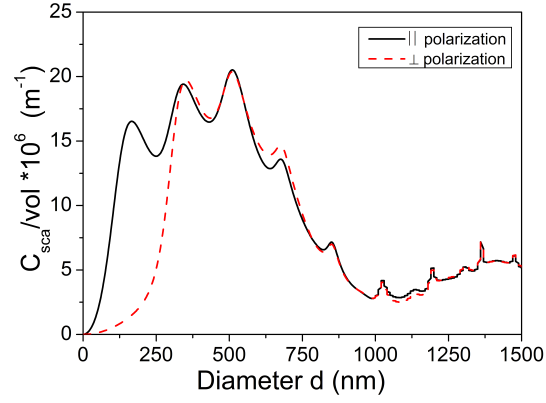


Figure A.1: Calculated scattering cross section normalized to the volume of a cylinder of unit length with the refractive index $m = 1.95 + i0.0043$. The polarization of the scattered incident wave ($\lambda = 870 \text{ nm}$) is assumed to be perpendicular (\perp) or along the cylinder axis (\parallel).

the asymptotic behaviour of the scattering cross section

$$\frac{C_{sca}}{vol} \sim \frac{4}{\pi \frac{d}{2}} \quad (\text{A.37})$$

described by Bohren delivers a discrepancy by a factor of two. Nevertheless, the shape of C_{sca} is in good agreement with the literature.

Publications and Conference contributions

Publications

- D. J. Park, B. Piglosiewicz, S. Schmidt, H. Kollmann, M. Mascheck, P. Gross and C. Lienau
Characterizing the optical near-field in the vicinity of a sharp metallic nanoprobe by angle-resolved electron kinetic energy spectroscopy.
Ann. Phys. 525 (1-2) 135-142 (2013)
- D. Leipold, M. Silies, M. Mascheck, C. Lienau, E. Runge
Ultrafast dynamics of localized light modes.
Ann. Phys. 525 (1-2) 199-204 (2013)
- D. J. Park, B. Piglosiewicz, S. Schmidt, H. Kollmann, M. Mascheck and C. Lienau
Strong field acceleration and steering of ultrafast electron pulses from a sharp metallic nanotip.
PRL 109, 244803 (2012)
- M. Mascheck, S. Schmidt, M. Silies, D. Leipold, E. Runge, T. Yatsui, K. Kitamura, M. Ohtsu, and C. Lienau
Observing the localization of light in space and time by ultrafast second harmonic microscopy.
Nature Photonics 6, 293-298 (2012)
- B. Piglosiewicz, D. Sadiq, M. Mascheck, S. Schmidt, M. Silies, P. Vasa, and C. Lienau
Ultrasmall bullets of light - Focusing few-cycle light to the diffraction limit.
Opt. Express 19, 14451-14463 (2011)
- S. Schmidt, M. Mascheck, M. Silies, T. Yatsui, K. Kitamura, M. Ohtsu, and C. Lienau
Distinguishing between ultrafast harmonic generation and multi-photon-induced luminescence from ZnO thin films by frequency-resolved interferometric autocorrelation microscopy.
Opt. Express 18, 25016 (2010)

Conference contributions

- M. Mascheck, S. Schmidt, M. Silies, D. Leipold, E. Runge, T. Yatsui, K. Kitamura, M. Ohtsu, and C. Lienau
Observing the localization of light in space and time by ultrafast second-harmonic microscopy.
Near Field Optics, San Sebastian, Spain (2012)
- M. Mascheck, S. Schmidt, M. Silies, D. Leipold, E. Runge, T. Yatsui, K. Kitamura, M. Ohtsu, and C. Lienau
Trapping light in random ZnO nanorod arrays - Localization of light in space and time.
Deutsch Physikalische Gesellschaft, Spring-Meeting, Berlin , Germany (2012)
- M. Mascheck, S. Schmidt, M. Silies, D. Leipold, E. Runge, T. Yatsui, K. Kitamura, M. Ohtsu, and C. Lienau
Weak localization of light in ZnO nanorods in space and time.
JST/DFG German-Japanese Nano-Optics, Kyoto, Japan (2011)
- M. Mascheck, S. Schmidt, M. Silies, D. Leipold, E. Runge, T. Yatsui, K. Kitamura, M. Ohtsu, and C. Lienau
Weak localization of light in ZnO nanorods in space and time.
Deutsch Physikalische Gesellschaft, Spring-Meeting, Dresden , Germany (2011)
- M. Mascheck, S. Schmidt, M. Silies, D. Leipold, E. Runge, T. Yatsui, K. Kitamura, M. Ohtsu, and C. Lienau
Localizing light in random zinc oxide nanoneedle arrays.
ECONOS Bremen (2010)
- M. Mascheck, S. Schmidt, M. Silies, D. Leipold, E. Runge, T. Yatsui, K. Kitamura, M. Ohtsu, and C. Lienau
Ultrahigh temporal and spatial resolution imaging of second harmonic fields in random zinc oxide nanostructure arrays.
Deutsch Physikalische Gesellschaft, Spring-Meeting, Regensburg , Germany (2010)
- M. Mascheck and C. Lienau
Progress in tip-enhanced electron microscopy.
JST/DFG German-Japanese Nano-Optics, Delmenhorst, Germany (2008)

Curriculum vitae

Manfred Mascheck

- Allgemeines
 - Geboren am: 12.06.1983
 - Geburtsort: Fritzlar
 - Familienstand: Ledig
 - Nationalität: Deutsch
- Schule
 - 1989 - 1993 Grundschule Bad Zwesten, Germany
 - 1993 - 2002 Christliches Jugenddorf Gymnasium Oberurff, Germany
- Studium
 - 2002 - 2009 Physikstudium an der Carl von Ossietzky Universität Oldenburg, Germany
 - 2009 - 2013 Promotion an der Carl von Ossietzky Universität Oldenburg, Germany

Danksagung

Als Erstes geht mein Dank an Prof. Dr. Christoph Lienau für die sehr engagierte Betreuung meiner gesamten Forschungstätigkeiten in der Arbeitsgruppe UNO. Vielen Dank für die vielen interessanten Diskussionen, die stetige Hilfsbereitschaft und für den ein oder anderen Schubser in die richtige Richtung. Auch für die Möglichkeit an interessanten und aktuellen Forschungsthemen zu arbeiten, die auch international auf Interesse stießen und mir Vorträge in Kyoto und San Sebastian ermöglichten, möchte ich mich herzlich bei Prof. Lienau bedanken.

Prof. Dr. Erich Runge danke ich für die Bereitschaft das Zweitgutachten zu übernehmen. Vielen Dank auch für die ein oder andere Diskussion im Rahmen der Zusammenarbeit unserer Publikationen.

Diesbezüglich gilt mein Dank auch David Leipold für die vielen FDTD Berechnungen und auch für seine Geduld, wenn wir das Simulationsgebiet immer wieder änderten.

Des Weiteren gilt mein Dank Prof. Dr. Martin Aeschlimann und Pascal Melchior für die Unterstützung bei den hochauflösenden PEEM Lokalisierungsmessungen.

Ohne den tollen Rückhalt in der Arbeitsgruppe UNO wäre mir die Arbeit sicherlich viel schwerer gefallen. Vielen Dank für die viele Unterstützung und Motivation. Danke!!! Insbesondere möchte ich mich bei Slawa, Martin, Heiko und Björn für die viele Hilfe bedanken. Des Weiteren gilt mein Dank Effe, Robert, Martin, Simon, Ralf, Petra, Wei, DJ, Raimond und natürlich auch Margret die mich vielfach unterstützt haben.

Vielen Dank auch an die Physikerrunde Malte, Reef, Anne und Dani. Mein besondere Dank geht dabei an Johanna. Für die immer wieder nötige Motivation danke ich Stephan, Juliane, Roland, Harald und Familie Martin die mich über Jahre hinweg uneingeschränkt unterstützt haben. Des Weiteren Lisa und Alena, die mich immer wieder angetrieben haben. Dank auch an an Katrin und Esther für die Unterstützung.

Mein herzlichster Dank gilt meine Eltern, Lena und Jan. Ohne euch alle wäre dies alles nicht möglich gewesen.....Danke!

Formale Erklärung

Hiermit versichere ich, dass ich diese Arbeit selbständig verfasst und keine anderen als die angegebenen Quellen und Hilfsmittel benutzt habe. Außerdem versichere ich, dass ich die allgemeinen Prinzipien wissenschaftlicher Arbeit und Veröffentlichung, wie sie in den Leitlinien guter wissenschaftlicher Praxis der Carl von Ossietzky Universität Oldenburg festgelegt sind, befolgt habe.

Manfred Mascheck